PORE NETWORK MODELLING OF WETTABILITY EFFECTS ON WATERFLOOD OIL RECOVERY FROM AGBADA SANDSTONE FORMATION IN THE NIGER DELTA, NIGERIA

Onuoha Fidelis Wopara

A thesis Submitted to the School of Chemical and Metallurgical Engineering, Faculty of Engineering and the Built Environment, University of the Witwatersrand, Johannesburg, in fulfillment of the requirements for the degree of Doctor of Philosophy

Johannesburg, 2016

DECLARATION

I declare that this thesis is my own unaided work. It is being submitted for the degree of Doctor of Philosophy to the University of the Witwatersrand, Johannesburg. It has not been submitted before for any degree or examination to any other University.

_____

Onuoha Fidelis Wopara

31st day of May, 2016

Abstract

Wettability of a porous reservoir rock is an important factor that affects oil recovery during waterflooding. It is recognized as being important for multiphase properties. Understanding the variation of these properties in the field, due to wettability trends and different pore structures, is very critical for designing efficient and reliable processes and projects for enhanced hydrocarbon recovery. After primary drainage the reservoir wettability changes: if it was oil-wet initially, it gradually changes to water-wet during waterflooding. This change in reservoir wettability towards water-wet will reduce the residual oil saturation and improve the oil displacement efficiency. However, knowledge of the constitutive relationship between the pore scale descriptors of transport in the porous system is required to adequately describe wettability trend and its impact on oil recovery, particularly during waterflooding. In this work, the petrophysical properties that define fluid flow in the Agbada, Nigeria sandstone reservoir were determined using conventional experimental and x-ray CT scanning methods. Experimentally measured average porosity is 0.28, average permeability is 1699 mD, while the initial and irreducible water saturation is 0.22. Permeability in the *x*, *y* and *z* directions, ranging from 50 to 200 mD, were calculated from the pore network extracted from the Agbada sandstone rock. Results obtained from the Amott-Harvey wettability measurement method indicate that the reservoir is strongly water-wet, with Amott-Harvey index of about 0.9. The cross-over between the water and oil relative permeabilities occurred at saturations of the samples above 0.5, giving an indication of strong water-wetness. The work summarizes the mechanism of wettability alteration and characterizes the performance of the reservoir during waterflooding from injecting water, and relates the residual oil saturation, relative permeability and volumes of water injected to

wettability and its effects on oil recovery. Waterflood oil recovery is computed using the Buckley-Leverett method based on the reservoir rock and fluid properties. Computed waterflood oil recovery using this method was about 60% of the oil initially in place. Plots of spontaneous imbibition rate show that the injection rate for optimal oil recovery is 40 bbls of injected water per day. At this rate, both the mobility and shock front mobility ratios are less than 1, leading to a stable flood front and absence of viscous fingering. Waterflooding is by far the most widely applied method of improved oil recovery over the years with good results in conventional and unconventional (tight oil) reservoirs It is relatively simple and cost effective: abundance and availability of water. Waterflood oil recovery factor is affected by internal and external factors. The placement of the injection and production wells, for example, impacts on the effectiveness of the waterflooding process. I considered the placement of the wells in a five-spot pattern as elements of an unbounded double periodic array of wells and assumed the reservoir to be homogeneous, infinite and isotropic, with constant porosity and permeability. Both fluids are treated as having slight but constant compressibility and their flow governed by Darcy's law. The average pressure in the reservoir satisfies quasi-static flow or diffusion equation. I then assumed piston-like displacement of oil by injected water that takes account of viscosity diffence between both fluids and proposed a model based on the theory of elliptic functions, in particular Weierstrass p-functions functions. Oil-water contact movement, dimensionless time for water breakthrough at the production well, areal sweep and average reservoir pressures were modeled. The model was tested using Wolfram Mathematica 10 software and the results are promising. The thesis has therefore established that the Agbada sandstone reservoir is strongly water-wet and that waterflooding is a viable option for enhanced oil recovery from the reservoir.

Dedication

This PhD research work is dedicated to:

- God Almighty for His ever abundant mercies, goodness, blessings and strength.
- My family for unflinching support, encouragement and love.
- Everyone who finds this work useful.

Acknowledgments

This work has been carried out as a Doctor of Philosophy (PhD) thesis at the School of Chemical and Metallurgical Engineering, Faculty of Engineering and the Built Environment, University of the Witwatersrand, Johannesburg, South Africa, in the period of 2013 to 2015. My supervisor has been Professor Sunny Iyuke, Head of School of Chemical and Metallurgical Engineering, University of the Witwatersrand, Johannesburg.

I am very grateful to all my advisors who have guided me through this work. I think I have been very lucky having three excellent advisors who were always ready to help and inspire me. From my point of view the supervisors have complemented each other. I thank Professor Sunny Iyuke for his constant support, guidance, patience and encouragement during this work. Without his assistance, the work would never have been done. In particular, I am impressed with his ability to understand the different physical processes underlying multiphase flow in porous media. My sincere thanks go to Professors Boniface Obah and Essio Oboho for their inspiration and assistance on the improvements to the quality of this thesis.

I thank Professor Martin J Blunt of the Earth Sciences and Petroleum Engineering Department and Head of the Pore Scale Modeling Consortium, Imperial College, London, who not minding the distance between us in terms of physical contact, patiently explained to me through numerous electronic mails, the underlying principles of pore-scale modeling and fluid flow in porous media. I show utmost appreciation to the micro-CT system Laboratory of Imperial College London, and in particularly to Dr. Hu Dong who assisted in the scanning of the Agbada rock

samples. I also express gratitude to Mr. Reuben Dinuya and the LSS laboratory in Port Harcourt, Nigeria, for allowing me use of their core analysis laboratory for the experiments

I want to thank all the people at the School of Chemical and Metallurgical Engineering, University of the Witwatersrand, Johannesburg, South Africa, and my colleagues and students at the Petroleum Engineering Department of Rivers State University of Science & Technology, Port Harcourt, for the professional atmosphere accorded me during the duration of this work.

Finally, to my wife and children, I say thank you for your unconditional love and immense support! God keep you all for me!

Johannesburg, May, 2016

Onuoha Fidelis Wopara

Declaration.....ii

Abstract……..……..……...iii

Dedication……..……..……...v

Acknowledgement……..……..……..……..……..vi

Table of Contents……...…viii

List of Figures…….…….…….....……..…..….xiv

List of Tables……..…..…..……..…..……..……xvii

1: Introduction…… ……..……1

1.2 Aims and Objectives……..……..9

1.3 List of Publications…….……...11

2: Literature Review.....12

2.1 Introduction to Network Models 12

2.2 Description of the Pore Space……14

2.3 Multiphase Drainage……..22

2.3.1 Two-phase Drainage……...…..22

2.3.2 Three-phase Network Models……..……24

2.4 Fluid Transport Properties.....33

2.4.1 Interfacial Tension and Wettability.....34

2.4.2 Contact Angle Measurement……...……..36

2.4.3 Fluid Saturation…….38

2.4.4 Capillary Pressure 40

2.4.5 Drainage and Imbibition.....42

2.4.6 Fluid Displacement Energy…….……..44

2.4.7 Permeability 45

2.4.8 Relative Permeability……....45

2.4.9 Determination of Porosity and Permeability using x-ray CT……...46

2.4.10 Lattice-Boltzmann Method (LBM)…….48

2.5 Pore Networks, Geometry and Wetting Films……..….50

2.5.1 Pore Network Shapes.....50

2.5.2 Wetting Films.....52

2.6 The Effects of Wettability on Oil Recovery.....54

2.6.1 Interacting Parameters.....54

2.6.2 Wettability Concepts.....55

2.6.3 Reservoir Wettability and Oil Recovery Efficiency.....57

2.6.4 Wetting Alteration in Cores……...58

2.6.5 Pore Level Studies of Wettability Effects on Oil Recovery……..…59

2.6.6 Wettability and Oil Recovery by Gas Injection…….71

2.6.7 Phase Trapping……...73

2.7 Determination of Reservoir Wettability……..73

2.7.1 Contact Angle Method……..…….74

2.7.2 Amott Method…….……...75

2.7.3 Wettability Indices…….……76

2.8 Changes in Wettability…….……...78

2.9 Pore Network Simulation of Waterflooding……...……...…80

2.9.1 Reservoir Simulation…….80

2.9.2 Discretization Methods……..82

2.9.2.1 Finite Difference Method……..82

2.9.2.2 The Finite Volume Method……..83

2.9.3 Elliptic Functions……..84

2.9.3.1 Weierstrass Elliptic Functions……...…85

3: Materials and Experimental Methods……89

3.1 Introduction to Sampling Location……89

3.1.1 Geological Setting and Hydrocarbon Generation…….89

3.1.2 Lithostratigraphy……..91

3.1.3 Properties of Oil and Gas in the Niger Delta…….....93

3.2 Materials……....94

3.2.1 Core Samples……94

3.2.2 Preparation of Core Samples……....94

3.2.2.1 Cutting and Trimming…….…..94

3.2.2.2 Acetate Peel to Remove Rock Flour…….…95

3.2.2.3 Core Cleaning and Saturation…….……..96

3.3 Porosity Measurement……..…97

3.3.1 Dry Weight and Bulk Volume Measurement……...98

3.3.2 Helium Porosimeter……..99

3.4 Permeability Measurement……..100

3.5 Wettability Measurement…….…103

3.5.1 Experimental Procedures and Apparatus……103

3.5.1.1 Amott-Harvey Method……103

3.6 Coreflooding Experiment……..…105

3.7 Determination of Porosity and Permeability using x-ray Computed Tomography…….108

3.7.1 Basic Setup…….110

3.7.2 X-ray Attenuation……...……111

3.7.3 X-ray Sources……..…112

3.7.4 3-D Reconstruction……..…113

3.7.5 Spatial Resolution……...114

3.8 Sample Preparation……..114

3.9 Experimental Procedure……..…115

3.9.1 Image Acquisition……..116

3.9.1.1 Sample Positioning……..……..……...…116

3.9.1.2 Sensor Calibration……...…117

3.9.1.3 Operational Parameters……..117

3.9.1.4 Reconstruction……....117

3.10 Post Processing……..118

3.10.1 Median Filter……...…118

3.10.2 Image Segmentation……...…118

3.11 Network Extraction……120

3.12 Porosity Calculation……...121

3.13 Permeability Estimation – lattice Boltzmann…...…….122

3.14 Measurement of Saturation and Capillary Pressure ……..…….124

3.15 Buckley-Leverret Computation of Waterflood Oil Recovery……...125

3.15.1. Immiscible Displacement of Oil by Water……125

3.16 Simulation of Waterflooding in Agbada Sandstone Reservoir…….……127

3.16.1 Weierstrass Elliptic Functions……...…..128

3.16.2 Mathematical Model…….....128

3.16.3 Boundary Conditions……..…..131

3.16.4 Piston-Like Displacement……..……...135

3.17 Numerical Solution…….…...143

3.17.1 The Well Model……143

3.17.2 Data Input…….……144

3.17.3 Streamline Path 146

3.17.4 Tracing Streamlines 147

3.18 Time Stepping and Simulation Scheme 148

4: Results and Analysis……....150

4.1 Mineralogy, Porosity and Permeability……...……...….150

4.1.1 Representative Core Samples 152

4.2 Calculation of Porosity and Absolute Permeability from X-ray CT……....152

4.3 Relative Permeability and Saturation Curves…….....…154

4.4 Wettability Measurement…….…156

4.5 Effect of Amott-Harvey Index on Oil Recovery……..156

4.6 Buckley-Leverret Calculations……...159

4.6.1 Overall Recovery Efficiency…….…….167

4.6.2 Calculation of Displacement Efficiency……168

4.6.3 Mobility Ration…….….168

4.7 Results of Numerical Simulation……..…...170

4.7.1 Streamline Flow…….....171

4.7.2 Instability Condition and Viscous Fingering…….....171

4.7.2.1 Saffman-Taylor Instability.....172

4.7.2.2 Stationary Fingers.....173

4.7.3 Areal Sweep…….....174

5: Conclusion and Recommendation……..176

5.1 Conclusion……..…..176

5.2 Recommendation……..178

Nomenclature……..……...180

References…….....181

Appendices……..…194

List of Figures

2.1. Cross-section of micro-CT image of a sandstone……..……....14

2.2. Visualization of 3D image of a porous rock.……..……..…….…19

2.3. Liquid spreading scenario……..…….....30

2.4. Interfacial tension between a solid surface, wetting phase (water), and non-wetting phase (oil)…….……....35

2.5. Fluid saturation profile in a single water-wet pore…….……....39

2.6. Radius of curvature along the interface of two immiscible fluids.....41

2.7. Capillary pressure-saturation curves for two-phase drainage and imbibition…….……...42

2.8. Elements with different cross-sectional shapes……..50

2.9. Triangular cross-section of a pore space…….…....54

2.10. Imbibition and drainage capillary pressure curves for calculating Amott and USB wettability indices……..…….……....77

2.11 Fundamental Parallelogram.....87

2.12 Fundamental and half-domains.....88

3.1. Niger delta province on the World map…….….90

3.2 Progression of the Niger delta mouth.....91

3.3 Geological Section showing sedimentary layers of the Niger delta.....92

3.4 Lithostratigraphical cross-section across the Niger delta.....93

3.5. Agbada sandstone reservoir core plugs used in the work……..…..……...95

3.6. Soxhlet extraction apparatus……...97

3.7. Core bulk volume measurement…….....98

3.8. Schematic of Helium Porosimeter.....……..99

3.9. Schematic of Darcy's experimental setup for flow in sandpack…….....….101

3.10. Amott wettability test setup……..…….….104

3.11. Schematic of Hassler cell……....105

3.12. Schematic of experimental setup for core flooding……...….106

3.13. Micro-CT scanner at Imperial College, London……..…109

3.14. Picture of basic components of a micro-CT scanner…….....110

3.15. A profile of attenuated x-ray radiation through a sandstone……..…….112

3.16. The x-ray tube in the desktop scanner and rotating sample stage……...112

3.17. Schematic diagram of core scanning experimental setup……...116

3.18. A cross-section of the raw image of a sandstone……....119

3.19. Effect of median filtering on the binarized image…….….120

3.20. Imaged Agbada core sample……...121

3.21. Closed cylindrical reservoir…….....….134

3.22 Doubly periodic lattice for five-spot waterflooding pattern.....134

3.23 Schematic diagrams of oil-water interface.....136

3.24 Geometry of reservoir model and location of wells on regular Cartesian grids.....146

3.25 Simulation Scheme for Weierstrass Elliptic Functions……..……149

4.1. Graphic representation of the experimental porosity and permeability of the cores…...….151

4.2. 2D section of the micro-CT image of Agbada rock sample and the extracted network…...153

4.3. Plot of initial relative permeability……...155

4.4. Plot of relative permeability after wettability alteration……..….155

4.5. Spontaneous imbibition rates for initial wettability determination……..…156

4.6. Experimental oil recovery as a function of Amott-Harvey indices……..…158

4.7. Effect of wettability on waterflood oil recovery……...159

4.8. Semi-log plot of water saturation vs relative permeability ratio……...161

4.9. Fractional flow curve for Bony Light crude oil……...….162

4.10. Fractional flow curve for Forcados Blend crude oil……..……..…163

4.11. Water saturation vs water injection time……..……..165

4.12. Flow Characteristics for five-spot flooding pattern……..……..……...…….172

4.13. Formation of Viscous Fingers in five-spot flooding pattern……...174

4.14. Area of the reservoir swept by injected water in five-spot flooding pattern……..175

4.15. OWC before and after water breakthrough in the production well in five-spot scheme…175

List of Tables

3.1. Fluid and reservoir properties used in the simulations……..……...145

4.1 Mineralogy of the Agbada sandstone cores……...150

4.2. Porosity and permeability of the core plugs measured in the lab……150

4.3. Measured properties of the Agbada core plugs…….151

4.4. Water composition……....152

4.5. Properties of the crude oils……..….152

4.6. Calculated transport properties for the Agbada core samples studies….……....153

4.7. Experimental relative permeability values before wettability alteration……..154

4.8. Experimental relative permeability values after wettability alteration…….…155

4.9. Summary of laboratory wettability measurement using Amott method……..…156

4.10. Summary of Amott-Harvey wettability effects on waterflood oil recovery…….....157

4.11. Water saturation and ration of oil/water relative permeabilities…….....…159

4.12. Plotting data for Bony Light crude oil……..……..….161

4.13. Plotting data for Forcados Blend crude oil…….....…...……..….162

4.14. Distances from injector well to producer well at S_w 60% to 70%.....164

4.15. Shock front and relative permeabilities calculated from fractional flow data……169

Chapter 1

Introduction

The world is facing growing challenges in oil and gas supply in order to sustain growth in energy demand and the economy. Growth in global population and industrialization in developing countries will result into increase in global energy consumption and hence further pressure on the available oil resources. Oil producing companies are encountering increasing difficulties and challenges in accessing new conventional reserves, and are therefore turning to more complex developments like the deep and ultra-deep offshore to deliver growth and boost production to meet the increasing energy demand. However, even the huge oil and gas reservoirs discovered in deep and ultra-deep offshore will only yield about 30 - 40% recovery by primary reservoir energy but the problem of recovery of a greater percentage of what is left behind will persist.

Waterflooding is by far the most widely applied method of improved oil recovery over the years with good results in conventional and unconventional (tight oil) reservoirs. Waterflooding when properly applied can increase production from conventional oil reservoirs by over 50 percent. A lot of unconventional plays (tight oil) are in high decline. By implementing waterfloods, one can lower the declines in these fields and increase reserves.

An understanding of the properties of the oil bearing rock and the reservoir fluids, interactions between the rock and the fluids, and in particular, multiphase flow, is very essential in the choice, design, installation and management of projects for enhanced oil recovery. Multiphase

flow processes in natural porous media or synthetic porous materials is a common phenomenon in many diverse fields of science and engineering. Such fields include agricultural, aeronautical, biomedical, ceramic, chemical, and petroleum engineering, food and soil sciences, as well as in porous metallurgy. Typical examples of great practical interest and economic importance are production of oil and gas from reservoir rocks, underground water flow and transport of inorganic pollutants in unconsolidated soil formations and their removal through remediation process, water flooding, and/or gas injection in oil reservoirs.

In order to understand rock and fluid properties and their interactions at the porescale, one needs to understand the structure of the pore space and its spatial configuration. Pore-network models have become very useful in understanding the physics of porous media flow. Network models are practical reservoir description and simulation tools used to study a variety of two- and three-phase displacement processes (Blunt, 2002; Unsal et al., 2006; Clemens et al., 2013; Berg et al., 2013; Piller et al., 2014; Armstrong et al., 2015; Liu et al., 2015). Pore-scale modeling has been used successfully to predict many different properties, such as two- and three-phase relative permeability and wettability impact on reservoir fluid distributions. From rock samples, methods have been developed to analyze the pore space and extract geologically realistic networks. These methods have been applied to analyze recovery at the field scale, demonstrating the potential of waterflood and recovery trends with wettability in different types of petroleum reservoirs.

Pore-network modeling is now established as a theoretical compliment to special core analysis. It is being used in the industry to assign multiphase flow properties in reservoir models and to predict how these properties vary with rock type and wettability. Using physically-based

properties that properly capture the pore network and wettability variations in the reservoir, adequate prediction of variations in oil recovery trends by waterflooding can be made. Understanding the impact of rock wettability on multiphase flow of oil and gas in the reservoir is very important in many enhanced oil recovery (EOR) processes.

Multiphase flow in porous media is a complex process which involves many and usually unpredictable phenomena. Many hydrocarbon reservoir rocks have different orientations and matrix block sizes (Bear, 1972). Therefore, an understanding of how water, oil and gas move through them is necessary for optimizing enhanced hydrocarbon recovery and remediation of oil spills. The macroscopic transport properties of multiphase flows are determined not only by the geometry and topology of the porous medium, but also by the spatial distribution of wettability and the extent of its variation in individual pore space. Wettability may vary spatially owing to the maturity of the crude oil and variations in its chemical composition, mineralogy, and surface roughness of the rock grains (Morrow, 1975; Dixit et al., 1999).

The ultimate recovery of oil and other non-aqueous phase liquids (NAPLs) depends on the residual saturations and relative permeabilities of each of the phases. In two-phase flow, one phase will wet the porous medium more than the other phase. This wetting phase occupies the smaller pores, crevices, and corners while the non-wetting phase occupies the larger pores with the exact mix determined by the capillary pressure. No matter the pair of fluids used (gas/water, oil/water, gas/oil) the positioning of the fluids will be somewhat identical at identical saturations. On the other hand, for three-phase flow there will be an intermediate wetting phase which will be positioned uniquely in the porous medium, leading to a whole new regime of flow paths

(DiCarlo, 2000). These variations in pore scale positioning of each fluid directly affect the important macroscopic properties of relative permeability, residual saturation and oil recovery.

Starting with the approach pioneered by Fatt in the 1950s (Fatt, 1956a,b,c), a lot of work has been done on pore network models with different representations of pore space used in the investigations of multiphase flow. These models include the disordered networks proposed by Blunt and King (1991); squares proposed by Fenwick and Blunt (1998), Blunt (1998), Dillard and Blunt (1991); regular lattice of cylindrical ducts with cross-sections that are circles proposed by Dixit and co-workers (1999); polygons proposed by Tuller and co-workers (1999); triangles by Hui and Blunt (2000); lattices by Lowery and Miller (1995). These pore network models have been reviewed by, e.g., Berkowitz and Balberg (1993), Sahimi (1995) while Blunt (2001) provides a good bibliography. Most of these pore networks are stochastically generated and usually do not give accurate representation of natural permeable media. However, a wealth of information about the microstructure of real formation is obtained nowadays with the use of advanced imaging techniques such as micro-focused computed tomography (CT) (Coles et al., 1994; Hazlet, 1995), and serial sectioning (Lin and Cohen, 1982). These have led to a tremendous increase in pore network model capabilities (Øren et al., 1998).

Few, if any, hydrocarbon reservoirs are strongly water-wet and many soils contaminated by oil often display oil wet characteristics. This is because the prolonged contact of oil with the solid surface allows surface-active oil components to adhere to the solid surface, changing its wettability (Buckley et al., 1998). Micro-model studies (Lenormand, 1983) have established different displacement mechanisms for multiphase flow in strongly water-wet media, and have

been used in pore-scale models to explain a variety of phenomena, including relative permeability hysteresis, and trends in residual oil saturations (Jerauld and Salter, 1990; Blunt, 1997).

The wetting condition of a reservoir rock plays a significant role in determining transport properties such as capillary pressure, relative permeability and oil recovery. Many experimental investigations on the impact of wettability have been conducted and several excellent review papers are available (Anderson, 1987a,b; Morrow, 1990; Jadhunandan, 1990). Network modeling, where displacement is simulated through a lattice of pores connected by throats, does make predictions of the microscopic fluid distribution and relates this to macroscopic parameters, such as wettability index and oil recovery (Fenwick and Blunt, 1998; Dillard and Blunt, 2000; Tuller et al., 1999; Øren et al., 1998; Dixit et al., 2000; Al-Futaisi and Patzek, 2003; Øren and Bakke, 2003; Piller et al., 2014). It is therefore, a useful tool for understanding the impact of rock structure and wettability on multiphase flow.

Kovscek et al. (1993) proposed a theoretical model for wettability alteration after primary drainage where areas of the pore space in direct contact with oil changed their oil/water contact angle for waterflooding, while water-filled regions remained water-wet. This model has been applied in network modeling to explore the effects of wettability on relative permeability and waterflood oil recovery (Fenwick and Blunt, 1998; Tuller et al., 1999; Øren et al., 1998; Dixit et al., 2000; Kasiri and Bashiri, 2011; Gharbi and Blunt, 2012; Fatemi and Sohrabi, 2013; Falode and Manuel, 2014).

McDougall and Sorbie (1995, 1997) and Sorbie et al., (2011) investigated trends in relative permeability and oil recovery efficiency with a regular cubic network. Recovery was shown to be maximum in a network where half the pore space was oil-wet. Other studies have also been carried out to investigate relative permeability characteristics and trends in oil and gas recovery (Parvazdavani et al, 2013; Ghoodjani and Bolouri, 2014).

Jadhunandan and Morrow (1995) investigated the relationship between wettability and waterflood oil recovery in a series of Berea cores. They used crude oil as a wettability-altering agent. Their study showed that oil recovery by waterflooding initially increased and then decreased as the wettability changed from strongly water-wet to oil-wet, with maximum recovery observed at weakly water-wet conditions. Using geologically realistic network of Berea sandstone, Jackson et al. (2003) predicted the recovery trend as a function of wettability.

Rostami et al (2008) carried out an experimental study of wettability effects on oil recovery and residual saturations during gas assisted gravity drainage and subsequent water flooding mechanisms. Analysis and interpretation of the results obtained in terms of saturation profile, oil recovery at break through time, final oil recovery and residual saturations shows that fluid injection rate and wettability played a major role on phase distribution and fluid displacement mechanism.

.

.Al-Raoush (2009) investigated the impact of wettability of porous media on pore-scale characteristics of residual non-aqueous phase liquids (NAPLs). Findings indicate that spatial variation in wettability of porous media surfaces has a significant impact on pore-scale characteristics of residual NAPL blobs in saturated porous media systems.

Raeesi and Piri (2009) used a model 3-D network of interconnected pores and throats of various geometrical shapes, representing the pore space of Berea and Saudi Arabia reservoir sandstone to investigate the impact of wettability and trapping on the relationship between interfacial area, capillary pressure and saturation in two-phase drainage and imbibition processes. They showed that in a strongly water-wet system, a sharp increase is observed at the beginning of water flood, which shifts the area to a higher level than primary drainage. As the wettability of the system changes from strongly water-wet to strongly oil-wet, the trapped oil saturation decreases significantly. Starting water flood from intermediate water saturations, greater than the irreducible water saturation, can also affect the non-wetting phase entrapment, resulting in different interfacial area behaviors.

Oil recovery pattern during gravity drainage processes in heterogeneous porous media depends strongly on wettability. Zendehboudi et al. (2011) investigated the effects of wettability in fractured and homogeneous porous media during free-fall gravity drainage (FFGD) and controlled gravity drainage (CGD) conditions. They showed that different wettability conditions govern the oil recovery mechanism during FFGD and CGD processes. Also, obtained results showed that the wetting properties of the test fluid considerably affected the matrix-to-fracture transfer and the fluid saturation, with the water-wet conditions favoring oil recovery for both FFGD and CGD processes. Also, Parsaei and Chatzis (2011) through a systematic experimental study investigated the impact of reservoir wettability variations at the macroscopic scale on oil recovery efficiency in gravity-assisted inert gas injection (GAIGI) process for tertiary recovery of residual oil by waterflooding. Obtained experimental results showed that for a positive oil-spreading coefficient, the continuity of water-wet portions of the heterogeneous porous medium

favors the tertiary oil recovery through the film flow mechanism. In addition, owing to the high waterflood residual oil content of the heterogeneous media tested, the oil bank formation occurred much earlier and grew faster, resulting in a higher oil recovery factor.

Zhao et al. (2011) investigated the impacts of wettability on waterflood oil recovery using a capillary pore-scale network model derived from micro-CT images of different rock types. They reproduced the experimental results obtained by Jadhunandan and Morrow and validated the pore-scale model used to simulate flooding cycles. From the results of their investigation they concluded that for a uniformly-wet system, oil recovery increases as the system becomes less water-wet and reaches a maximum for oil-wet conditions where recovery is approximately constant for contact angles greater than 100^0. In water-wet systems oil recovery decreases as initial water saturation increases whereas in oil-wet systems oil recovery initially increases and then decreases. Optimal recovery occurs when a small fraction of the system is water-wet.

Spontaneous water imbibition into the matrix blocks is known as the main mechanism for increased oil recovery from naturally fractured oil reservoirs. The rate of oil recovery and its ultimate value is mostly affected by wettability of the rocks and their pore structure. Rezaveisi et al (2012) utilized a novel experimental model to study the imbibition mechanism under different wettability conditions in naturally fractured formations. The results obtained show that presence of a small fraction of oil-wet rock grains drastically affects oil recovery by capillary imbibition.

Successful reproduction of experimental results is possible using a combination of representative networks and an improved understanding of pore-scale displacement processes. However, several studies have used either cubic networks or a relatively homogeneous network that

represent just one sandstone - Berea. Recent development of high-resolution imaging capabilities has enabled different rock types to be studied that serve as the basis for predictions of flow and transport properties (Arns et al., 2004; Knackstedt et al., 2006; Al-dhahli et al., 2011; Blunt et al., 2012; Piller et al., 2014). The pore structure of a wide range of rock samples can now be determined using Micro-CT imaging. This project will extend previous studies to investigate the effects of wettability on waterflood oil recovery using a network derived from micro-CT image of the Agbada rock system.

1.2 Aims and Objectives

The aim of this research is to determine the petrophysical properties of Agbada sandstone petroleum reservoir rock, wettability of the system and its effects on oil recovery by waterflooding, and to develop a new mathematical model for the simulation of oil recovery by waterflooding.

The specific objectives of the study are:-

I. To determine the petrophysical properties of porosity, permeability and relative permeability of Agbada sandstone reservoir rock using conventional laboratory methods.

2. To compare/validate the data obtained above using pore-network modeling approach whereby the pore network structure extracted from 3-D image scan of the rock sample is used to determine the said properties

3. To establish the wettability of the Agbada sandstone reservoir rock samples studied by waterflooding, and determine the amount of oil recovered using the Buckly-Leverret displacement method

4. To propose a model based on elliptic functions that can be applied for the simulation of waterflooding performance. The proposed modeling scheme will be executed on Wolfram Mathematic software. .

By extending the analysis of the effects of wettability on the macroscopic relative permeabilities, capillary pressure, trapped oil distributions, and flow regimes during displacement of oil by water using a faithful representation of the pore space of the Agbada sandstone, a proper understanding of the dynamics of multi-phase flow in the Agbada porous reservoir rocks can be acquired, which is very essential for designing projects for enhanced oil recovery by waterflooding and/or gas injection, optimizing oil recovery, and remediation of oil spills

In this work a literature review of the fundamentals of fluid flow through porous media, pore-scale modeling and effect of wettability on oil recovery efficiency are given in Chapter 2. In Chapter 3, the apparatus and materials are discussed, and the series of experiments performed in order to determine the petrophysical properties and characterize the initial wettability state of the Agbada sandstone and the procedure for its alteration are presented. An understanding of how the injected fluid displaces the oil to the production wells is very essential for the management of water flooding in oil reservoirs. This aids the optimization of the oil recovery process and identification of possible allocations of new injection and production wells. Prediction of the configuration and movement of fluids in the reservoir is a very complex task. The solutions are sensitive to the grid system because the fluids move between discrete control-volumes, and the numerical scheme should be carefully chosen. From the experimental data obtained in this study, a computation of waterflood oil recovery using the Buckley-Leverett fractional flow theory. The

results of the experiments, computations and simulation are presented and analyzed in Chapter 4. Finally, Chapter 5 discusses the conclusions and recommendations of the study.

1.3 List Publications

The following is a list of journal papers prepared as part of this work:

1. Wopara, O. F., Iyuke, S. E. and Dandekar, A., (2015). Pore-Network Modeling and Prediction of Flow and Transport Properties in Porous Media. 37th International Symposium APPLICATION OF COMPUTERS AND OPERATIONS RESEARCH IN THE MINERAL INDUSTRY, Fairbanks AK, USA pp. 952 – 961.
2. Wopara, O. F., Iyuke, S. E., Obah, B., (2014). Review of Studies on Pore-Network Modeling of Wettability Effects on Waterflood Oil Recovery. Submitted to Journal of Petroleum and Gas Engineering. Manuscript Number JPGE/14.04.15/0222. **Under review.**
3. Wopara, O .F., Iyuke, S. E. (2015. Prediction of Flow and Transport Properties in Porous Media. Submitted to Inter J of Oil, Gas and Coal Tech (IJOGCT), Paper Reference IJOGCT-132436. **Under review/revision**.

Chapter 2

Literature Review

2.1 Introduction to Network Models

Pore-network models are mechanistic models that idealize the complex pore space geometry of the porous media. They are used as effective tools to study and predict macroscopic properties from fundamental pore scale physics. Because of the complex nature of porous media, it is practically not possible to model the behavior of fluids in these systems.

Constructing a pore-network model involves defining its structure and geometry, i.e., the locations of pore bodies (and hence pore-throat length distribution), pore-body size distributions, throat-body size distribution, connectivity, and the spatial correlation between pore bodies and pore throats (Celia et. al., 1995).

There are two types of pore-network models: quasi-static and dynamic. In quasi-static models a capillary pressure is applied on the network and the positions of fluid-fluid interfaces are calculated ignoring viscous forces, while dynamic models apply inflow rate for each one of the components of the system and calculate the corresponding pressure and the interface positions

Knowledge of the constitutive relationships between macroscopic properties such as relative permeabilities, capillary pressures, and fluid saturations is necessary for understanding the flow of fluids in porous media. These relationships are employed in macroscopic differential

equations to describe transport of fluids in a porous medium system. There are complications in determining these constitutive relationships as they are governed by the pore space, properties of the fluids, and saturation history. Pore-network modeling involves the development of rules that describe the pertinent physical processes and the positioning of fluids in a pore space. The rules are then combined to describe flow and transport in systems approximately tens of pores across, representing samples of around 1 mm to a few cm cubed. Macroscopic properties are computed and then use pore-scale modeling to predict relative permeability and capillary pressure as a function of saturation.

Fatt (1956a,b,c) in the 1950s initiated this approach by using a regular 2D network to obtain capillary pressure and relative permeability curves for drainage as a function of average saturation by using the Young-Laplace equation. Since then, the capabilities of pore network models have increased tremendously and have been applied to describe many different physical processes in a pore space.

Micro-model experiments of drainage and imbibition have allowed the pore-scale physics of displacement to be understood. Lenormand et al. (1983) used models with rectangular cross-section capillaries to observe and describe the displacement processes in imbibition that are still at the foundations for network modeling – piston-like displacement, snap-off and cooperative pore-body filling. Advances in pore-scale network modeling have been reviewed by Berkowitz and Balberg (1993), Sahimi (1995), Blunt (2001), which provide good bibliography while Koplik (1982), Jerauld and Salter (1990), Heiba et al. (1992), and Øren et al. (1998) give excellent description of this approach.

2.2 Description of the Pore Space

It is important to have a reliable physically-based tool that can provide reasonable estimates of macroscopic properties. For a theoretical or numerical approach, a detailed understanding of the multiphase displacement mechanisms at pore level and an accurate and realistic characterization of the structure of the porous medium are needed. The prediction of macroscopic transport of immiscible reservoir fluids is therefore possible if there is an adequate description of the essential geometry and topology of the pore space, and a sufficient representation of the multiphase flow physics. Many workers have proposed different statistical and process based techniques to describe the geometry of the pore space (Biswal et al. 1999; Øren and Bakke, 2002). Earlier network models considered the pore space as a collection of capillary tubes and provided simple analytical solutions to predict flow properties such as permeability. These simplified models could not capture the interconnectivity of the pore space. Therefore, 2D and 3D networks that would provide more realistic representation of the pore space were developed (Fatt, 1956a,b,c). Also direct computed tomography (CT) images and depositional models are used to extract a pore space model from a sample of sedimentary rock (Dunsmuir et al., 1991; Dong, 2007). Figure 2.1 shows an example of a 3D pore space of a sandstone.

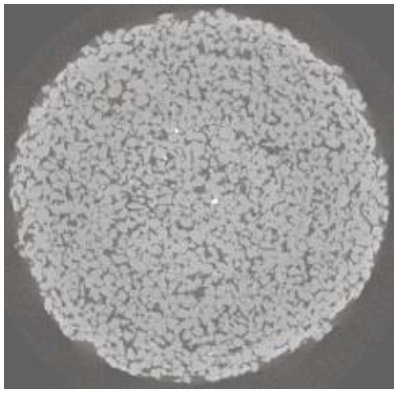

Figure 2.1: Micro-CT image of a sandstone

Multiphase flow can be simulated directly on 3D pore-space images by solving Navier-Stokes equations or by using Lattice-Boltzmann techniques. These images are commonly generated using X-ray computed tomography (Hazlet, 1995; Arns et al., 2004; Berg et al., 2013; Piller et al., 2014), stochastic micro-structural modeling, (Adler et al., 1990; Liang et al., 1998; Okabe and Blunt, 2004) or process-based simulation of rock forming processes (Bryant et al., 1993, Bakke and Øren, 1997; Øren and Bakke, 2003; Jin et al., 2003). These images are then used to compute macroscopic flow properties by solving numerically the continuum flow equations governing fluid transport. Several single-phase properties such as permeability, electrical resistivity and nuclear magnetic resonance (NMR) responses have been predicted from 3D images (Øren et al., 2002; Arns et al., 2004; Knackstedt et al., 2004, Sakellariou et al., 2007) and these have been shown to be in good agreement with conventional laboratory measurements (Arns et. al., 2001; 2002 and 2004). For capillary dominated flow with multiple phases, these methods are very rigorous and computationally expensive. Nevertheless, they provide effective parameters at the pore scale to be used in network modeling. In network modeling, macroscopic equations, such as Darcy's law, are not invoked directly, but emerge from averaging the relevant pore-scale physics.

An alternative approach to the prediction of transport properties directly on 3D images is the use of pore-scale network models (Fatt, 1956; Chatzis and Dullien, 1977; Bryant et al., 1993; Blunt et al., 2002; Blunt 2012; Piller et al., 2014). For accurate predictions they should be derived from 3D images (Lindquist et al., 1996; Bakke and Øren, 1997; Delerue et al., 2002) so as to make them topologically similar to the original samples. Capillary pressure, relative permeability and formation factor were predicted from network models and have been shown to be in good

agreement with experimental data (Bakke and Øren, 1997; Øren and Bakke, 2003, Valvatne and Blunt, 2004, Piri and Blunt 2005b; Ferrari, 2012; Clemens et al., 2013; Armstrong et al., 2015).

Flow in porous media is visualized by making use of conceptual models of the pore structure in terms of pore spaces and pore throats. Several advances have been made in the construction of realistic representations of porous media. Until recently most networks were based on a regular lattice – typically a cubic lattice with coordination number of six or less. Depending on the lattice of interest the coordination number can be varied by throats elimination or variation from the network (Fischer and Celia, 1999; Dixit et l., 2000), or allowing the throat lengths to vary (Fenwick and Blunt, 1998). All these variations in the throat lengths do not give us a three dimensional image of the network. However, in all these cases the network is still based on a regular topology, whereas the porous medium it is attempting to model has a more irregular structure. To overcome this limitation, studies have been made using networks based on square or cubic lattices but with extra coordination that provide more realistic description of the connectivity. Examples of models that provide pore-network representation include Voronoi networks (Fenwick and Blunt, 1998; Blunt and King, 1990, 1991), Delaunay triangulations Blunt and King, 1990, 1991) and irregular networks that allow a variable coordination number (Lowry and Miller, 1995).

Blunt and King (1990, 1991) generated two- and three-dimensional random networks of interconnected voids to identify the physical properties that affect relative permeability. In 2D networks, random points are placed independently and connected by a network of triangles (Delaunay triangulation). Three-dimensional networks are generated using Voronoi tessellation

polyhedra surrounding each point placed randomly in the space. The pores are represented by the vertices of the polyhedra and the connection represented by the edges.

Jerauld and Salter (1990) generated a pore-network model with which they performed extensive investigation of relative permeability and capillary pressure, and explained the trends seen using pore-scale network modeling. Using a cubic lattice with circular capillaries they were able to reproduce the features of relative permeability curves seen in experiments. They found that the most important structural property of the network was the size aspect ratio between pore-bodies and throats. This was found to influence significantly the amount of relative permeability hysteresis between flooding cycles as well as the shape of the curves. Also influencing the shape was the spatial correlation of pore and throat sizes, and to some degree the pore size distribution. They found that the coordination number of the system (number of paths connected to a pore body) had effect on relative permeability predictions. Coordination number ranged from 3 to 12 with an average of 6. Increase in the coordination number within the pore structure reduced the trapped residual phase as a result of higher probability of maintaining phase continuity.

A random distribution of points within the model area makes it possible to construct a network from the triangulation of these points that better reflects the real porous media of interests. This procedure was used by Jerauld et al. (1984a; 1984b) to construct random networks from Voroni diagrams. From an initial coordination number of more than 15 an average coordination number of 6 was obtained by removing the longest throats. However, little difference in relative permeability was observed when comparing to regular networks (Jerauld and Salter, 1990). Blunt and King (1990; 1991) constructed networks using a similar approach.

Another approach is to construct a random network with the connectivity based on a representation of a real porous medium. Having obtained a three-dimensional representation of the porous medium from a pixellated image of pore and grain at a given resolution, a network of pores and throats is constructed, with properties such as shape and volume assigned to each element in the network that mimics the three-dimensional image.

A three-dimensional description of a pore space can be obtained in many ways, such as constructing the pore structure directly, combining a series of two-dimensional sections to form a three-dimensional image (Adler et al., 1990, 1992) or direct x-ray microtomography imaging of the three-dimensional pore space at resolutions of around a micron. This method is accurate to the resolution of the imaging machine. This method, however, to date is not used for routine core analysis. On the other hand two-dimensional thin sections are commonly used. Porosity and two-point correlation function can be measured from these sections and used to generate a three-dimensional image with same statistical properties. The advantage of this is its generality which allows for description of a large variety of porous media (Ioannidis and Chatzis, 2000, Masad et al., 2000; Hilpert and Miller 2001; Vogel and Roth 2001). In most of these works, an equivalent network is not actually constructed: instead flow simulations are performed directly on the image of the pore space. For example, Adler et al. (1990, 1992), using a statistical technique to generate a three-dimensional pore space that had the same porosity and two-point correlation function as thin section images, modeled Fontainebleau sandstone and successfully predicted absolute permeability and electrical properties. The disadvantage is that the simulated pore space may not capture the long-range connectivity of the pore space imposed by the geological processes that formed it. This is because it is difficult to impose this connectivity through matching two-point

statistics alone. This therefore calls for an alternative approach – reconstruction of the porous medium by modeling the geological processes by which it was formed. Figure 2.2 shows the 3D pore space of different Berea models.

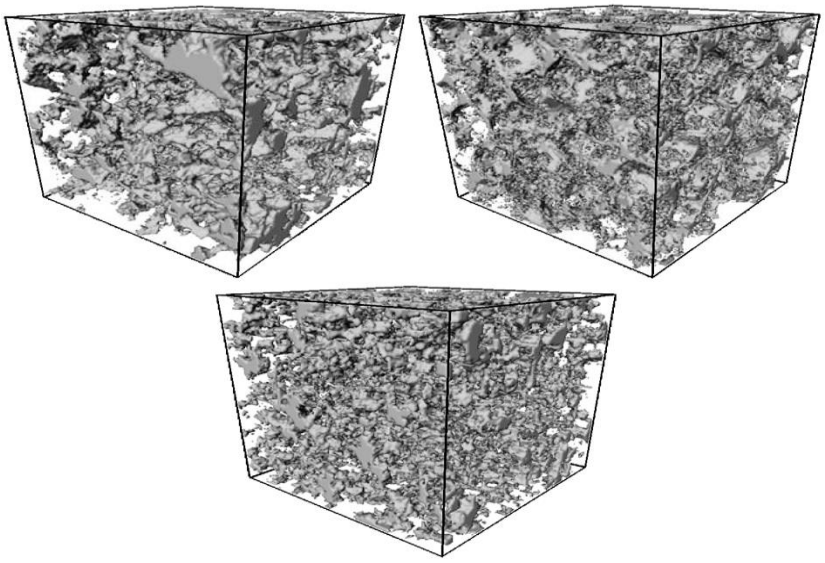

Figure 2.2: Visualization of 3D images of a porous medium; left - micro-tomographic (CT), right - process-based (PM), and bottom - statistical model (SM) (Dong, 2007)

All the methods described above do not capture the characteristics of real porous media. Bryant et al. initiated the use of geologically realistic networks (Bryant et al., 1992, 1993; Bryant and Raikes, 1995). They based their models on a random close packing of equally-sized spheres. They were able to predict the absolute and relative permeability, capillary pressure, elastic and electrical properties, and to predict the trend of relative permeability with porosity for Fontainebleau sandstone. This represented a major breakthrough in pore-scale modeling, as genuine predictions of fluid transport and flow properties were made for the first time. They showed that spatial correlations in the pore size distribution were important for correct predictions: using the same pore size distribution, but assigning it at random to the throats in the network gave erroneous predictions of permeability. The major problem was that application of

this work was restricted to simple media that were, to a good approximation, composed of spherical grains of same size with a constant coordination number of 4.

Øren, Bakke and co-workers at Statoil extended this approach to a wider range of sedimentary rocks (Øren and Bakke, 1997, 1998, 2002; Biswal et al., 1999; Lerdhal et al., 2000). They developed a reconstruction method, where the packing of spheres of different size was simulated. They derived the grain size distribution from analysis of either a direct three-dimensional image of the pore space from micro CT scanning of thin sections of the rock of interest, or from simulating the geological processes by which the rock was formed. Biswal and co-workers (1999) compared the pore space derived from this geological reconstruction of Fontainebleau sandstone with an image obtained from micro-tomography. After studying two stochastic models based on correlation function representation, they proved that the stochastic models differed strongly from the real sandstone in their connectivity properties. The geological reconstruction captured adequately the pore spaces connectivity of the rock and could therefore give accurate prediction of transport properties (Arns, 2004; Blunt 2012). Øren and co-workers (Øren and Bakke, 1998; Bakke and Øren, 1997) simulated multiphase flow by using the geological reconstructions to construct topologically equivalent networks and predicted relative permeability for a variety of water-wet sandstones, showed promising results for a water-wet reservoir rock sample.

Object-based modeling technique has been used to simulate the actual rock-forming process. Coehlo et al. (1997), Pillotti (2000), Latham et al. (2000) and Jia and Williams (2001) described how to simulate the deposition of grains of arbitrary shapes, which in principle enables the

reconstruction technique to be applied more generally. Other authors have also predicted single and multiphase properties using sphere packs (Thomson and Fogler, 1997; Patzek, 2001; Hilpert and Miller, 2001).

However, the application of reconstruction methods to reservoir samples has three main constraints. First, the reconstruction algorithm is based on explicit simulation of the geological processes by which the rock is formed. This is very tasking for complex systems, involving micro-porosity and clays and a variety of different sedimentary processes. Statistical reconstruction methods are more general, since they require only a two-dimensional image of the system, and have been successfully applied to non-clastic rocks (Bekri et al., (2000). For now, however, they are principally used to predict single-phase flow simulated directly on the pore-space reconstruction. In principle though, this could be extended to study multiphase flow properties using an equivalent network representation of the pore space. The second problem, for any approach, is that characterization of the pore space requires detailed thin section analysis that might not be available or is difficult to obtain. Third, the appropriate characterization of pore shape and wettability is not fully understood.

From the above we can conclude that a description of the pore space with a disordered connectivity based on the real system of interest (Agbada sandstones) is sufficient to produce a predictive model. Network models based on a regular lattice can always be tuned to match particular experimental results of interest. Indeed, many studies have used different empirical methods to adjust network model parameters to experimental data (Rajaram et al., 1997; Fischer and Celia, 1999; Dixit et al., 1998, 1999, 2000; Blunt, 2007; Ferrari, 2012; Clemens et al., 2013).

This provides some assurance that pore-scale models do represent flow and transport properties adequately, but the matching process is generally non-unique. This implies lack of guaranty that the geometry of the pore space is close to the real system, and as a consequence there is little confidence that the model could be used to predict other properties accurately. Since it is difficult to represent accurately the real geometry and topology of the pore space of the Agbada sandstone, this approach is used in the study to make genuine prediction of wettability effects on oil recovery by waterflooding.

2.3 Multiphase Drainage

Multiphase flow behavior is a key parameter in terms of planning and assessing the economics and technical feasibility of oil and gas production projects. Predicting the detailed behavior of multiphase flow in porous media still presents a challenging domain of increasing interest. Through the past years, many models of fluid displacement mechanisms including fluid/fluid and fluid/solid interface description have been proposed and integrated in numerical modeling schemes like pore network models.

2.3.1 Two-phase Drainage

Two-phase displacements in porous media have frequently been studied over the last two decades. The main reason for this is the great variety of structures observed when changing the physical parameters of the fluids like viscosity contrast, wettability, interfacial tension and displacement rate. From the point of view of modern physics the process is of great interest and it has a large number of practical applications in many fields of science. Most often mentioned is the relation to the oil industry where the flow of oil, gas and water in reservoirs are of great

technological importance. It is surprising that today's petroleum engineering is not able to recover more than about 30 – 40% of the oil in a reservoir. Other fields of applications are hydrology and soil science where there has been much attention to modeling ground water resources and pollution effects of the acid deposition, causing acidification of soils and water.

Madalena et al., (1985) developed a theoretical simulator of immiscible displacement of a non-wetting fluid by a wetting one in a random porous medium. The porous medium is modeled as a network of randomly sized unit cells of the constricted-tube type. Under creeping-flow conditions the problem is reduced to a system of linear equations, the solution of which gives the instantaneous pressures at the nodes and the corresponding flowrates through the unit cells. They obtained a pattern and rate of the displacement by assuming quasi-static flow and taking small time increments. They used a sand-pack as the porous medium for the simulations, with porosity 0.395 and grain sizes in the range from 74 to 148 microns. In addition to the residual saturation of the non-wetting fluid, the simulator predicts the time required for the displacement, the pattern of the transition zone, the size distribution of the entrapped ganglia, and the acceptance fraction as functions of *Ca*, *k*, and the porous-medium geometry.

Vahid et al. (2010) compared predictions of several pore-scale codes for single- and two-phase flow for the first time. Firstly, using two implementations of lattice-Boltzmann method (LBM) and a finite-difference based code (FDDA) they predicted single-phase flow in Fontainebleau sandstone and dolomite samples. They then obtained pore-scale drainage for two fluid phase configurations using a novel level set method based progressive quasi-static (LSMPQS) algorithm for capillarity dominated flow. The resulting fluid configurations were used to

compute relative permeability using the lattice-Boltzmann method (LBM) in each phase as well as formation factor. They demonstrated that the numerical methods compare well with each other and with available experimental results. Numerous other two-phase network models abound in literature and it is not the intention of this thesis to review them all.

2.3.2 Three-Phase Network Models

This section presents a review of previously developed network models for three-phase flow. Heiba et al. (1984) extended the statistical network model and percolation theory of capillary pressure and relative permeabilities previously used for two-phase systems to three-phase flow of oil, water and gas. They used a Bethe lattice (tree) as network to represent the porous medium. Relative permeabilities were calculated by Stinchcombe's formula (Stinchcombe, 1974) using series approximations from percolation theory. Only a single phase could occupy a throat. A given fluid can flow only if among the pore segments it occupies at least one set that is connected from inlet to outlet, i.e. only if a continuous flow path has been established for that fluid phase. Accessibility and local entry capillary pressure controlled the displacement of one phase by another. Six groups of displacement were considered: gas into oil, oil into gas, gas into water, water into gas, water into oil, and oil into water. They investigated two spreading systems: in the first one gas and water were displacing oil while in the second case water and oil were displacing oil and gas. They showed that the gas and water relative permeabilities were functions of only their own saturations. Oil layers prevented the direct contact of gas and water. Oil isoperms were found to be strongly curved, meaning that the oil relative permeability was not only a function of its own saturation. Extensions of the theory to handle the complications involved by the effects of wettability and phase swelling due to mass transfer were also

discussed. It was concluded that three-phase relative permeabilities are generally path functions rather than state functions (function of saturation only) except in particular situations such as when two phases are separated by the third. This model used rather simple networks and displacement rules.

Soll and Celia (1993) developed a computational model of capillary-dominated two- and three-phase flow at the pore level to simulate capillary pressure-saturation relationships in a water-wet system. Regular two- or three-dimensional networks of pores, connected to each other by throats, were used to represent the porous medium. Hysteresis was modeled by using advancing and receding contact anglesvalues for each pair of fluids. Every pore was able to accommodate one fluid at a time as well as wetting layers. Viscous forces were considered to be negligible but the effects of gravity were included to modify the local capillary pressures. In order to reproduce their micromodel experiments (Jadhunandan and Morrow, 1995), oil as a spreading phase was allowed to advance ahead of a continuous invasion front. Several pores could be filled simultaneously. This model was the first to incorporate layer flow in three-phase network modeling albeit in a rather ad hoc fashion. The results were compared with capillary pressure-saturation results and fluid distributions from the two- and three-fluid micromodel experiments. Predicted two-phase air-water and oil-water capillary pressures were in good agreement with measured values (Jadhunandan and Morrow, 1995) although the model did not so successfully match three-phase data. The model was not used to calculate relative permeabilities.

Øren et al. (2003) described details of the pore level displacement mechanisms taking place during immiscible (tertiary) gas injection into waterflood residual oil and incorporated them into

a two-dimensional strongly water-wet square network model with rectangular links and spherical pores in order to compute oil recovery in spreading and non-spreading systems. Simulated recoveries compared very well with the measured values from micromodel experiments (Dixit et al., 1999; Moulo et al., 1999). The authors described a double drainage mechanism where gas displaces trapped oil that displaces water allowing immobile oil to become connected thereby enhancing oil recovery. Oil recovery decreased with decreasing spreading coefficient. When the systems are non-spreading, direct gas-water displacement was leading to early gas breakthrough and low oil recovery. In spreading systems oil reconnection was more effective and direct gas-oil displacement was preferred.

Pereira et al. (1996) developed a dynamic two-dimensional network model for drainage-dominated three-phase flow in strongly water- and oil-wet systems when both capillary and viscous forces were important. The displacement mechanisms in spreading and non-spreading systems were described by generalization of two-phase displacement mechanisms. Both pores and throats were assumed to be lenticular in cross section allowing wetting and spreading layers to be present. The simulated recoveries at gas breakthrough were compared against measured values in micromodels. As in Øren et al. (2003), a large difference between the recoveries in spreading and non-spreading systems was reported for water-wet cases due to existence of oil layers in the spreading systems. The highest recovery, 85%, was found for the oil-wet case. This was because continuous wetting layers prevented trapping of oil. The oil recovery was much lower, 14%, for the water-wet case in a non-spreading system. This was because there were no spreading layers of oil. Even when layers were present for the spreading system, the oil recovery was much lower, 40%, in a water-wet medium than for the oil-wet case. Water in water-wet

systems played the same role as oil in oil-wet systems - water recoveries in water-wet spreading and non-spreading systems were high. An order of magnitude reduction in the simulated conductivity of the oil layers decreased oil recovery and made the behavior of the spreading system similar to that of a non-spreading system. Also a reduction in initial oil saturation for tertiary gas injection decreased the oil recovery. This was true for both spreading and non-spreading systems indicating that the recovery of the intermediate wetting phase is strong function of saturation history. This was reported to be consistent with experiments by Dria et al. and Oak (1990). It was also concluded that the recovery of the wetting fluid is independent of the saturation history. Relative permeabilities were not calculated in this work.

Paterson et al. (1998) developed a water-wet percolation model to study the effects of spatial correlations in the pore size distributions on three-phase relative permeabilities and residual saturations. A simple site percolation model with trapping was used. In three-phase simulations direct displacement of oil and water by gas and also double drainage were implemented. The model assigned the same volume to all pores and so the fraction of sites occupied by a phase gave its saturation. All the sites were assumed to have the same conductivity regardless of their radii. The simulation results for correlated properties showed lower residual saturations in comparison to uncorrelated ones. Incorporating a bedding orientation to the spatial correlations had a major impact on relative permeability. When the bedding was parallel to the flow direction, the relative permeabilities were greater and residual saturations lower than those when bedding was perpendicular to the flow. This was also the case for two-phase relative permeabilities (Paterson et al. 1998). The effects of spreading coefficient were also studied. It was shown that the less negative the spreading coefficient, the lower the final residual oil

saturation. For more negative spreading coefficients direct gas to oil and gas to water displacements are preferred over double drainage.

Fenwick and Blunt (1998a,b) developed a three-dimensional pore-network to model capillary pressure, relative permeability, drainage and imbibitions of three-phase strongly water-wet systems by using a regular cubic network composed of pores and throats with equilateral triangular or square cross sections. Oil-water and gas-water contact angles were considered to be zero. The model incorporated two and three-phase displacement mechanisms including oil layer flow observed in micromodel experiments. Double drainage was generalized to allow any of six types of double displacement where one phase displaces a second that displaces a third as observed by Keller et al. (1997). The model was able to simulate any sequence of oil, water, and gas injection. Using a geometrical analysis, a criterion for stability of oil layers was derived which was dependent on oil-water and gas-oil capillary pressures, contact angles, equilibrium interfacial tensions, and the corner half angle. It was argued that oil layers could be present even for negative spreading coefficient systems. Using a simple calculation it was shown that the layers are of order of a micron across or thicker in the corners, roughness, and grooves of the pore space. The work estimated conductance of an oil layer which then was used to compute oil relative permeability. It was shown that at low oil saturation the oil relative permeability should vary quadratically with saturation, as observed experimentally (Grader and O'Meara, 1988; Øren et al., 1992; Keller et al., 1997; vanDjike and Sorbie, 2001). An iterative methodology which coupled a physically based network model with a one-dimensional (1D) three-phase Buckley-Leverett simulator was developed in order to find the correct saturation path for a given process with known initial condition and injection fluid (Fenwick and Blunt, 1998). This enabled the

network model to compute the properties for the right displacement sequence. Relative permeabilities for secondary and tertiary gas injection into different initial oil saturations were presented. The resultant saturation paths compared well qualitatively with experimental data by Grader and O'Meara (1988)]. The paths in the oil-water versus gas-oil capillary pressure space were all located in the region where oil layers were stable meaning that oil did not get trapped. Oil relative permeabilities for different initial conditions were different from each other, consistent with several experimental studies (Øren et al., 1998, 1999; Blunt, 1998; Oak, 1990).

Mani and Mohanty (1998, 1999) also used a regular cubic network of pores and throats to simulate three-phase drainage and imbibition in water-wet systems. They considered the pores and throats to be spherical and cylindrical, respectively and fixed the oil-water capillary pressure at its original value during the gas invasion processes. They then tuned the parameters of the network to match two-phase mercury-air experimental capillary pressures for Berea sandstone.

The work had two important features: dynamic simulation of capillary-controlled gas invasion, where it was assumed each phase pressure was not constant across the network; re-injection of the produced fluids at the outlet of the medium into the inlet in order to simulate larger systems. This was used to see whether trapped oil ganglia become reconnected by double drainage to form spanning clusters. The two-phase processes were simulated at low capillary number using traditional quasi-static assumptions. Pressure drops across pores were ignored. The model included fluid flow through wetting and spreading layers. A fixed conductance was assigned to oil layers. For the capillary pressure histories used, no stable oil layers were observed in both spreading and non-spreading systems. Gas invasion was modeled by three displacement

mechanisms: direct gas-water, direct gas-oil, and double drainage. For each displacement a potential was considered, which was the difference between the pressures of two involved fluids, minus the threshold capillary pressure of the displacement. The displacement with the largest potential was carried out first. Re-injection of fluids was simulated by replacing the fluid distribution in the inlet zone by the fluids in the outlet zone. The process was terminated after steady state was reached at the imposed pressure conditions, i.e., when no further gas invasion was possible at the imposed capillary pressure. The final oil saturation in spreading systems was zero. The capillary pressure curves obtained from dynamic and quasi-static simulations were virtually identical. For non-spreading systems with a low oil-water capillary pressure, drainage of water and oil occurred with similar probability. The effect of spreading coefficient and saturation history on three-phase relative permeability was consistent with other network modeling studies (Øren et al., 1998, 1999; Blunt, 1998; Fenwick and Blunt, 1998) and experimental measurements (Amott, 1959; Oak, 1990).

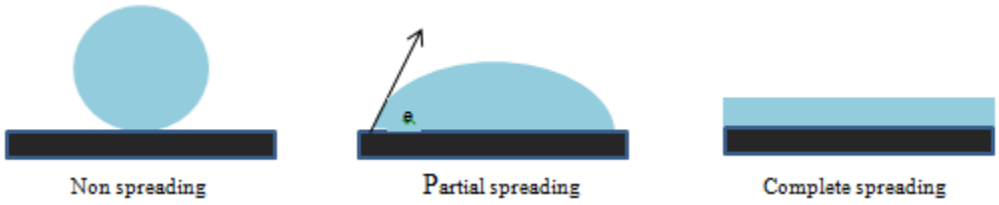

Figure 2.3: Liquid spreading scenario

Laroche et al. (1999a,b) developed a pore network model to predict the effects of wettability heterogeneities with different patterns and spatial distributions on displacement mechanisms, sweep efficiency, and fluid distribution in gas injection into oil and water. A dalmatian type of wettability heterogeneity was used with continuous water-wet surfaces enclosing discontinuous regions of oil-wet surfaces or vice versa. A series of three-phase glass micromodel experiments with different wettabilities were also carried out. Measured oil-water contact angles for the

water-wet and oil-wet surfaces were 0° and 105°, respectively. *n*-dodecane, water, and nitrogen were the three fluids used in the experiments. All the two-phase interfacial tensions, densities, and viscosities were measured. The initial spreading coefficient was 7.3 mN/m and hence the oil was assumed to be spreading. The capillary number throughout the experiments was approximately 10^{-5} indicating capillary controlled displacement. A 2D regular pore and throat network was used to simulate the experiments. All the throats had triangular cross sections while the pores were circular cylinders. The pore and throat size distributions were similar to those of Berea sandstone. Saturations, conductances, and relative permeabilities were calculated using similar techniques to Fenwick and Blunt (1998). The fluid distributions at the end of two- and three-phase simulations were in good qualitative agreement with those found experimentally.

Hui and Blunt (2000) developed a mixed-wet model of three-phase flow for a bundle of capillary tubes. The tubes had different sizes and were equilateral triangle in cross section. Wettability alteration was modeled by changing the wettability of surfaces that came into contact with oil after primary drainage. The model simulated three-phase flow with any combination of oil-water, gas-water, and gas-oil contact angles. In all some ten fluid configurations were considered. Primary drainage, water flooding, and tertiary gas injection were simulated. The effects of wettability, spreading coefficient, and initial oil saturation on relative permeabilities were investigated. Possible configuration changes during each process along with the threshold capillary pressure of each change were presented. The stability of layers in different configurations and capillary pressures at which they collapse was discussed. This approach is extended towards studying 30 different possible fluid configurations in three-phase flow and to incorporate them in a three-dimensional random network model.

Lerdahl et al. (2000) used the technique developed by Bakke et al. (1998) to reconstruct a three-dimensional void space, and then convert it to a pore and throat network, for use in a water-wet network model to study drainage-dominated three-phase flow. Simulated results were compared successfully against the experimental data by Oak (1990). Larsen et al. (1998) used a water-wet three-dimensional cubic pore network model based on the work of Fenwick and Blunt (1998) to simulate a series of micromodel experiments of Water Alternating Gas (WAG) injection processes. All the pores and throats were assumed to have square cross sections. The network model was used in an iterative procedure similar to the one used by Fenwick and Blunt (1998) to find self-consistent saturation paths.

vanDijke et al. (2000, 2001) presented a process-based mixed-wet model of three-phase flow using a bundle of capillary tubes with circular cross sections to study the saturation dependencies of capillary pressures and relative permeabilities for spreading and non-spreading systems. Larger pores were considered to be oil-wet and the smaller ones water-wet. It was shown that, based on interfacial tensions and contact angles, the three-phase saturation space could be divided up to three different regions with a different intermediate-wet phase. The relative permeability of this phase was a function of two saturations. Also the capillary pressure between the most wetting and non-wetting phases is dependent on two saturations. The relative permeabilities of the other two phases were a function of only their own saturation in this region.

vanDijke et al. (2001), expanding on their previous studies on bundles of capillary tubes, developed a regular three-dimensional three-phase network model for systems with different wettability. Every element was allowed to have a different oil-water contact angle and linear

relationship was used to find gas-oil and gas-water contact angles from the oil-water contact angle and interfacial tensions. While layers were not incorporated explicitly in saturation or conductance computations they were allowed to establish continuity of different phases. The model was a cubic array of only throats with a circular cross section. The coordination number could be changed by removing throats from the network. An extensive series of simulations of three-phase flow was performed. For networks with a high coordination number, the saturation dependencies were qualitatively similar to those predicted for capillary bundles. As the coordination number was reduced, connectivity was impaired and trapping became significant. They compared their network simulations with micromodel experiments of WAG where there were repeated cycles of water and gas flooding. To reproduce the results they incorporated multiple displacements where a train trapped clusters may displace each other until there is invasion into a connected phase. They suggested that such multiple displacements were significant in WAG flooding.

.

2.4 Fluid Transport Properties

When the pore space of a porous media is occupied by two or more fluids, two types of flow are possible: miscible and immiscible displacement. In miscible displacement, the two fluids can completely dissolve in each other and there is no fluid-fluid interface. In the case where a fluid-fluid interface exists due to the interfacial tension between fluids, an immiscible displacement occurs as a form of simultaneous flow of the phases that exist in the system (e.g., oil, water, and gas). For miscible displacement, the two phases mix together in a determined proportion and flow as a single phase.

2.4.1 Interfacial Tension and Wettability

The interfacial tension σ, is defined as the work necessary to separate a unit area of two immiscible liquid phases from each other. The interfacial tension or energy barrier between a liquid and air is called the surface tension. The main forces involved in interfacial tension are adhesive forces (tension) between the liquid phase of one substance and either a solid, liquid or gas phase of another substance. Figure 2.4 shows two immiscible fluids (oil and water) in contact with a solid surface, the angle between the interface and the solid surface, θ, and the interfacial tensions between the three phases σ_{ij} (where i,j is oil, water, or solid).

The relationship between the contact angle and tension at the interfaces is given by Young's equation, Adamson (1982):

$$\sigma_{ow} cos\theta = \sigma_{os} - \sigma_{ws} \tag{2.1}$$

where θ = contact angle, the angle of the water/oil/solid contact line.

The contact angle determines which fluid will preferentially wet the solid (i.e., the wettability of a solid by a liquid). A contact angle less than 90° (low contact angle) indicates that wetting of the surface by water is very favorable, and the water will spread over a large area of the surface. Contact angles greater than 90° (high contact angle) means that wetting of the surface is unfavorable to water but favorable to oil and so the surface will be preferentially oil-wet. Wettability therefore is the ability of a fluid to spread or adhere on a rock surface in the presence of other immiscible fluids. Wettability is generally considered to be one of the principal parameters influencing the distribution, saturation and flow of fluids in porous media.

Wettability has a dominant effect in oil recovery by waterflooding and gas injection and in many other processes of industrial and environmental interest. Knowledge of wettability is important in deciding what production strategy needs to be employed for optimum oil recovery. Wettability can also be defined in terms of the contact angle between a droplet of the liquid in thermal equilibrium on a horizontal surface. Depending on the type of surface and liquid, the droplet may take a variety of shapes as illustrated in Figure 2.4. The wetting angle θ is given by the angle between the interface of the droplet and the horizontal surface. The liquid is seemed wetting when $90 \le \theta \le 180$ degrees and non-wetting when $0 \le \theta \le 90$. An angle value of $\theta = 180$ degrees corresponds to perfect wetting and the drop spreads forming a film on the surface.

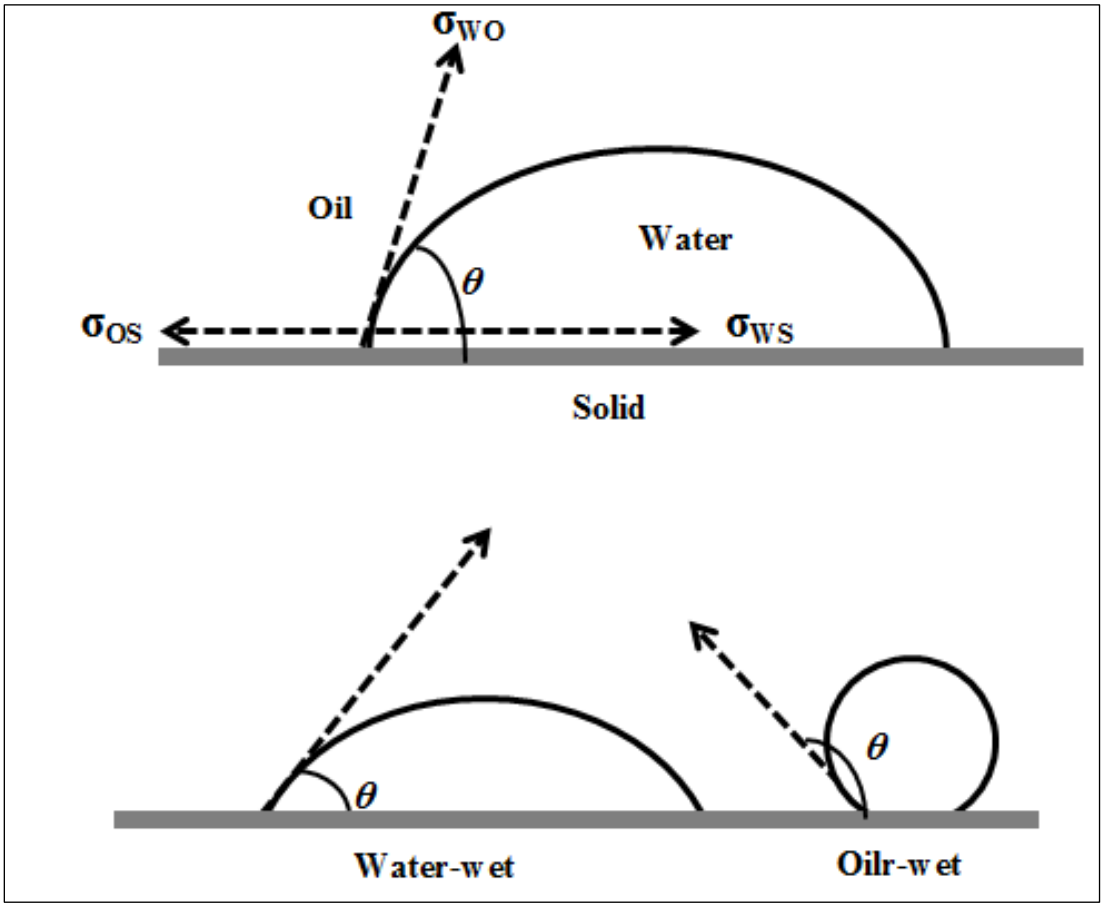

Figure 2.4: Interfacial tensions between a solid surface, wetting phase (water), and a non-wetting phase (oil).

Actually, the wetting angle θ is a thermodynamic variable that depends on the interfacial tensions of the surfaces. For two-phase flow in porous media the wetting angle influences the strength of the capillary pressure. For a wetting angle θ between the interface and the pore wall, the capillary pressure p_c in a pore of size *r* is given as:

$$p_c = \frac{2\sigma}{r}\cos\theta \tag{2.2}$$

In porous media a direct measurement of contact angles is impractical. Wettability and its effects on fluid flow behaviour are manifested primarily through the capillary pressure - fluid saturation relationship. With this in mind an acceptable method of measuring reservoir core wettability can be based on different types of capillary pressure phenomena.

2.4.2 Contact Angle Measurement

There are several methods of determining contact angles. These include the sessile or pendant drop and the Wilhelmy plate methods. These measurement techniques are most useful for measuring wettability effects of pure fluids on clean, smooth mineral surfaces and thus provide qualitative information. However, they do not represent reservoir rocks, because the plates do not account for surface roughness, the large variety of minerals, presence of thin layers of organic materials, and presence of polar substances in the oils. For porous materials, the wicking or capillary rise method is often used (Chibowski and Perea-Carpio, 2002). For spherical particles, methods have been developed to determine contact angles based on force measurements (Zhang et al., 1996; Preuss and But, 1998; Subedi, 2011; Dandeker, 2013), confocal microscopy (Mohammadi and Amirfazli, 2004), and film trapping (Hadjiiski et al., 1996). Wenzel (1936) developed an equation (2.3) to calculate the theoretical contact angle, θ_W, on rough surfaces. The theoretical contact angle is calculated using the contact angle on a smooth surface of the same

material, θ, and the roughness factor, ζ, which is the ratio of true surface area to projected surface area.

$$cos\theta_W = \zeta\, cos\theta \tag{2.3}$$

Cassie (1944) developed two equations to calculate theoretical contact angles on heterogeneous surfaces and porous materials. Equation (2.4) calculates the theoretical contact angle, θ_C, on heterogeneous surfaces with two different contact angles, θ_1 and θ_2, with fractional areas of each surface under a drop, f_1 and f_2. Equation (2.5) calculates the theoretical contact angle, θ_C, on porous surfaces where f_1 is the fractional area solid-liquid interfaces and f_2 is the fractional area of liquid-air interfaces or pores when a drop is placed on the surface.

$$cos\theta_C = f_1\, cos\theta_1 + f_2\, cos\theta_2 \tag{2.4}$$

$$cos\theta_C = f_1\, cos_{\theta 1} - f_2 \tag{2.5}$$

Wenzel's approach is difficult to apply to a non-patterned, rough, porous material because of the need to know the true surface area of the substrate. Cassie's method can be used for porous materials; however it becomes difficult to apply when using a material that is porous with a non-patterned roughness. Both approaches require knowledge of the contact angle on a smooth surface of the same material.

Current measurement techniques are not suitable for making accurate contact angle measurements on rough surfaces due to poor optical resolution at the contact line. Stacy (2009) developed a technique for accurately measuring contact angles on rough surfaces using a sessile drop method. The technique requires a drop profile image which is processed to extract the solid surface and drop interface data. The Laplace-Young equation is numerically integrated to

generate a Laplacian curve which matches the upper portion of the drop profile. The contact angle is then extracted from the Laplacian curve. This technique is advantageous because it removes the dependence of the contact angle measurement from imaging of the contact line.

The general steps involved in using Stacy's method for measuring contact angles include capturing a profile image of a sessile drop on the desired substrate, processing the drop image to obtain the drop interface data and substrate surface data, and finding a solution to the set of first-order, non-linear differential equations which produces a Laplacian curve that matches the drop interface. The solution is found by minimizing the distance between the Laplacian curve and the drop interface data at a point above the contact line.

2.4.3 Fluid Saturation

The wettability of a porous medium depends on the mineralogy of the rock, the composition of the oil and water, the initial water saturation, and the temperature (Buckley et al., 1989; Buckley, 1995; Buckley and Liu, 1998; Dubey and Waxman, 1991; Dubey and Doe, 1993; Wolcott et al., 1993). Saturation of a fluid is simply the fraction or percentage of the void space filled by that fluid (e.g., oil, gas, water, etc.). The fluids in the pore spaces may be wetting or non-wetting. In most reservoirs, water is the wetting phase, but a few reservoirs are known to be oil wet. The wetting phase exists as an adhesive film on the solid surfaces. At irreducible saturation of the wetting phase, the non-wetting phase is usually continuous and is producible under a pressure gradient to the well bore. In a water-wet porous media system, occupation of fluids in a pore may take different forms leading to three types of fluid saturations as shown in Figure 2.4 (Bear, 1972). At very low water saturation, water forms a thin film around the solid surface and isolated

water-rings around the solid contact angle called *pendular* rings. These pendular rings become continuous as the wetting phase saturation increases. The wetting phase might or might not be at irreducible saturation. In Figure (2.5), water in "A" and "B" is pendular. If the wetting phase saturation increases any further, the saturation is called *funicular*. In funicular saturation the non-wetting phase exists as a continuous film throughout the interstices. The non-wetting phase is mobile under the influence of a hydrodynamic pressure gradient. The wetting phase might or might not be at irreducible saturation. In the illustration, the oil in "A" is funicular. As the saturation of the wetting phase increases, the non-wetting phase loses its continuity and forms isolated droplets within the continuous wetting phase. This state is called *insular* saturation. A drop in pressure might or might not cause the insular droplets to collect into a continuous phase. The oil in "B" and "C" is insular. The same concept can be applied to oil-wet porous media systems.

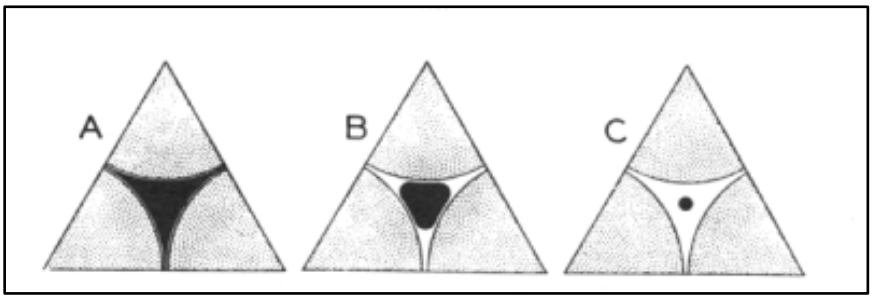

Figure 2.5: Fluid saturation profile in a single water-wet pore. Non-wetting oil (black) and water (blank). (From Levorsen, Petroleum Geology)

Several studies have successfully used network models to investigate the effect of wettability variations on flow at the pore-scale (Mohanty and Salter, 1983; Heiba et al., 1983; Kovscek et al., 1993; McDougall and Sorbie, 1995; Blunt, 1997a,b, 1998; Dixit et al., 1997, 1998, 1999; Hui and Blunt, 2000). These models have progressively captured more of the physics of pore-scale displacement mechanisms.

Displacement of non-wetting fluid from a core plug sample by spontaneous invasion or imbibition of the wetting fluid is a process which depends, in the main, on capillary pressure as a driving force. This process is a feature of the wettability measurement technique proposed by Amott (1959) and used for the generation of wettability indices, to which qualitative terms can be applied.

2.4.4. Capillary Pressure

When two or more immiscible fluids co-exist in a system of capillaries, the combination of surface tension and curvature due to the capillaries causes the phases to experience pressure differences between them. The difference between the pressures of any two phases is referred to as the capillary pressure, P_c (Adamson, 1982), and is defined as:

$$P_c = P_{nw} - P_w \tag{2.6}$$

where P_{nw} is the pressure of the non-wetting phase and P_w is the pressure of the wetting phase.

Capillary pressures can be determined for any two fluid phases; of interest to the oil industry are those for gas-brine, gas-oil and oil-brine systems. In any porous system with two fluid phases present, the wetting phase will always have the lower pressure. Therefore, capillary pressure curves can be used to determine the wetting characteristics of reservoir rocks. It can also be used to evaluate reservoir rock quality, pore throat size distributions and predict fluid saturations in the reservoir.

The capillary pressure is given by Young-Laplace equation as:

$$P_c = P_{nw} - P_w = \sigma_{nww}\left(\frac{1}{r_1} - \frac{1}{r_2}\right) \tag{2.7}$$

where σ_{nww} is the interfacial tension between fluids non-wetting and wetting phases and r_1, r_2 are the principal radii of curvature of the interface, as shown in Figure 2.6..

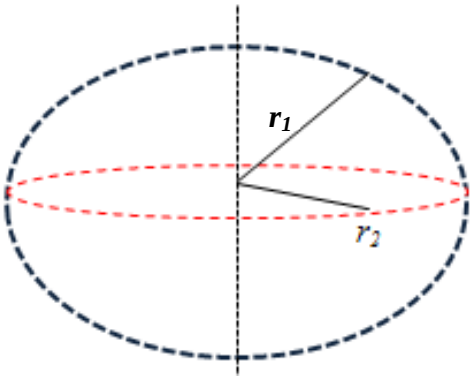

Fig. 2.6: Radii of curvature along the surface of two immiscible fluids

For simplicity, if it is assumed that in a reservoir rock, all the pores and throats have a circular cross-section, from the above equation the capillary pressure can be simply expressed as:

$$P_c = P_{nw} - P_w = \frac{2\sigma_{nww}\cos\theta}{R} \tag{2.8}$$

where R is the mean radius of curvature ($2/R = 1/r_1+1/r_2$).

The capillary pressure is a function of the pore geometry (pore radius and rock texture), fluid properties, wettability, interfacial tension between fluids, density and the amount and location of each phase in the pore space (saturation history). Due to the complexity of natural porous media systems, it is difficult to obtain these parameters analytically. Therefore, the pore space is usually idealized (e.g., capillary tube or uniform spheres) to predict the capillary pressure as a function of the saturation or determined experimentally. In addition, there is no unique relationship between capillary pressure and saturation because of capillary pressure hysteresis caused by dynamic effects.

2.4.5. Drainage and Imbibition

In an initially fluid saturated system the displacement of a wetting phase by a non-wetting phase is called primary drainage process. When the non-wetting phase is displaced by a wetting phase, the process is called imbibition. Figure 2.7 shows a typical capillary pressure-saturation curve for a water-oil system in a porous rock.

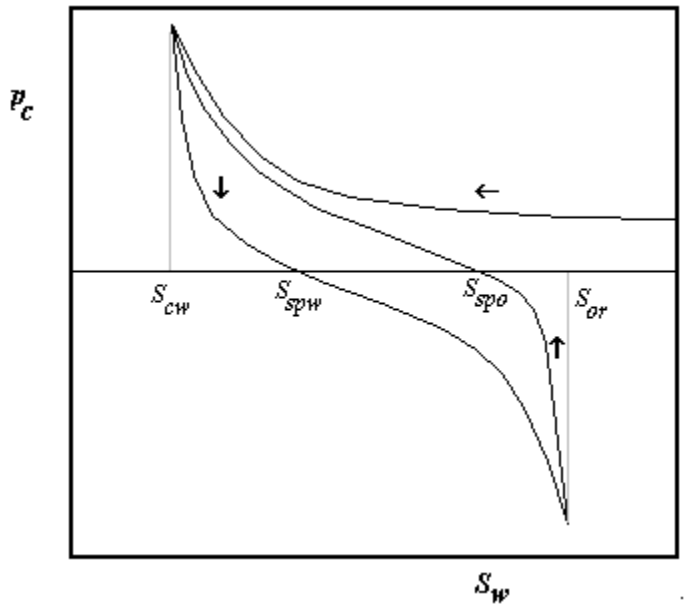

Figure 2.7: Capillary pressure-saturation curves for two-phase drainage and imbibition

At water saturation, S_w=1, the start of the drainage, an "entrance" pressure needs to be exceeded before oil can enter the sample. As pressure increases, drainage of the system continues until it reaches a point where further drainage is not possible. The amount of the wetting fluid (water) that remains in the system is called irreducible or connate saturation, S_{cw}. There will be no more flow of the wetting phase until this level of saturation is exceeded. By starting from this point and following the imbibition curve by decreasing the pressure and displacing the non-wetting phase by wetting phase, a point where a certain amount of the non-wetting phase remains in the system at zero capillary pressure is reached. This amount is called the residual saturation of the

non-wetting phase. The imbibition process can be started at any point on the drainage curve and the drainage process can be started at any point on the imbibition curve. The minimum amount of pressure required for the non-wetting phase to initiate the displacement of the wetting phase is called the threshold pressure (or bubbling pressure or non-wetting fluid entry value). This pressure is controlled by pore-throat size (the maximum radius). The non-wetting fluid saturation increases as the capillary pressure increases and at the end of drainage processes, most of the pore-throats and pore-bodies are filled with non-wetting fluid except a very thin film along the pore-walls occupied by the wetting phase at irreducible saturation (Roof, 1970; Lenormand et al., 1983; Mohanty et al., 1987; Zhao et al., 2010; Sorbie et, al., 2011; Fatemi and Sohrabi, 2013; Falode and Manuel, 2014).

Imbibition, displacement of non-wetting phase by wetting phase, process takes place via two mechanisms: choke-off (or snap-off) and retraction displacement. In choke-off, the non-wetting phase is displaced from small throats due to wetting phase film flow, and in retraction, a piston displacement from small pore-bodies takes place. Choke-off is controlled by the aspect ratio of the system (the ratio of pore-body size to pore-throat size), as this ratio increases choke-off becomes more dominant (Li and Wardlaw, 1986a, b).

In choke-off, the interface in a pore-throat breaks if:

$$P_c \leq \frac{\sigma \cos\theta}{r_t} \tag{2.9}$$

In retraction, the head meniscus within a pore-body leaves the pore-body and moves into the adjacent pore-throats. This event takes place if the capillary pressure satisfies:

$$P_c \leq \frac{2\sigma \cos\theta}{r_b z_{nw}} \tag{2.10}$$

where z_{nw} is the number of adjacent pore-throats filled with non-wetting phase (Lenormand et al., 1983; Mohanty et al., 1987; Jerauld and Salter, 1990).

From the above discussion it is obvious that processes such as drainage and imbibition and hence the distribution of fluid phases in porous media systems depend upon the geometry and the topology of the pore space (pore-body sizes, pore-throat sizes, aspect ratio and the interconnectivity of the pore space). Therefore, characterization and proper representation of the pore space is important to better understand such processes.

2.4.6 Fluid Displacement Energy

When a core is strongly water-wet the core will imbibe water until the water saturation equals the water saturation at the residual oil saturation. This means that the work required for oil displacement is almost zero for a strongly water-wet system. The amount and rate of imbibition depend on a number of simultaneously acting properties of a water-wet system: the wettability of the system, the interfacial tension, the saturation history of the system, the initial saturation, the fluid viscosities, the pore geometry, and the pore size distribution. As the system becomes less water-wet, the work required for displacement of oil increases and the amount and rate of imbibition decrease. This means that a smaller amount of water will imbibe at a lower rate as the system becomes less water-wet. If the system is oil-wet, oil will spontaneously imbibe into the system displacing the water. Water must be forced into the system and the work required for the displacement of oil by water is, in theory, the work required for a waterflood, an economic factor of oil production.

2.4.7 Permeability

The permeability of a porous medium describes the ability of a fluid to flow through the porous medium. This is often called the absolute permeability and is a quantity that depends on the geometry of the medium only. Permeability is the single-phase fluid conductivity of a porous material and its value is determined by the structure of the porous rock.

The equation that defines permeability in terms of measurable quantities is Darcy's law. If we consider an incompressible fluid, with viscosity μ, which is forced to flow, at flow rate q, through a porous medium, of length L and with cross section A, such that the pressure difference across the length of the porous medium is ΔP. Then the permeability K of the material is defined as:

$$K = \frac{q\mu L}{A\Delta P} \tag{2.11}$$

A tight rock, with small pore diameter will have in general a smaller permeability than a coarse rock with larger pores. From equation (2.11) it is seen that permeability, K has dimensions of length squared. The unit most widely employed for permeability is the Darcy (D); $1D = (1\ \mu\ m)^2 = 10^{-12}\ m^2$.

2.4.8 Relative Permeability

The concept of relative permeability, which also depends on the fluids flowing in the porous network, is introduced below. When two or more immiscible fluids are present in porous media systems, the pore space is partitioned among fluids that exist in the system. As a result, the cross-sectional area available for the flow of each fluid is less than the total cross sectional area of the pore space. This condition leads to the concept of relative permeability. The relative permeability

of a fluid at given saturation can then be defined as ratio of the intrinsic permeability of the fluid to the total intrinsic permeability of the porous media. In simple term, relative permeability describes the extent to which the flow of one fluid is hindered by the other. As with the pressure-saturation, the location and saturation of the phases is dependent on the morphology of the pore space (Bear, 1972). The relative permeability is defined by setting-up the Darcy equation individually for each phase *i* that flows in the pore space:

$$q_i = \left(\frac{K k_{ri}}{\mu_i} \right) A \frac{\Delta p_i}{\Delta x} \tag{2.12}$$

with q_i being the flow rate of phase *i*, k_{ri} the relative permeability of phase *i*, μ_i the viscosity of phase *i* and Δp_i the pressure drop within phase *i*. The term in brackets is denoted the "mobility" of phase *i*.

2.4.9 Determination of Porosity and Permeability using X-ray CT

Permeability, like other physical properties, depends on the complex microstructure of the porous medium. According to (Bear 1988), attempts to relate permeability to other easily computed parameters, such as porosity and specific surface area has not been successful. It is therefore necessary to study fluid flow behavior directly within the pore space to be able to accurately correlate and estimate the permeability of the rock medium. Using numerical techniques permeability can now be predicted with improved accuracy. Three-dimensional (3-D) images can be constructed from two-dimensional high-resolution images of rock samples (Zinszner and Meynot 1982; Thovert et al. 1993). Using object-based methods, where grains of different sizes and shapes are deposited (Øren et al. 1998), an image is obtained that reproduces the statistics of the two-dimensional pictures (Adler et al. 1990; Roberts 1997; Okabe and Blunt 2004). X-ray computed tomography is capable to generate 3-D images with a resolution of only a

few microns (Coenen et al. 2004; Flannery et al. 1987) sufficient enough to capture the pore space of many reservoir rocks.

X-ray computerized tomography (μ-CT scanning) has been used in the medical field to image the human body for more than two decades (Hounsfield, 1973; Ledley et al., 1974). Recently, it has been applied to earth sciences. Bonner et al. (1994) confirmed fluid migration in the rock by X-ray CT. Chen et al. (1996) used X-ray CT in the experimental study of the movement gas flow through sand in the presence water. Tivey and Singh (1997) used X-ray CT to study the internal structure of fragile sea-floor hydrothermal vent samples. Nakashima et al. (1997) applied X-ray CT to the three- dimensional non-destructive imaging of arrays of fluid inclusions in a mineral. Ohtani et al. (1997) and Ohtani et al. used X-ray CT to clarify the heterogeneous distribution of miarolitic cavities in granite. Grader et al (2009) used X-ray CT to determine the porosity and permeability for a carbonate reservoir sample using the lattice Boltzmann method for fluid dynamic calculations.

The X-ray process includes sample preparation, imaging, image processing, property computations, and property integration to the core scale. The material sample (reservoir core plug) is subjected to a descending scale of x-ray CT imaging, along with physical sub-sampling of the core. The descending size of scanning leads to increased resolution of the three-dimensional digital core, keeping the sample volumes registered in place. The resulting digital rocks are segmented and the pore structure is determined on the x-ray CT grid system. The resulting three-dimensional pore structure, that is the same as the actual pore structure subjected to resolution limits, is used as the input grid system for direct fluid dynamic computations that

are second order accurate representation of the Navier-Stokes fluid flow equations. These computations yield porosity, absolute permeability, relative permeabilities, and capillary pressure (Grader et al.). The resulting computations were in good agreement with the laboratory measurements.

2.4.10 Lattice-Boltzmann Method (LBM)

Network models idealize the porous rock system as a lattice of pores and throats through which fluid displacement and transport can be computed semi-analytically (Blunt 2001). However, it is not easy to separate between pores and throats and this creates difficulties in using network extraction algorithms (Dong and Blunt 2009). Again, it is difficult to capture some complex pore geometries with network models. It is natural, therefore, to study transport properties directly on micro-CT images. The lattice Boltzmann method is a popular and simplified approach for modeling flow in complex geometries (Jin et al. 2004; Kang et al. 2006; Knackstedt et al. 2004; Pan et al. 2001; Pan et al. 2004) because coding is straightforward and it can be readily parallelized (Piller et al. 2009; Liu et al., 2015).

The lattice-Boltzmann method for single-phase flow describes fluid flow as collisions of mass particles in a lattice (Chen et al., 1992). In two-phase flow, almost the same procedures are followed as in the single-phase case, except that there are two different types of particles representing two immiscible fluids, and calculation of surface tension and wettability are needed. Although the lattice Boltzmann is a powerful approach that is widely used, it is computationally demanding and requires the use of massively parallel computing approaches. Moreover, applying no-slip (zero velocity on the solid surfaces) and constant - pressure boundary conditions is not

straightforward (d'Humières and Ginzburg 2009; Noble et al.1995; van Genabeek and Rothman 1996).

Manwart et al. (2002) compared the finite difference and lattice Boltzmann methods to calculate the permeability of three- dimensional porous media. They showed that in terms of memory, the lattice Boltzmann method required 2.5 times more memory than what was required by finite difference, while the computation times and numerical results of the two methods were similar. The LB method is used in this work to compute the porosity and permeability of the Agbada sandstone and the result obtained is compared with experimental values.

There are several popular lattice Boltzmann (LB) techniques for the analysis of multiphase flows, three of which are the methods of Gunstensen et al. (1991), the Bhatnagar–Gross–Krook (BGK) model (Chen et al. 1992), Shan and Chen (1993), and free energy approach by Swift et al. (1996). All three methods have been employed in numerical researches and each one has its distinct advantages. A review of these methods can be found in Nourgaliev et al. (2003). Among all of these LBM models, Shan & Chen's model (SC model) is widely used due to its simplicity and remarkable versatility. It can handle fluid phases with different densities, viscosities and wettabilities.

The most widely used LB model is the BGK model (Chen et al. 1992), with a standard bounce-back (SBB) scheme for fluid–solid boundaries. A major setback of the BGK method is that the collision operator is approximated by a single-relaxation-time (SRT) approximation, which has some defects such as numerical instability and viscosity dependence of boundary locations, especially in under-relaxed situations (Qian et al. 1992). This boundary conditions dependence

on viscosity creates a serious problem in the simulation of flow through porous media because the intrinsic permeability becomes viscosity dependent, instead of being a function of the characteristic physical properties of the porous medium alone. The inherent deficiencies in the BGK model can be significantly reduced by using a multiple-relaxation-time (MRT) approach (He et al. 1997), which separates the relaxation times for different kinetic modes and allows tuning to improve numerical stability and accuracy. In this study D2Q9 MRT is used (Lallemand and Lue, 2000, Li et al., 2005; Chen et al., 2013; Cercigani, 2013; Shi et al., 2014).

2.5 Pore Networks, Geometry and Wetting Films

2.5.1 Pore-network shapes

The shapes assigned to pores and throats are significant in defining transport properties.

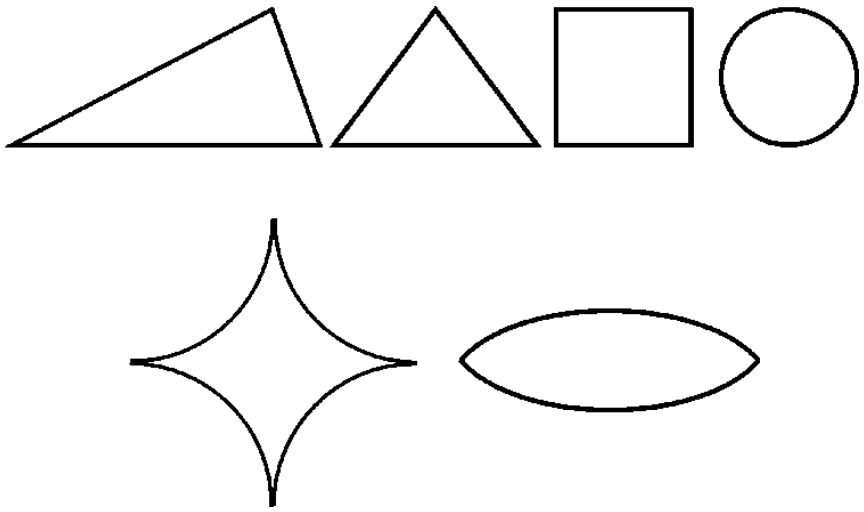

Figure 2.8: Elements with different cross-sectional shapes.

In cross section, individual pores and throats are often modeled as triangles and high-order polygons (Man and Jing, 1999, 2000, 2001). This allows wetting phase to occupy the corners when the non-wetting phase fills the center. As well as triangular cross section elements, authors have used geometries with circular (Dullien et al., 1989), square (Blunt, 1997, 1998), star-shape

(Fenwick and Blunt, 1998; Dillard and Blunt, 2000), and lenticular (Lenormand et al., 1983) cross sections (see Figure 2.8) to represent pores and throats.

Most early works on pore-scale modeling assumed that the throats were cylinders with a circular cross-section. Pores were either not modeled explicitly at all or were spherical or cylindrical in shape. It is reasonable to assume an effective circular cross-section for predicting single-phase properties, or the relative permeability of the non-wetting phase that resides in the centers of the larger pore spaces. For example, for the sphere packs studied by Bryant et al. (1992, 1993), the true cross-section of the throats was a grain boundary shape formed by the intersection of three or four spheres. They defined an effective radius that was the arithmetic mean of the inscribed radius and a radius of a circle with the same cross-sectional area as the throat. This effective radius varied along the throat. To account for this in the computation of permeability, they found the hydraulic conductance of each throat from an analytical calculation of the flow through a series of truncated cones. For multiphase flow, the capillary entry pressure for the non-wetting phase depended on the minimum effective radius along the throat. For saturation calculations, the volume of the throat was computed directly from the pore structure. No explicit computation for pores was made. Therefore, conceptually, the network was composed of throats of circular cross-section connected at pores with no volume. However, the volumes, hydraulic conductance and capillary entry pressures of the throats were carefully calculated based on the description of the real pore space. The Heriot-Watt group by the same approach, known as the three 'R's' considered a lattice of cylindrical throats with no volume assigned to pores (Dixit et al., 1998, 1999, 2000). However they used independent expressions for the capillary pressure, the volume of a throat and the hydraulic conductance. This is equivalent to using different values for the

radius R in the expressions for capillary pressure, volume and conductance. There are three different ‘sizes’ that are important: an inscribed radius to determine the capillary pressure at which a non-wetting fluid will enter the element; a radius that controls the volume; and a hydraulic radius that controls fluid conductance. These quantities are not necessarily simply related when representing porous media.

2.5.2 Wetting Films

In multiphase flow, when the non-wetting phase occupies the center of a pore or throat, the wetting phase may reside in grooves, crevices of roughness in the pore space. These wetting layers have been observed directly in micromodel experiments (Lenormand et al., 1983). Wetting layers are stabilized by capillary forces and have a typical thickness of a few microns--comparable to, although smaller than-the size of the pores. Flow through these layers, although slow, is measurable and can have a significant effect on the displacement process. This is in contrast to wetting film that are stabilized by molecular forces and are typically nanometers thick. Flow through such films is negligible. In a sphere pack with smooth grains, the wetting phase can form pendular rings of fluid around the grain contacts. The wetting phase may apparently reside in layers, but the pendular rings are not connected and the wetting phase can be trapped. This was observed in bead packs by Dullien et al. (1989) where a trapped wetting phase saturation of approximately 10% was found. When a sandpack, fully water-saturated, was drained in air, water (wetting) phase saturations as low as 1% were reached. This implies that in porous media composed of rough wet grains the wetting layers are connected and provide a conduit for flow, albeit slow, down to low saturation. The consideration of wetting layers in pore-scale modeling studies is essential to reproduce even the qualitative behavior of electrical

properties, three-phase flow, relative permeability hysteresis, dissolution rate and unsaturated flow in fractures (Øren et al., 1998; Dillaed and Blunt, 2000; Tsakiroglou, 2000; Tsakiroglou and Payatakes, 2000; Fenwick and Blunt, 1998; Hughes and Blunt, 2001; Wang and Mohanty, 2000; Or and Tuller, 2000). In these cases, having pores with only single-phase occupancy, or disconnected wetting phase, allowed insufficient connectivity of the wetting phase and resulted in poor comparisons with experiment. At very low wetting phase saturation, adsorbed water films, nanometers in thickness, in addition to wetting layers, have a significant impact on capillary pressure (Tuller et al., 1999; Or and Tuller, 1999).

It is difficult to represent every nook and cranny in the pore space directly. A simpler approach, adopted by many authors, is to assign some simple shape to the pore and throat cross-sections that accommodate wetting layers. Just as in the assignment of effective pore sizes, there is no suggestion that the real pore space is represented by some idealized constant cross-section—the shape is chosen simply to place the correct volume of wetting phase in layers in a pore whose center is filled by non-wetting phase and to give the right hydraulic conductivity to the layer. Varieties of different shapes have been proposed, including fractal models of roughness (Coehlo et al., 1997; Ioannidis and Chatzis, 2000), grain boundary pore shapes (Thompson and Fogler, 1997; Coehlo et al., 1997; Biswal et al., 1999) squares Mani and Mohanty 1998; Man and Jing 1999, 2000, 2001) and triangles (Hui and Blunt; Øren et al., 1998). Øren et al. (1998) defined a shape factor, G, for each pore and throat. The shape factor is the ratio of the cross-sectional area to the perimeter length squared. They then modeled the element as having a circular, square or scalene triangular cross-section such that the shape of the cross-section had the same shape factor

as the reconstructed pore space they were modeling. In most cases the pores and throats had a triangular cross-section, as shown in Figure 2.9.

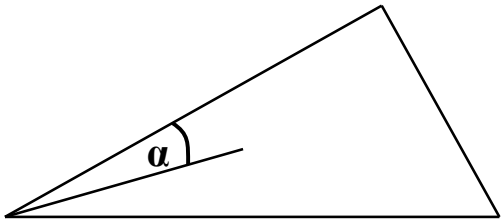

Figure 2.9: Triangular cross-section of a pore space

The details of how this was done are explained in Øren et al. (1998) and Patzek (2001). When non-wetting phase occupies the pore centers, wetting phase can reside in the corners. The volume of wetting phase in the corners depends on the capillary pressure. It is further assumed that all the wetting layers are connected to those in adjacent pores and throats. For multiphase flow consideration of wetting layers is essential to model correctly the behavior of the wetting phase.

2.6 The Effect of Wettability on Oil Recovery

2.6.1 Interacting parameters

Oil recovery efficiency depends, not only on the geometry, size and distribution of the pore spaces but also on the interaction of many other microscopic and macroscopic parameters at the pore scale level. Among these parameters are the wetting state of the reservoir rock, salinity of the connate water and the displacing fluid, fluid displacement mechanisms, rock mineralogy, and other reservoir rock and fluid properties. These interacting parameters when properly understood and applied, lead to efficient and cost-effective oil recovery. A lot of study of these parameters has been and is still being carried out by researches and engineers in the oil industry.

The reservoir-wetting state has been shown to be one of the most important parameters that affect the pore-scale displacement mechanism. Understanding reservoir wettability is fundamental to understanding multiphase flow problems, ranging from oil migration from source rocks through primary production mechanisms to EOR processes. The importance of wettability in the recovery of oil has been widely demonstrated by many researchers (Buckley and Leverett, 1942; Rathmell et al., 1973; Morrow et al., 1973; Jerauld et al., 1994; Dandekar et al., 2008).

2.6.2 Wettability Concepts

Wettability is the term used to describe the relative adhesion of two fluids to a solid surface (Tiab et al., 1996). In a porous medium containing two or more immiscible fluids, wettability is a measure of the preferential tendency of one of the fluids to adhere to the surface. According to Morrow (1990), reservoir wettability has a dependence on the complex interface boundary conditions acting within the pore space of sedimentary rocks. These conditions have a dominant effect on interface movement and associated oil displacement. Wettability plays a significant role in multiphase flow problems ranging from oil migration from source rocks to enhanced oil recovery methods such as alternate injection of CO_2 and water. Reservoir wettability is not a simply defined property and classification of reservoirs as just water-wet or oil-wet is over simplified. In a water-wet brine-oil-rock system, water will occupy the smaller pores and wet the majority of the surfaces in the larger pores. In areas of high oil saturation, the oil rests on a film of water spread over the rock surface. If the rock surface is preferentially water-wet and the rock is saturated with oil, water will naturally imbibe into the smaller pores, displacing oil from the core.

However, if the rock surface is preferentially oil-wet and the core is saturated with water, it will naturally imbibe oil into the smaller pores, displacing water from the core. Thus, a core saturated with oil is water-wet if it imbibes water spontaneously and, conversely, a core saturated with water is oil-wet if it imbibes oil spontaneously. The wettability of a reservoir can range from strongly water-wet to strongly oil-wet depending on the brine-oil-interactions with the rock surface.

Kovscek et al. (1993) observed that wettability is a prime factor controlling multiphase flow and phase trapping since wetting fluids occupy the smallest, tiniest and most hydrodynamically resistive pore channel. Homogenous wettability of porous media is broadly described by the following terms:

1. Neutral or intermediate wettability – this occurs when the rock displays no preference for either oil or water; the system can be equally wetted by both oil and water.

2. Fractional wettability – implies a spotted, heterogeneous wetting of the surface. Fractional wettability means that scattered areas throughout the rock have different degrees of wettability (either water-wet or oil-wet). Fractional wettability occurs when the surfaces of the rock are composed of various minerals that have very different surface chemical properties, leading to variations in wettability throughout the internal surface of the rock. Fractional wettability should not be confused with a state of neutral wettability, meaning that the rock surfaces have an equal affinity to oil and water. Cores exhibiting fractional wettability will imbibe a small quantity of water when the oil saturation is high, and also will imbibe a small amount of oil when the water saturation is high.

3. Mixed wettability – this term is commonly used to refer to the condition where the smaller pores are occupied by water and are water-wet, whereas the larger pores of the rock are oil-wet, and a continuous filament of oil exists throughout the core in the larger pores. Because the oil is located in the larger pores of the system in a continuous path, oil displacement from the rock occurs even at very low oil saturation. That is why the residual oil saturation of mixed-wettability rocks is unusually low. Mixed wettability can occur as a result of the invasion of oil containing interfacially active polar organic compounds into a water-wet rock saturated with brine. After having displaced the brine from the larger pores, the interfacially active compounds react with the rock's surface, displacing the remaining aqueous film and producing an oil-wet lining on the surface within the larger pores. The water film between the rock and the oil in the pore is stabilized by a double layer of electrostatic forces. As the thickness of the film is diminished by the invading oil, the electrostatic force balance is destroyed and the film ruptures, allowing the polar organic compounds in the oil to react directly with the rock surface (Tiab et al., 1996).

2.6.3 Reservoir Wettability and Oil Recovery Efficiency

The fact that wettability affects oil recovery efficiency is widely acknowledged. One of the seminal works on the importance of wettability on waterflooding performance was by Buckley and Leverett1 in 1941. However, the wetting phase that will result in optimal recovery of oil appears to be the subject of intense research debate. Reported observed cases of optimal oil recovery for water-wet, intermediate-wet/neutral-wet and oil-wet conditions have been published Blunt (1997); DiCarlo et al., (2000); Dandekar, et al, (2008); Zhao et al., (2010). The reason for

this divergence in reports is attributable to a number of modifying factors, which include, among other reasons, the following:

1. constraint of difficulty in wetting state reproducibility;
2. lack of a unified standard procedure for coring, core handing, and core storage;
3. different methods adopted for wetting-state characterization and their inherent limitations; and
4. the fact that a host of other reservoir rock and fluid properties, in addition to the reservoir wetting condition, also act to influence oil recovery efficiency.

2.6.4 Wettability Alteration in Cores

Departure from strongly water-wet conditions has been reported to result in either a decrease or an increase in oil recovery efficiency, reflecting the range of possible wettability changes. The difficulty in measuring the in situ reservoir-wetting state necessitates the "surface" determination of reservoir wettability through the use of core plugs or whole length cores. However, the wetting state of the core samples may be altered from their in situ values during cutting, surfacing, and handling of the core samples. Variation of core wettability from in situ reservoir wettability is due to a number of reasons including the following:

1. Temperature and pressure drop as the core sample is brought to the surface which results in the flashing of the connate water present
2. Drying of the core
3. Invasion of drilling mud during coring
4. Compositional changes resulting in asphaltene deposition or wax precipitation from the crude oil because of reduction in temperature and pressure

5. Oxidation, contamination, and desiccation during handling/storage. The oxidation process may sometimes enhance deposition.

Care must be taken in the handling of the core samples to ensure that the actual wettability is not altered. Usually the wetting state of the core plug may be altered in one of the stages beginning with coring, core handling, core preservation, and wettability measurement in the laboratory. Where the core wetting state has been altered, care should be taken to duplicate/reproduce the reservoir wetting conditions as closely as possible. However, some published reports (Morrow, 1990; Buckley et al., 1996; Buckley and Lui, 1998; Zhao, 2000; Ma et al., 2013; Dandekar, 2013; Li et al., 2015) in this regard have suggested ways of preserving and restoring in situ core wetting state so as to ensure that reservoir rock wettability is accurately measured. In addition, these methods help to ensure that core samples used in the laboratory for determination of oil recovery efficiency and related studies are representative.

The wetting characteristics of a reservoir is an important factor in determining residual oil saturation after a given production process. An oil-wet formation tends to hold back more oil in its minute pores and produce reservoir water. The alteration of reservoir wettability from oil-wet to water-wet or mixed wet may help in the production of more oil from such a reservoir.

2.6.5 Pore Level Studies of Wettability Effects on Oil Recovery

Pore network modeling is a useful tool for studying the effect of porous medium structure and wettability on multiphase flow. Network modeling simulates displacement processes in a porous medium through a lattice of pores linked by throats and relates predictions of microscopic fluid

distribution to macroscopic parameters, such as wettability index and oil recovery (Blunt and King, 1991; Blunt, 1998; Øren et al., 1998; Dixit et al., 1999, 2000; Al-Futaisi and Patzek, 2003; Øren and Bakke, 2003; Zhao et al., 2010; Al-dhahli et al, 2011; Clemens et al., 2013; Piller et al, 2014).

Primary oil recovery is affected by the wettability of the system because a water-wet system will exhibit greater primary oil recovery, but the relationship between primary recovery and wettability has not been developed (Tiab et al., 1996). Most of the studies on the effects of wettability on oil recovery have been focused on waterflooding and the analyses of the behavior of relative permeability curves. In laboratory displacement tests designed to investigate the effects of wettability on oil recovery, early results showed a decrease of the oil recovery with decreasing water-wetness of the cores (Morrow, 1990). This proves the earlier assumption that increased oil recovery is as direct function of the degree of wetting preference of the rock for water and associated strong capillary imbibition forces. However, there are an increasing number of examples of improved recovery with a shift from strongly water-wet conditions being reported for weakly water-wet to intermediate wetting conditions (these results generally involve displacement of crude oils or refined oils from cores in which organic films have been deposited from crude oil). When the wettability is varied from water-wet to oil-wet, the recovery is seen to pass through a maximum when the wettability is close to neutral.

Many researchers have carried out experimental studies on the effect of wettability on fluid flow properties such as capillary pressure, relative permeability, residual saturations and waterflood oil recovery (Anderson, 1987a,b; Morrow, 1990; Jadhunandan, 1990; Caubit and Bertin, 2004;

Al-Raoush, 2009; Raeesi and Piri, 2009; O'Carroll et al. 2010; Parsaei and Chatzis, 2011; Zendehboudi et al. 2011; Fatemi and Sohrabi, 2013; Ghoodjani and Bolouri, 2014).

Morrow (1990) conducted laboratory displacement experiments to investigate the effect of wettability on residual oil saturation and showed that residual oil saturation is least for systems at neutral wettability and increases as the system becomes more water-wet or oil-wet. A strongly water-wet system will produce most of the oil before water breakthrough and the water/oil ratio will increase rapidly thereafter, thus diminishing production to an insignificant amount. An oil-wet system will produce water early at a low water/oil ratio, which will continue to increase gradually.

Morrow (1990) also showed oil recovery decreased as water-wetness of the cores decreased. This is consistent with the intuitive notion that strong wetting preference of the rock for water and associated strong capillary imbibition forces give the most efficient oil displacement. However, there is an increasing number of examples of improved recovery with a shift from strongly water-wet conditions being reported for weakly water-wet to intermediate wetting conditions. These results generally involve displacement of crude oils or refined oils from cores in which organic films have been deposited from crude oil. When the wettability is varied from water-wet to oil-wet, the recovery is seen to pass through a maximum when the wettability is close to neutral.

Skauge et al. (1994) carried out study to show oil recovery dependence on water saturation, and the role of immobile phase on three-phase flow behavior. They found that, for sandstone cores

under water wet conditions, oil recovery increased in the presence of connate water compared to when water is not present. The influence of water-oil capillary pressure was found to change (reduce) the drainage rate, and also reduced oil relative permeability.

Jadhunandan and Morrow (1995) using different Berea sandstone cores studied oil recovery by waterflood as a function of wettability. By varying initial water saturation, aging conditions and wetting states to represent different reservoir conditions, they showed that waterflood oil recovery was highest at weakly water-wet conditions. Oil recovery decreased as the system changed from strongly water-wet to oil-wet.

Vizika and Lombard (1995) presented a gravity drainage study, performed with unconsolidated cores of pre-established wettability. Using different fluids with different spreading coefficients in their experiments, they clearly showed the impact of wettability on oil recovery. The highest oil recovery was obtained with water wet or fractional wet cores when spreading coefficient is positive.

McDougall and Sorbie (1995; 1997) developed a network model to investigate trends in relative permeability and oil recovery as a function of wettability using network of regular cubic lattice. Without explicitly including the wetting layers they were able to predict hitherto puzzling trends in oil recovery. They showed that oil recovery would be maximum where about half the pore space is water-wet and other half oil-wet. This agrees with experimental measurements of Jadhunandan and Morrow (1995). Dixit et al (1999) developed a three-dimensional network model to derive capillary pressure and relative permeability curves incorporating the effects of variations in wettability and realistic variations in advancing and receding contact angles. By randomly

varying contact angles in the network they simulated different wettability states and found that oil recovery by water imbibition in weakly water-wet system increases as the contact angle approaches neutral value (90^0). Deriving from theoretical calculations, they proposed a regime based theory of wettability classification and analysis and used it to classify a range of experimentally observed waterflood recovery trends as a function of wettability and contact angles distribution.

Ma et al., (1999) used Alaskan'93 crude oil to study the relationship between recovery by spontaneous imbibition and aging time. They obtained results that indicate increase in microscopic displacement efficiency as the system becomes less water-wet, leading to increased oil recovery. They stated that microscopic displacement efficiency for both spontaneous imbibition and waterflooding is governed by complex capillary phenomena related to stability of capillary structures and motion of three phase (oil/brine/solid) lines of contact. Oil recovery by spontaneous imbibition depends on the combined effect of wettability on microscopic displacement efficiency and capillary pressure. As the system becomes less water-wet trapping of oil by snap-off becomes less, leading to increase in recovery efficiency. In previous studies by Morrow et al., (1986); Jadhunandan and Morrow (1995), and Villard et al.(28) similar results were obtained for different crude oils. Maximum waterflood recoveries were obtained at close to very neutral or weakly water-wet conditions.

Studying depressurization process in a reservoir depleted to residual oil saturation, Grattoni and Dawe (2003) performed quantitative experiments to confirm earlier results from visual experiments in glass micromodels which suggested that wettability and oil spreading coefficient

substantially influence both the value of the critical gas saturation and the growth pattern for the developing gas bubbles, and thus the gas flow. They used large sintered packs, with different matrix wettability and oils of different spreading coefficients. The results showed that the magnitude of the critical gas saturation for a water-wet system is about the same irrespective of whether the oil is spreading or non-spreading, but it is much higher than for the oil-wet case. In addition, oil is also produced but the rate of production is dependent upon the rock wettability and the oil characteristics. They found that in a water-wet medium, for spreading oils, the physical form of the oil becomes transformed from being immobile ganglia into mobile oil films, which can then be transported by the gas. They showed that for non-spreading oils, oil has to be pushed out by the gas as discontinuous ganglia so less is oil produced while in an oil-wet system, the oil phase already exists as a continuous film on the surface of the solid so that the generation of gas effectively expands the oil phase, enabling the oil to be produced in larger quantities even at lower gas saturations. Their study gave further evidence that rock wettability has an important influence on waterflood oil recovery and on the performance of gas liberation from residual oil.

Al-Futaisi and Patzek (2003) used a network extracted from a 3D micro-focused X-ray CT image of a sample of Bentheimer sandstone to study the impact of alteration on two-phase quasi-static flow characteristics of a porous medium. They showed that in a less water-wet state, residual oil saturation initially decreased but as the system changed from water-wet to oil-wet conditions the residual oil saturation increased sharply and then decreased to a minimum in oil-wet condition.

Jackson et al. (2003) used a 3-D pore-scale network representation of Berea sandstone to investigate relative permeability and capillary pressure hysteresis. They successfully predicted

experimental relative permeability data for water-wet Berea sandstone as well as waterflood recoveries as a function of wettability. Based on their findings they suggested the use of network models that incorporate the structure of real rocks and the pertinent pore-scale displacement processes in predicting wettability impact on oil recovery.

Qingjie et al. (2004) conducted a series of experiments to investigate the effect of wettability alteration on relative permeability for oil-wet reservoir sandstones rock. By varying the air permeability and brine concentration they showed that both water and oil relative permeability curves are dependent strongly on wettability alteration. Water relative permeability curves were lower as wettability changed from oil-wet to intermediate wet with improvement in oil recovery efficiency.

Caubit et al (2004) investigated the effect of wettability on residual saturations during gravity drainage and tertiary flooding. Using cores of different lengths they performed experiments on forced displacement of gas by water and oil on the short cores, and gas/oil drainage by gravity in the presence of irreducible water (S_{wi}) followed by tertiary waterflooding on the long cores. Two-phase flow is obtained at the bottom of the core while three-phase flow is observed at the upper part of the core. Measured saturation profiles showed that saturation at the end of gravity drainage depends on wettability, while no wettability effect on three-phase residual gas saturation was observed.

Karabakal and Bagci (2004) discussed the effect of wettability on fluid distribution, and fluid flow in porous media, and investigated the influence of rock wettability on the relative

permeability and recovery of oil by waterflooding using core samples that had different wettability levels. In a water-wet medium, water breakthrough occurred relatively late and a considerable amount of oil was produced before the breakthrough. After the breakthrough, the rate of oil production decreased very sharply. Decreasing the water wetness resulted in decreasing the breakthrough recovery. In the intermediately wet system, breakthrough occurred very early and most of the oil was produced after the breakthrough. Water breakthrough had almost no effect on the rate of oil production.

Rostami et al (2008) carried out an experimental study of wettability effects on oil recovery and residual saturations during gas assisted gravity drainage and subsequent water flooding mechanisms. Forced downward displacement of oil by gas was performed on long artificial consolidated porous media and sensitivity analyses were done for wettability and gas injection rate. The wettability characteristics of porous media were modified by chemical treatment of glass beads. To investigate the impact of wettability during three phase flow, gas/oil gravity drainage mechanism was followed by subsequent water displacement. Analysis and interpretation of the results obtained in terms of saturation profile, oil recovery at break through time, final oil recovery and residual saturations shows that fluid injection rate and wettability played a major role on phase distribution and fluid displacement mechanism. ized front velocity, while in oil-wet media, oil remains continuous through wetting film. Three phase residual oil saturation profile strongly depends on spreading and wettability.

Extending their previous work on relative permeability hysteresis during water-alternating-gas (WAG) injection cycles Suicmez et al. (2008) used a three-dimensional mixed-wet random

network model representing Berea sandstone to investigate the effects of wettability and pore-level displacement on hydrocarbon trapping. They studied four different wettability conditions: water-wet, weakly water-wet, weakly oil-wet and oil-wet and demonstrated that the amounts of oil and gas that are trapped showed surprising trends with wettability that cannot be captured using previously developed empirical trapping models. The amount of oil that is trapped by water in the presence of gas increases as the medium becomes more oil-wet, as opposed to the trend observed in two-phase flow.

Al-Raoush (2009) investigated the impact of wettability of porous media on pore-scale characteristics of residual non-aqueous phase liquids (NAPLs). Using image processing algorithms on high-resolution 3-D images of fractionally wet porous media systems with mean grain size of 250 μm obtained through a Synchrotron X-ray micro-tomography he computed pore-scale characteristics of NAPL blobs such as volume, lengths, interfacial areas, and sphericity index. Findings indicate that spatial variation in wettability of porous media surfaces has a significant impact on pore-scale characteristics of residual NAPL blobs in saturated porous media systems. He concluded that at increasing wet-wet condition of the surfaces, residual NAPL blobs increase in size and length due to the entrapment at large pore bodies. NAPL−water interfacial areas tend to increase as the NAPL-wet surface fractions increase. Overall residual NAPL saturations are less in fractionally wet systems and increase as the systems become more NAPL-wet or water-wet.

Raeesi and Piri (2009) used a model 3-D network of interconnected pores and throats of various geometrical shapes, representing the pore space of Berea and Saudi Arabia reservoir sandstone,

to investigate the impact of wettability and phase trapping on the relationship between interfacial area, capillary pressure and saturation in two-phase drainage and imbibition processes. The model allowed multiple phases to be present in each capillary element in wetting and spreading layers, as well as occupying the center of the pore space. They allowed the wettability of the rock surfaces contacted by oil to alter after primary drainage. They modeled primary oil drainage and water flooding for mixed-wet conditions, and secondary oil injection for a water-wet system and investigated hysteresis by performing water injection into systems of varying wettability and initial water saturation. They showed that trapping and contact angle hystereses significantly affect the interfacial area. In a strongly water-wet system, a sharp increase is observed at the beginning of water flood, which shifts the area to a higher level than primary drainage. As the wettability of the system changes from strongly water-wet to strongly oil-wet, the trapped oil saturation decreases significantly. Starting water flood from intermediate water saturations, greater than the irreducible water saturation, can also affect the non-wetting phase entrapment, resulting in different interfacial area behaviors. Their results show encouraging agreement with the experimental data available in literature for glass beads, with some expected differences. Also, their results agree well with those generated by previously developed models.

Oil recovery pattern during gravity drainage processes in heterogeneous porous media depends strongly on wettability. Zendehboudi et al. (2011) investigated the effects of wettability in fractured and homogeneous porous media during free-fall gravity drainage (FFGD) and controlled gravity drainage (CGD) conditions. Using different test fluids (water and Varsol oil) at different wettabilities they captured important characteristics of gravity drainage processes such as the production performance, matrix–fracture flow communication, and liquid production

rate by the film-flow mechanism. They concluded that different wettability conditions govern the oil recovery mechanism during FFGD and CGD processes. They also showed that the wetting properties of the test fluid considerably affected the matrix-to-fracture transfer and the fluid saturation, with the water-wet conditions favoring oil recovery for both FFGD and CGD processes. Parsaei and Chatzis (2011) through a systematic experimental study investigated the impact of reservoir wettability variations at the macroscopic scale on oil recovery efficiency in gravity-assisted inert gas injection (GAIGI) process for tertiary recovery of residual oil by waterflooding. Obtained experimental results showed that for a positive oil-spreading coefficient, the continuity of water-wet portions of the heterogeneous porous medium favors tertiary oil recovery through the film flow mechanism. In addition, owing to the high waterflood residual oil content of the heterogeneous media tested, the oil bank formation occurred much earlier and grew faster, resulting in a higher oil recovery factor. However, having favorable wettability conditions in homogeneous porous media resulted in slightly lower reduced residual oil saturation after the GAIGI process compared to that in the heterogeneous media with the same withdrawal rate. A relationship between the oil recovery factor at gas breakthrough and gravity number was developed for the heterogeneous and homogeneous media. The recovery factor at gas breakthrough versus gravity number in homogeneous media follows a similar trend as that of homogeneous water-wet porous media. However, at a given gravity number, the recovery factor of heterogeneous media was greater than that of the homogeneous media.

Zhao et al. (2011) investigated the impacts of wettability on waterflood oil recovery using a capillary pore-scale network model derived from micro-CT images of different rock types. They reproduced the experimental results obtained by Jadhunandan and Morrow and validated the

pore-scale model used to simulate flooding cycles. They then used four network models, each representing a different rock system to systematically study the effects of wettability, initial water saturation, contact angle distribution and oil-wet fraction on waterflood oil recovery in different rock systems. From the results of their investigation they concluded that for a uniformly-wet system, oil recovery increases as the system becomes less water-wet and reaches a maximum for oil-wet conditions where recovery is approximately constant for contact angles greater than 100^0. In water-wet systems oil recovery decreases as initial water saturation increases whereas in oil-wet systems oil recovery initially increases and then decreases. Zhao and co-workers also concluded that for mixed-wet systems the oil-wet fraction plays a more important role in determining recovery than the contact angle in the oil-wet regions. Optimal recovery occurs when a small fraction of the system is water-wet. Pore structure influences only the initial saturation for optimal oil recovery and the magnitude of the recovery.

Spontaneous water imbibition into the matrix blocks is known as the main mechanism for increased oil recovery from naturally fractured oil reservoirs. The rate of oil recovery and its ultimate value is mostly affected by wettability of the rocks and their pore structure. Rezaveisi et al (2012) utilized a novel experimental model to study the imbibition mechanism under different wettability conditions in naturally fractured formations. Matrix blocks made from different grain types and size distributions of glass beads were saturated with two different types of synthetic oil, to mimic the oil-saturated matrixes. They used a standard chemical treatment process to alter the wetting characteristic of the models used in their study. Wettability, grain type and size distribution, as well as oleic phase properties, were changed to find the effect of these parameters on oil recovery efficiency. The results obtained show that presence of a small fraction of oil-wet

grains drastically affects oil recovery by capillary imbibition. They obtained a criterion to describe the effects of wetting property of the matrix blocks on oil recovery efficiency by capillary imbibition.

2.6.6 Wettability and Oil Recovery by Gas Injection

The efficiency in recovering a large fraction of the waterflood residual oil from water-wet porous media by low pressure inert gas injection assisted by gravity drainage was reported by Naylor and Frørup (1989). They conducted a series of experiments to investigate secondary and tertiary, gravity-stable, immiscible, nitrogen displacement of oil. Two high pressure and four low pressure experiments were performed using cores that consisted of well-cemented aeolian sandstone, which was water-wet, had well sorted grains and a low clay content. The high pressure runs were conducted to investigate the effects of core orientation during gas injection. Secondary injection was conducted in the presence of connate water saturation, and tertiary injection was conducted following a waterflood. The results from the study demonstrated that oil production can be enhanced when gravity forces assist the drainage of oil during gas displacement, and, furthermore, that a decrease in initial water saturation resulted in an increase of oil permeability during gas injection.

Catalan et al. (1994) reported experimental results obtained with oil-wet consolidated media. It was their goal to study the impact of wettability variation on oil recovery during tertiary gravity drainage in core samples. They conducted experiments with water-wet and oil-wet Berea, oil-wet Pembina Cardium cores, and glass bead packs. The Berea core was made oil-wet by treatment with a 4% solution of dichlorodimethylsilane (drifilm) in hexane. They found that the

displacement mechanisms of oil during tertiary gravity drainage are different in water-wet and oil-wet porous media. In water-wet media, the spreading of oil as a film between the gas occupying the center part of the pores and the aqueous phase covering the pore walls is essential to establish and maintain continuity of the oleic phase. By contrast, when the oil is the wetting phase, spreading is not important because the waterflood residual oil phase is always present as a continuous film on the pore walls.

Flow visualization experiments using macroscopically homogeneous glass micromodels helped show the role played by pore-level heterogeneities. In a random network of pore bodies connected by large pore throats imbedded in a network of smaller pore throats and pore bodies, it was observed that several segments of bypassed oil (waterflood residual oil) were successfully drained during gravity drainage. With the gas oil contact maintained constant, further drainage of oil, further reconnection of isolated residual oil, and further redistribution of residual oil took place, but, in all, residual oil recovery by gravity drainage from bypassed regions was found to be a very slow process.

Ren et al. (2004) conducted a pore-level observational study of gas-assisted tertiary gas injection processes to achieve a better understanding of the pore-level mechanisms. They used a transparent 3-D sandpack model and conducted updip waterflooding and tertiary gas injection to observe how the fluids flowed and to observe how the mobilization of the residual oil in a single pore took place after gas invasion or water invasion occurred. Of greatest interest to them was to see whether oil films and oil film flow occurred and to understand the mechanism underlying fluid flow in a single pore space. Some of their observations were that after the waterflood, the

residual oil was distributed sparsely as isolated oil droplets and that there was very little bypassed oil owing to the relatively low degree of heterogeneity of the porous medium within the cell.

2.6.7 Phase Trapping

Departure from very strongly water-wet conditions can give distinctly reduced oil entrapment. In 2-D pore network flow experiments (Li and Wardlaw, 1986) that permit observation of pore-level displacement mechanisms affecting displacement efficiency, it has been noted that residual oil is trapped as disconnected globules in the pore bodies of systems that were very strongly water-wet and had a high aspect ratio (i.e., high ratio of pore body to pore size) believed to be typical of reservoir rocks. Simulated waterfloods of crude oil from micromodels were also conducted at various wettability conditions by Li and Wardlaw (1986), and while a great variety of distributions has been observed, no crude-oil/brine system showed the extensive trapping of oil in the pore bodies that is characteristic of very strongly water-wet systems. They also showed that snap-off in simple pore models of rectangular cross sections can be inhibited if the water-advancing contact angle exceeds 60º.

2.7 Determination of Reservoir Wettability

The wettability of a porous hydrocarbon reservoir system cannot be measured directly but by using indirect methods such as the Amott test, the USBM test, and contact angle measurement to determine with some certainty the distribution of fluids and the wetting condition of the porous media system.

There are many different ways for measuring the wettability of a system. They include quantitative methods, such as contact angle measurement, imbibition/forced displacement (the Amott method), the United States Bureau of Mines (USBM) wettability method, and qualitative methods, such as imbibition rates, microscope examination, flotation, glass slide method, relative permeability curves, and more. Although no single method is accepted by everyone, three quantitative methods are generally used:

1. Contact angle measurement.
2. The Amott method.
3. The USBM method.

The contact angle is a measure of the wettability of a specific surface, while the Amott and the USBM method measure the average wettability of a core.

2.7.1 Contact Angle Method

When two immiscible fluids are in contact the fluids are separated by a well-defined interface, which is only a few molecular diameters thick. When the interface is in intimate contact with a solid surface it intersects the surface at an angle, the contact angle, θ, which is a function of the relative adhesive tension of the liquids to the solid.

The contact angle is the best wettability measurement method when pure fluids and artificial cores are used because there is no chance of surfactants or other compounds altering the wettability (Anderson, 1986). Some of the methods used to measure the contact angle include: the tilting plate method, sessile drop or bubbles, vertical rod method, tensiometric method, cylinder method, capillary rise method, and the Dual Drop Dual Crystal method.

2.7.2 The Amott Method

The Amott method combines imbibition and forced displacement to measure the average wettability of a core. In this method both reservoir core and fluids can be used. The Amott method is based on the principle that the wetting fluid will generally imbibe spontaneously into the core, displacing the non-wetting one. The ratio of spontaneous imbibition to forced displacement is used to reduce the influence of other factors, such as relative permeability, viscosity, and the initial saturation of the rock.

Usually the core is prepared by centrifuging under brine until the residual oil saturation is reached. The following four steps are then executed in the Amott method:

1. Immersion of the core in oil and measurement of the volume of water displaced by the spontaneous imbibition of oil after 20 hours.
2. Centrifuging of the core in oil until the irreducible water saturation is reached and measurement of the total amount of water displaced, including the volume displaced by spontaneous imbibition.
3. Immersion of the core in brine and measurement of the volume of oil spontaneously displaced by the imbibition of water after 20 hours.
4. Centrifuging of the core in brine until the residual oil saturation is reached and measurement of the total amount of oil displaced.

Preferentially water-wet cores have a positive displacement-by-water ratio and a zero value for the displacement-by-oil ratio. The displacement-by-water ratio approaches one as the water-wetness increases. Similarly, oil-wet cores have a positive displacement-by-oil ratio and a zero

displacement-by-water ratio. Both ratios are zero for neutrally wet cores. The time period for the spontaneous oil and water imbibition steps were chosen arbitrarily, but it is recommended that the cores be allowed to imbibe until either imbibition is complete or a pre-set maximum time limit has been reached. Imbibition can take from several hours to more than two months to complete.

2.7.3 Wettability Indices

The direct effect of wettability on capillary pressure has prompted several investigators to define a wettability number. The two mostly used indices are the Amott index and the USBM index. However, it should be stressed that (i) these numbers capture only part of the shape of the curves and (ii) for the description of displacement processes, the complete relative permeability and capillary pressure curves are required, instead of a single wettability index. Wettability indices may give only an (incomplete) wettability characterization of a reservoir rock, but still can be useful in the design of correlations.

The Amott index is based on the amount of spontaneous imbibition of a certain phase. For water, the Amott index I_w is defined as (see Figure 2.10):

$$I_w = \frac{S_{spw} - S_{cw}}{1 - S_{cw} - S_{or}}$$

Similarly, the Amott index for oil I_o is defined as:

$$I_o = \frac{S_{spo} - S_{or}}{1 - S_{cw} - S_{or}}$$

For an extremely water-wet system I_o will be zero, while for an oil-wet system I_w equals zero. Clearly, the shape of the capillary pressure curve is not taken into account in the Amott index.

$$U = {}^{10}\log \frac{A_w}{A_o}$$

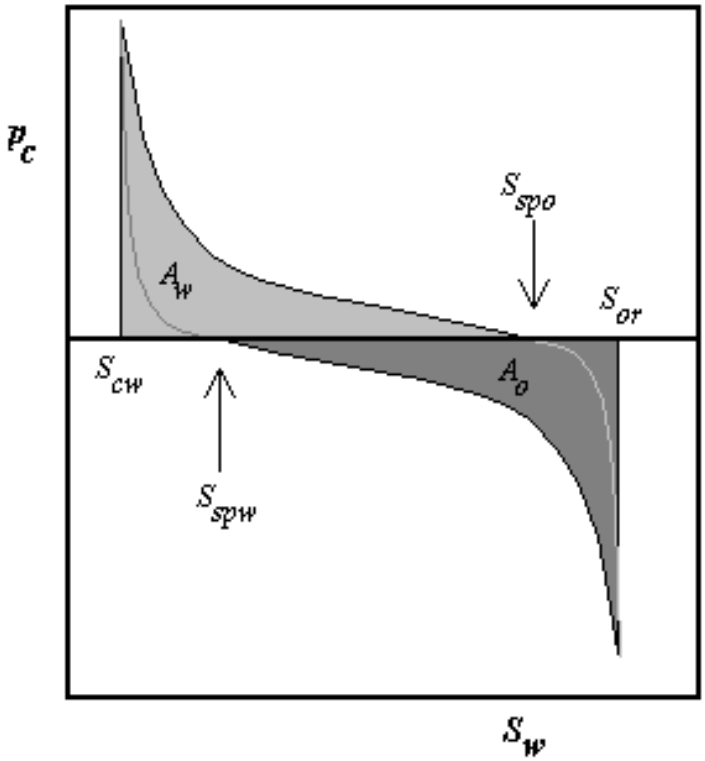

Figure 2.10: Imbibition and drainage capillary pressure curve for determining Amott and USBM wettability indices.

For an extremely water-wet system *U* is very large and positive, for an intermediate-wet *U* lies around zero and for an extremely oil-wet system *U* will be very large and negative. Finally, it should be mentioned that the USBM number defined above is usually referred to as the modified USBM index. The standard USBM index is calculated in an identical way from raw centrifuge capillary pressure data, using the average saturation instead of that at the inflow end. However, the raw data need considerable correction (saturation shift) before one arrives at a more truthful representation of capillary pressure p_c.

2.8 Changes in Wettability

Wettability alteration could be related to geometric parameters during oil invasion. When oil invaded the initially water-wet pore space, its distribution was controlled by both pore size and prevailing capillary pressure: the largest pores were invaded by oil while the smaller ones remained oil free. Aging then caused adsorption of polar oil compounds on the exposed surface. Spontaneous imbibition of oil could therefore be due to a continuous pore network within the oil-wet intergranular mesopores, whilst spontaneous imbibition of brine could be related to brine circulation in water-wet micropores of the calcitic cement. Microscopic studies of oil-brine-rock systems (coupled with other imaging techniques such as the X-ray computed tomography) contribute to a better understanding of intermediate wettability causes and can thus explain the macroscopic behavior of some reservoir rocks.

As stated above, few, if any, hydrocarbon reservoirs are strongly water-wet and many soils contaminated by oil often display oil-wet characteristics. The reason for this is that the prolonged contact of oil with the solid surface allows surface-active components of the oil to adhere to the solid surface, changing its wettability Buckley et al., (1998). For strongly water-wet media the different displacement mechanisms for multiphase flow are well established from micro-model studies (Lenormand et al., 1983) and have been used in pore-scale models to explain a variety of phenomena, including relative permeability hysteresis, and trends in residual oil saturation Blunt (1997). For media of arbitrary wettability, there is less direct experimental evidence of the appropriate pore-scale arrangements of fluid and their macroscopic consequences. However, outlined in this work is a simple and appealing theoretical pore level scenario for wettability alteration that appears to capture the pertinent physics of non-water-wet displacement.

Kovscek et al. (1993) proposed a pore-level model of wettability change and fluid distribution. Consider a displacement sequence that mimics oil migration and production in a hydrocarbon reservoir. Initially we consider the reservoir rock to be completely saturated with water-wet. During oil migration, oil invades the pore space. The part of the rock surface directly contacted by the oil changes wettability. Regions of the pore space for which a thick wetting film of water coats the surface remain water-wet, as do the corners of the pore space where water still resides. The degree of wettability alternation depends on the composition of the oil and water, the mineralogy of the solid surface and the capillary pressure imposed during primary drainage (Buckley et al., 1998; Kovscek et al., 1993). In laboratory studies, wettability alteration typically takes 40 days to complete. This is a shorter time than oil resides in reservoirs before being produced or even typical residence times for oil in polluted aquifers. Then the oil is displaced from the pore space by flooding with water. During this process we assume that the wettability does not change.

Kovscek et al. (1993) examined the pore-scale configurations of fluid and the macroscopic behavior for a bundle of parallel tubes with a grain boundary shape. Within a single pore, the surfaces have different wettability, for a triangular pore. This results in a number of different possible fluid configurations during waterflooding. If portions of the pore wall are oil-wet, then water re-enters the pore-space as the non-wetting phase and occupies the centers of the pore-space. Oil may reside as a layer sandwiched by water in the corner and water in the center. This provides connectivity of the oil and allows for very low residual oil saturations to be reached. Using this pore-level scenario the effects of waterflood relative permeability on wettability have been explored in detail using network modeling (Dixit et al., (1998, 1999); Blunt (1998).

Laboratory experimental results can be successfully reproduced if available pore-networks that represent the real structure of the porous medium of interest are combined with a better knowledge of pore-scale physics. However, most studies have been performed on either cubic networks or on a relatively homogeneous network representing just one particular sandstone - Berea. According to (Arns et al., 2003, 2004), Micro-CT (micro-focused computed tomography) scanning has enabled the pore structure of a wide range of rock samples to be determined.

The objectives of this research are to determine the petrophysical properties that govern fluid flow and transport in the Agbada reservoir rock system using experimental and image scanning methods, determine the wetting state of the medium and estimate the amount of waterflood oil recovery using the Buckley-Leverett fractional flow method.

2.9 Pore Network Simulation of Waterflooding

2.9.1 Reservoir simulation

Reservoir simulation has become an integral part of the oil and gas operations for more than half a decade. A large proportion of reservoir engineers and scientists now specialise in the use of reservoir simulations to help make critical decision on recovery options, estimate reserves, and to diagnose and improve the performance of producing reservoirs. This development has been facilitated by advances in computing hardware, software design, and improved numerical algorithms and formulations. In order to manage and optimise hydrocarbon production, it has become necessary to model oil and gas recovery under different production scenarios. The purpose of simulation therefore is to estimate field performance (oil recovery) under one or more

producing schemes. Observation and analysis of model results that represent different producing conditions aid in the selection of optimal set of producing conditions for the reservoir.

A lot of work has been carried out on simulation to characterise oil recovery processes from petroleum reservoirs (Dicks, 1993; Marcondes, 1996; Granet et al., 2001; Giting, 2004; Gharbi, 2004; Ridha and Gharbi 2004; Hui and Durlafsky, 2005; Mago, 2006; Matus, 2006; Di Donato et al., 2007; Lu and Connell, 2007; Escobar et al., 2007; Clemens et al., 2013; Parvazdavani et al., 2013; Piller et al., 2014; Liu et al., 2015). These works have studied extensively reservoir simulation for optimizing recovery performance by fluid injection: water, water-alternating-gas, simultaneous water-alternating-gas, and gas injection in the bottom of the reservoir with water injection in the reservoir top.

Reservoir characterization process provides the physical parameters, such as size, resident fluid and rock composition and properties, which are needed by the mathematical model. Given the physical parameters, the mathematical model describes the fluid flow with a set of partial differential equations, initial and boundary conditions, and other relations, which are derived from physical principles. The processes occurring in petroleum reservoirs are basically fluid flow and mass transfer. Three immiscible phases (water, oil, and gas) flow simultaneously, while mass transfer may take place between the phases (chiefly between gas and oil phases). Gravity, capillary, and viscous forces all play a role in the fluid flow process (Peaceman, 1977).

In reservoir simulation, boundary condition requires that the reservoir lies within some closed curve across which there is no flow, and fluid injection and production take place at wells which can be represented by point sources and sinks, for example. A number of mathematical models

exist for the description of fluid flow in oil reservoirs. These can be divided into categories as to whether the fluid flow is considered to be compressible or incompressible and whether the fluid components are immiscible or miscible. The mathematical models that describe most isothermal flow situations are derived from four main physical principles. There are: conservation of mass of the fluid components; conservation of momentum; thermodynamic equilibrium, which determines how the fluid components combine to form phases, and lastly the condition that the fluid fills the rock pore volume. Several analytical models are available, but their application is restricted to small models, due to the complexity and mathematic effort required in most of the practical applications. So the solution for intermediate and large models is the numerical simulation.

2.9.2 Discretization methods

Different methods used in oil reservoir simulation, such as finite difference (Gatski et al. (2004), Ghia et al. (2005), Gustafson and Halasi (1996), Soh and Goodrich (2002), Goodrich et al.(1996), Kupferman (1994), and Guo (1998), finite element Di Donato et al.(2006), Escobar et al. (2007), finite volume methods Fletcher (2003), Gharbi (2004), Granet et al. (2001), Giting (2004), boundary element methods Giting (2004), Hui and Durhofsky (2005), a radial basis function network method Hirasaki and O'Dell (1970) and the lattice Boltzmann method Lu and Connell (2007) have been described in literature. The finite difference and finite volume methods are briefly considered below.

2.9.2.1 Finite difference method

Traditionally, numerical models based on the finite differences method (FDM) were developed for the discretization of the partial differential equations (PDEs) governing multi-phase flow in

porous media; finite element methods are generally not well suited to describe the fluid flow because they might not guarantee the conservation of mass (Faust and Mercer, 1976; Wan et al, 2003). Among the methods used in recent years to obtain better accuracy by using more complex grids that adapt to the flow patterns as determined by the reservoir geological features and by the well's architecture and pattern is the finite volume method (FVM). The FVM so far, has proven to work well in complex geometries and is already used in commercial fluid-dynamic simulators.

2.9.2.2 The Finite volume method

The finite volume method (FVM) is a discretization technique well suited for numerical simulations of various types (i.e., elliptic, parabolic or hyperbolic) of conservation laws. It is applied in many engineering fields, such as fluid mechanics, heat and mass transfer as well as petroleum engineering (Eymard et al, 1997). In the simulation of hydrocarbon reservoir, the finite volume method was first applied by Lemonnier (1979). The FVM, similar to other methods such as the FDM and the finite element method, provides the representation and evaluation of PDEs when expressed in the form of algebraic equations. The variables or parameter values are calculated in small volumes surrounding each cell node. These small volumes are known as the *finite volume*. The surface integrals are approximated by the sum of the fluxes through each of the sides of the control volume.

However, in this work, neither the FDM nor the FVM is used for the simulation of waterflooding process in the Agbada sandstone reservoir. Instead a model based on the use of elliptic functions, in particular, Weierstrass *p*-function is proposed.

2.9.3 Elliptic Functions

Elliptic functions appear here and there in diverse areas of applied mathematics such as cosmology (Kraniotis and Whitehouse 2002), chemical engineering (Koopman and Lee 1991), dynamical systems (Kotus and Urban´ski 2003), and quantum mechanics (Chow 2002). They are widely used in other branches of science and engineering, particularly, in mechanics and physics. In solid mechanics elliptic functions are used to model perforated plates and shells or doubly periodic system of cracks in plates and shells ([1-5] as well as in studies of screw dislocations motion in crystals [6]. In aero- and hydrodynamics, elliptic functions are used to describe the flow of fluids through doubly periodic lattice profiles [7], the motion of doubly periodic systems of point vortices [8-10]. They have been applied to fluid mechanics (Johnson and McDonald 2004, 2005; Hankin, 2006). They also provide interesting and instructive non-elementary examples of many results in complex analysis such as Cauchy's integral theorem and the residue theorem. Elliptic functions provide interesting and instructive examples of many ideas of complex analysis, and package elliptic illustrates these numerically and visually.

A meromorphic function f is said to be elliptic if $\exists\ \omega_1, \omega_2 \in \mathbb{C}$ with $\omega_2/\omega_1 \in \mathbb{C}\setminus\mathbb{R}$ such that

$$f(z) = f(z + 2m\omega_1 + 2n\omega_2) \tag{2.13}$$

whenever $f(z)$ is defined and $m, n \in \mathbb{Z}$ (Abramowitz and Stegun, 1965); ω_1 and ω_2 are called the half periods.

An elliptic function is a meromorphic function that is periodic in two directions, i.e., doubly periodic. It as a periodic function of non-zero variables defined by its values on a fundamental parallelogram and then repeats in a lattice. An elliptic function must have at least two poles

(counting multiplicity) in a fundamental parallelogram. The number of poles of an elliptic function in the fundamental parallelogram is called the order of an elliptic function.

For a non-zero (real) complex number, a function $f(z)$ is called *periodic* with period ω if $f(z) = (z + \omega)$ for all z. If two non-zero complex numbers ω_1 and ω_2 whose ratio is not real exist such that:

1. $f(z + \omega_1) = f(z)$ for all z
2. $f(z + \omega_2) = f|(z)$ for all z and
3. ω_1/ω_2 is not real

then $f(z)$ is doubly periodic. The doubly periodic function that is analytic except at its poles, and which has no singularities other than these poles in a finite part of the complex plane is called an *elliptic function*. The function $f(z)$ is uniquely determined and it is generally denoted by $P(z)$ and called the *Weierstrass P-function.* Therefore, the points 0, ω_1, $\omega_1 + \omega_2$ and ω_2 when taken in order are the vertices of a fundamental parallelogram.

2.9.3.1 Weierstrass elliptic functions

The Weierstrass elliptic functions (or Weierstrass *P*-functions) are elliptic functions which have a second-order poles at all nodes of the periodic lattice. The main function is the *P*-function, defined by the infinite sum:

$$P(z) = \frac{1}{z^2} = \sum_{m,n=-\infty}^{\infty}{}' \left(\frac{1}{(z-\omega)^2} - \frac{1}{\omega^2}\right) \tag{2.14}$$

where $\omega = m\omega$, $n\omega$ (m, n 0, 1, 2) are the nodes of the periodic lattice Λ. The prime indicates that the summation is taken over all non-zero periods of P, i.e., over all integer values of m and n,

except when $m = n = 0$. The subtraction of each $1/\omega^2$ plays two roles: it gives convergence of the series, and the right limiting behavior as z approaches zero.

The main property of the P-function that is of interest in this work is its double periodicity. As stated earlier, function $f(z)$ is generally denoted by $P(z)$. Therefore,

$$\left.\begin{aligned} P(z-\omega_1) &= P(z) \\ P(z-\omega_2) &= P(z) \end{aligned}\right\} \tag{2.15}$$

where ω_1 and ω_2 are the periods of the Weierstrass P-function.

Since $P(z)$ has zero residues, its anti-derivative is a single-valued function and can be expressed as:

$$\zeta(z) = -\int P(z)dz = \frac{1}{z} + \sum{}' \left(\frac{1}{z-\omega} + \frac{1}{\omega} + \frac{1}{\omega^2}\right) \tag{2.16}$$

where $\zeta(z)$ is known as the Weierstrass zeta-function and the summation is taken over all non-zero periods of P.

Anti-derivative of the zeta-function yields the Weierstrass sigma-function, expressed as:

$$ln\sigma(z) = ln\, z + \sum_{m,n=-\infty}^{\infty}{}' \left\{ln\left(\frac{z-\omega}{\omega}\right) + \frac{z}{\omega} + \frac{z^2}{2\omega^2}\right\} \tag{2.17}$$

The functions $\sigma(z)$ and $\zeta(z)$ are not elliptic and do not possess the property of double periodicity. They are quasi-periodic and satisfy the following conditions:

$$\left.\begin{aligned} \zeta(z+\omega_1) &= \zeta(z) + \eta_1 \\ \zeta(z+\omega_2) &= \zeta(z) + \eta_2 \end{aligned}\right\}$$

and

$$\left.\begin{aligned} \ln\sigma(z+\omega_1) &= \ln\sigma(z) + \eta_1 \\ \ln\sigma(z+\omega_2) &= \ln\sigma(z) + \eta_2 \end{aligned}\right\}$$

The values η_1, η_2, ω_1 and ω_2 are not independent; they are related by the Legendre identity. According to Legendre: if ω_1, ω_2 is a pair of basic periods, with $Im(\omega_2/\omega_1) > 0$, then,

$$\eta_1\omega_2 - \eta_2\omega_1 = \pi i \tag{2.18}$$

where $\eta_1 = \zeta(\omega_1)$ and $\eta_2 = \zeta(\omega_2)$.

The lattice generated by ω_1 and ω_2 is also denoted as $\Lambda(\omega_1, \omega_2)$ to make clear that it depends on ω_1 and ω_2. The two generators ω_1 and ω_2 are the lattice basis. They complex numbers that can be fixed arbitrarily with the main restriction that

$$Im(\omega_2/\omega_1) > 0$$

The fundamental parallelogram defined by the vertices 0, ω_1 and ω_2 together with the lattice Λ, spanned by periods ω_1 and ω_2, are shown in Figure 2.11. If $\tau = \omega_2/\omega_1$ is defined to be the half-period ratio, then the lattice basis can always be chosen so that τ lies in a special region, called the fundamental domain

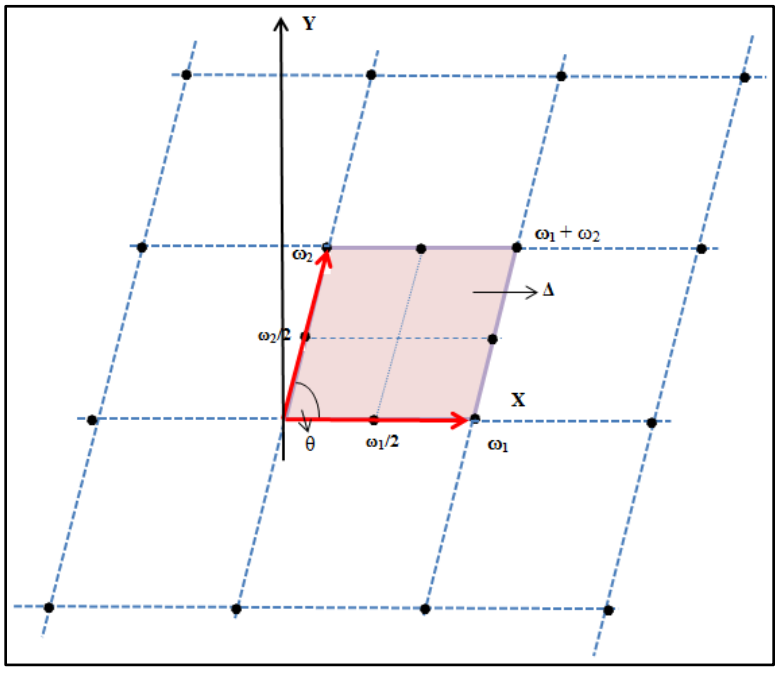

Fig. 2.11.: Fundamental parallelogram with a doubly periodic lattice spanned by periods ω_1 and ω_2, in the complex plane.

It is possible to transform a potential flowfield into another form using a conformal mapping from the z- plane to the ζ- plane, traditionally denoted ζ = f(z). This technique finds application when flow is desired (in the ζ- plane) that obeys some specific boundary condition that is simple to specify in the z- plane. In this case, we seek a conformal transformation that maps the upper half plane to a rectangle. If we consider the flowfield shown in Figure 2.11, then the map given by:

$$\zeta = \int \frac{dz}{\sqrt{(1-a^2z^2)(1-z^2)}} \tag{2.19}$$

takes the upper half plane of the ζ- plane to a rectangle in the z- plane (Milne-Thomson 1949). This is equivalent to z = sn(ζ;m), where sn(·,·) is a Jacobian elliptic function and *m* a constant of integration.

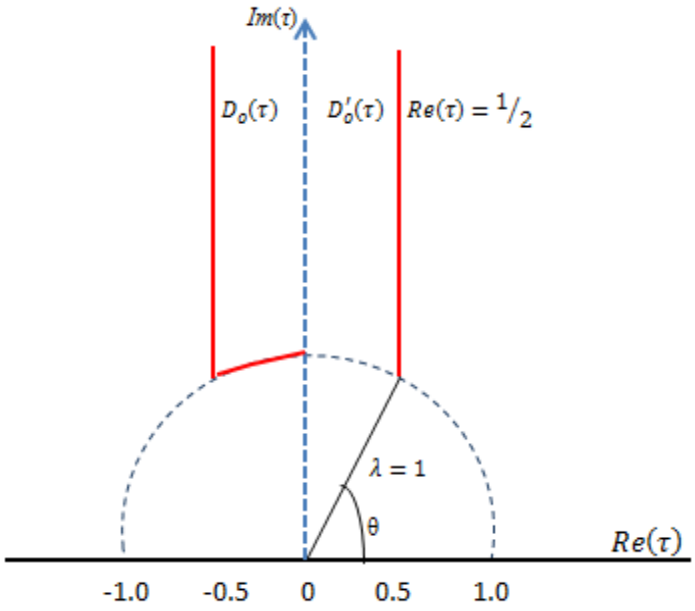

Fig. 2.12: The fundamental and half-domains for τ

Chapter 3

Materials and Experimental Procedures

3.1 Introduction to sampling location

The Niger Delta region, shown in Figure 3.1, is situated on the Gulf of Guinea on the west coast of Central Africa (South of Nigeria), and forms one of the world's major hydrocarbon provinces. It is 130 km long by 60 km wide and extends from the lower Benue trough in Nigeria to South-western Cameroon where it narrows and terminates under the Cameroon volcanic region. It covers an area between longitude 4 – 9º E and latitude 4 - 9º N. The *depobelts of the Niger Delta* basin form one of the largest regressive deltas in the world with an area of about 300,000km^2, sediment volume of 500,000km^3 and reaches maximum thickness of about 12 km.

3.1.1 Geological setting and hydrocarbons generation

The primary source rock in the Niger delta region is the Upper Akata formation, the marine-shale facies of the delta, with possibly contribution from interbedded marine shale of the lowermost Agbada formation. Oil is produced from sandstone facies within the Agbada formation, however, turbidite sand in the Upper Akata formation is a potential target in deep water offshore and possibly beneath currently producing intervals onshore. The tertiary section of the Niger Delta is divided into three formations, representing prograding depositional facies that are distinguished mostly on the basis of sand-shale ratios. These are:

1) The Akata formation situated at the base of the delta which is of marine origin and composed of thick shale sequences (potential source rock), turbidite sand (potential reservoirs in deep water), and minor amounts of clay and silt. The process started in the Paleocene and through the

Recent, the Akata formation formed during lowstands when terrestrial organic matter and clays were transported to deep water areas characterized by low energy conditions and oxygen deficiency. The formation underlies the entire delta, and is typically over-pressured.

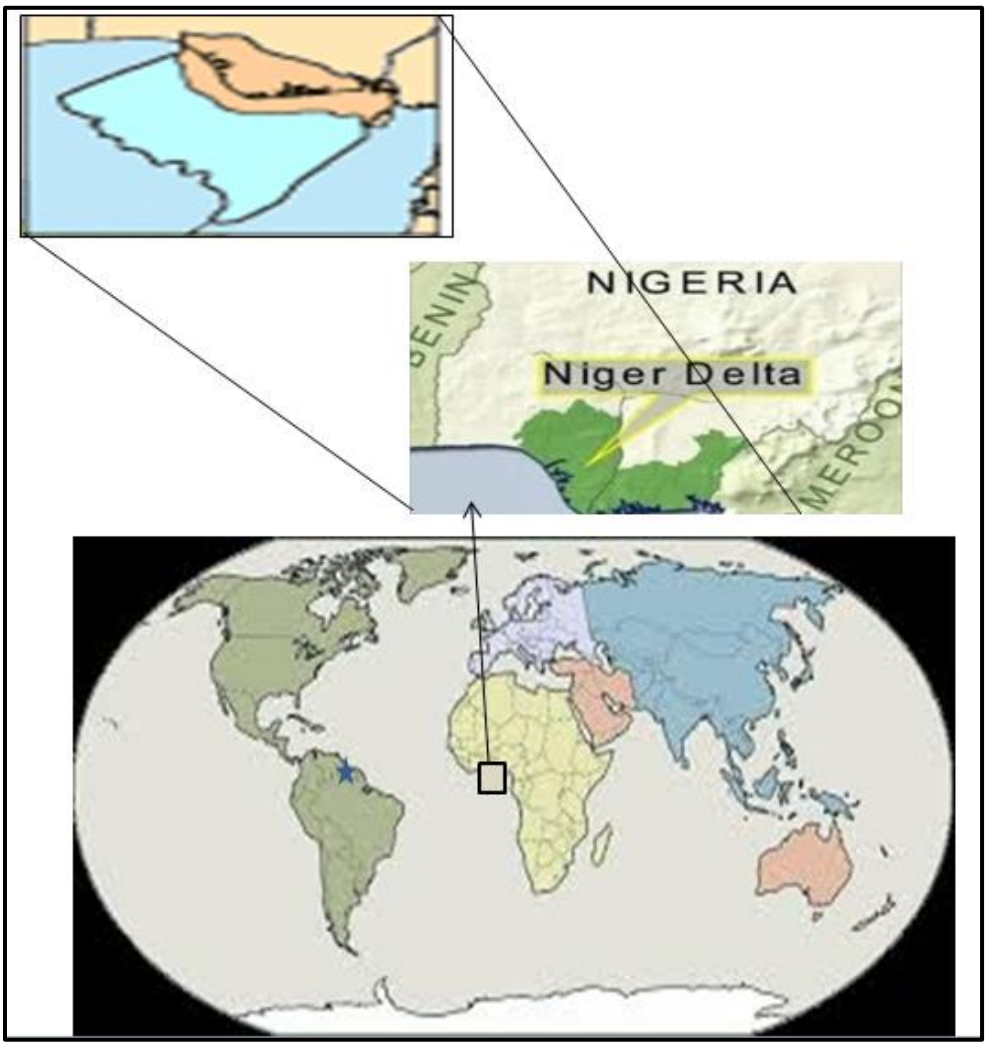

Figure 3.1: Niger delta province in the World map.

2) The deposition of the overlying Agbada formation, the major petroleum-bearing unit, began in the Eocene and continues into the Paleocene. The formation consists of paralic silica-clastics over 3700 meters thick and represents the actual deltaic portion of the sequence. The clastics accumulated in delta-front, delta-topset, and fluvio-deltaic environments. In the Lower Agbada

formation, shale and sandstone beds were deposited in equal proportions. However, the upper portion is mostly sand with only minor shale interbeds. 3) Overlying the Agbada formation is the Benin formation, a continental Late Eocene to Recent deposit of alluvial and upper coastal plain sands that are up to 2000 m thick (Pusey, 1973). Figure 3.2 shows the seaward extension of the Niger delta, which has advanced over a distance of 200 kilometers and has widened from less than 300 kilometers to about 500 kilometers

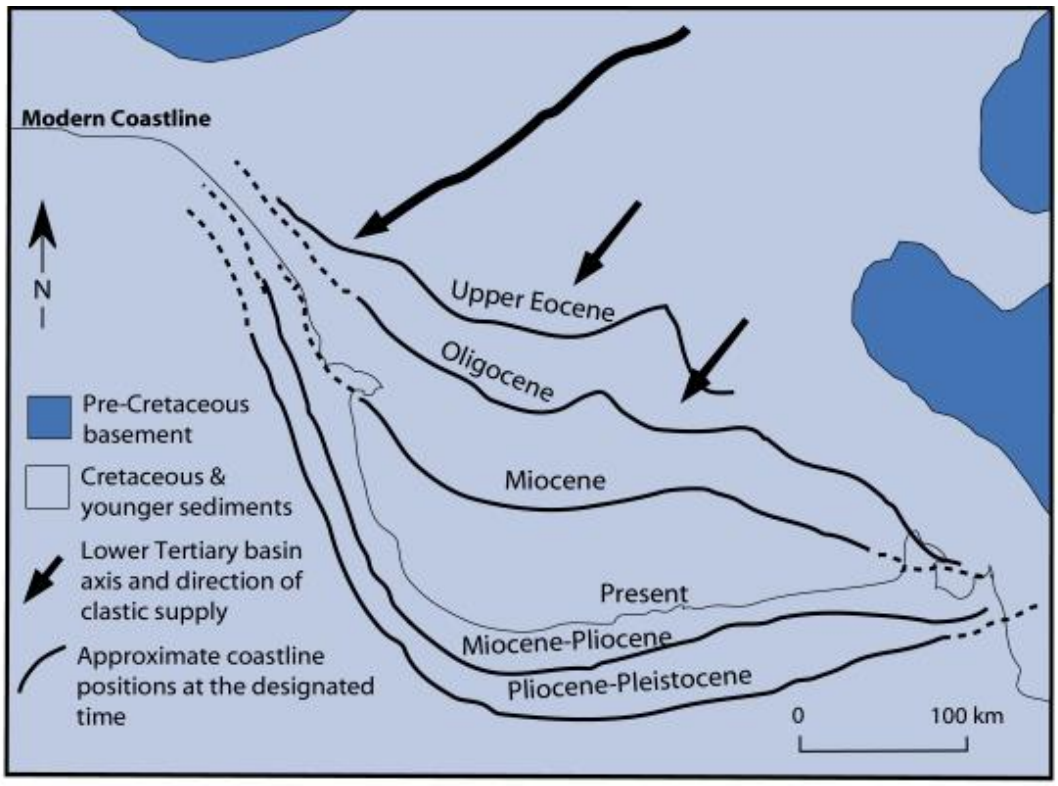

Figure 3.2: Progression of the Niger delta coastline (Modified from Whiteman, 1982)

3.1.2 Lithostratigraphy

The lithostratigraphy consists of three broad formations. The oldest formation in Niger Delta is the Akata Formation, dominated by hemipelagic shales. Overlying the Akata Formation is the Agbada Formation which consists of paralic sequence of sandstones and shales intercalation. The sandstone to shale ratio tends to decrease with depth. The youngest facie is the continental

sediments known as Benin Formation. Overlying the Agbada Formation, it consists predominantly of fresh water bearing continental mudstones, poorly sorted sandstone and gravels. Most of the hydrocarbon generated in Niger Delta is derived from both Akata and Agbada formations. Figure 3.3 is a section of the sedimentary layers, while Figure 3.4 shows a cross section of the lithostratigraphy of the Niger delta.

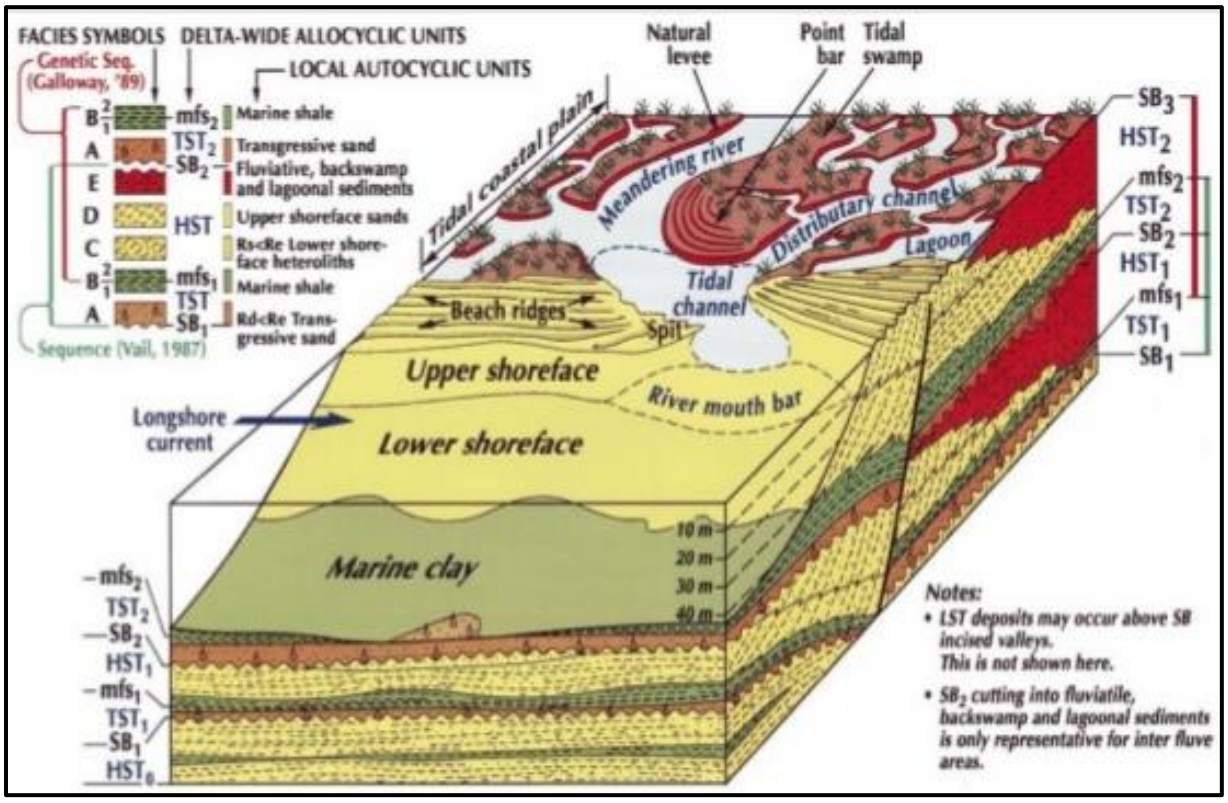

Figure 3.3: Geological section showing sedimentary layers of the Niger delta mouth
(Ruhr University Bochum, 2014)

Some of the unconsolidated sands in the Agbada petroleum system have minor component of argillo-silicic cement (Kulke, 1995). Characteristics of the reservoirs in the Agbada Formation are controlled by depositional environment and by depth of burial. The primary reservoirs in Niger Delta are dated Miocene age and described to be paralic sandstones with about 40% porosity, 2 darcy permeability, and with a thickness of 100 meters. The Agbada Formation has a

minimum thickness of 3,000 m. Mineralogy of the Agbada sandstone indicates the following: quartz ranges from 58 to 85%, albite from 16 to 24%, calcite from 2 to 6%, dolomite from 0.5 to 4%, kaolinite from 2 to 6% and muscovite from 0.5 to 3% (Tuttle et al., 1999). The grain size of the reservoir sandstone is highly variable with fluvial sandstones tending to be coarser than their delta front counterparts; point bars fine upward, and barrier bars tend to have the best grain sorting. Porosity only slowly decreases with depth because of the young age of the sediment and the coolness of the delta complex.

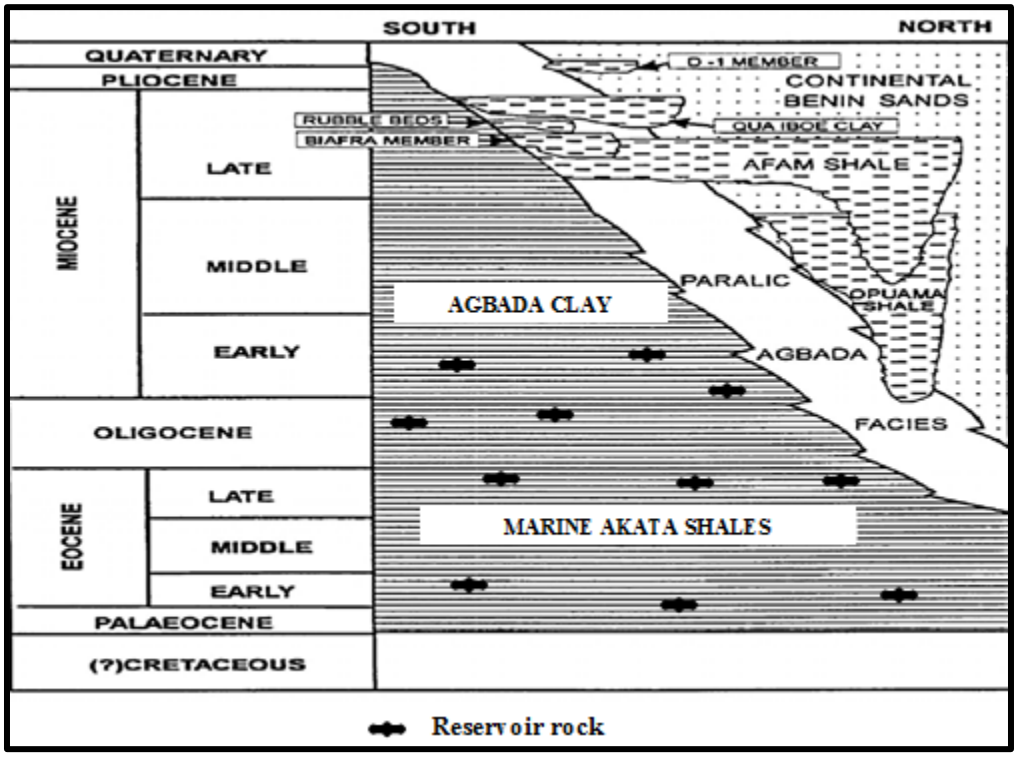

Figure 3.4: Lithostratigraphical cross section across the Niger Delta (Modified from Jubril M.A. et al., 1991)

3.1.3 Properties of oil in the Niger delta

The physical and chemical properties of the oil in the Niger Delta are highly variable, even down to the reservoir level. The oil in the delta has API gravity range of 16-50°, with the lighter oils having a greenish-brown color (Whiteman 1982). Fifty-six percent of Niger delta oils have API

gravity between 30° and 40° (Thomas, 1995). Most oils fall within one of two groups: 1) light paraffin based, waxy oils from deeper reservoirs (wax content up to 20%, but commonly around 5%, with high n-paraffin/naphthene ration of 0.86 (Doust and Omatsola, 1990; Kulke, 1995) and, 2) biodegraded oils from shallow reservoirs. They have lower API gravity of 26° average (Kulke, 1995) and are naphthenic non-waxy oils, with n–paraffin/naphthene ratio of 0.37. Biodegradation and washing is extreme in some Pleistocene sands of the Agbada Formation, forming extra heavy oils (API 8-20°). Oils with less than 25° API account for only 15% of the Niger delta reserves (Thomas, 1995). Sulfur concentration in most oils is low, between 0.1 % and 0.3 %, with a few samples ranging up to 0.6 %.

3.2 Materials

3.2.1 Core samples

The core samples used in this work were from Agbada Sandstone from different oilfields in the Niger delta petroleum system.

3.2.2 Preparation of core samples

3.2.2.1 Cutting and Trimming.

Experiments were performed on twelve (12) whole reservoir core samples taken from different oil bearing Agbada sandstone formations. The fields from which these samples were taken are identified as A to F. Two samples were taken from each field, representing various well depths and lithology. Twenty four (24) core plugs of approximately 3 inches in length and 1.5 inches in diameter each were cut from these whole cores at 0.5-foot intervals. Figure 3.5 shows a sample of the sandstone core plug used in the experiments in this work. After trimming the plugs' edges

were cleaned of fines using the Acetate Peel method. The plugs were wrapped with silver paper and then placed in sealed container completely submerged in evacuated brine.

3.2.2.2 Acetate Peel to remove rock flour

The method used for the removal of rock fines from the plug end faces is an adaptation of the stained acetate peel technique described by Katz and Friedman (1965). The acetate peel technique is used to remove rock flour from flat end faces and curved surfaces of plugs and whole cores during cleaning Although this technique was first used to produce rapid stained peels of limestones as a representative thin section, it has been used extensively and has proved to be very successful in removing the bulk of the rock flour from the plug end faces of sandstone and carbonate rock types.

Figure 3.5: Agbada sanstone reservoir core plugs used in this work

A square section of acetate sheet approximately twice the size of the plug end face diameter was submerged completely in acetone solvent for about 1 minute until it became jelly-like. This was then attached to a dry acetate sheet square and as soon as the jelly acetate was attached to the dry acetate sheet, the wet surface was applied to the plug face and rubbed gently until no air bubbles were observed. The plug plus acetate sheet was then left to dry out at room conditions overnight. The dried, hardened acetate sheet was then carefully peeled off the end face of the plug, which now appeared cleaner. All the 24 samples were subjected to this fines removal process.

3.2.2.3 Core cleaning and saturation

The Soxhlet extractor is the most commonly used apparatus for cleaning cores in the laboratory It provides a simple and gentle distillation of the fluids and salts within a core plug. The process can be slow, ranging from several days to several weeks, depending on the properties of the pore fluids and the rock permeability (Torsæter and Abtahi, 2003). Other disadvantages are the fact that solvent may not contact all pores in the core due to small pore throats and occasionally the solvent can cause alterations in wettability (Gant and Anderson, 1988). Different types of solvents are used according to the fluids being removed and it is important that the solvent employed does not react with the minerals in the core. For cleaning out oils it is common to use toluene as solvent. In this case the core plugs were initially oil-free and methanol was used to remove any salt or interstitial water.

The samples were cleaned by Distillation/Extraction method (Gant and Anderson, 1985). In this method, the samples were placed in a Soxhlet apparatus; the solvent was continuously distilled, condensed, and then distributed over the top of the samples (Figure 3.6). Toluene was used as the

cleaning solvent. The cleaned samples were dried in an oven at a temperature of 110 ^{0}C for 60 hours. The dried core samples were weighed on a balance. The samples were then placed under vacuum for an hour, after which they were saturated with deaerated brine under vacuum for 7 days to allow for ionic equilibrium of the brine with the core samples.

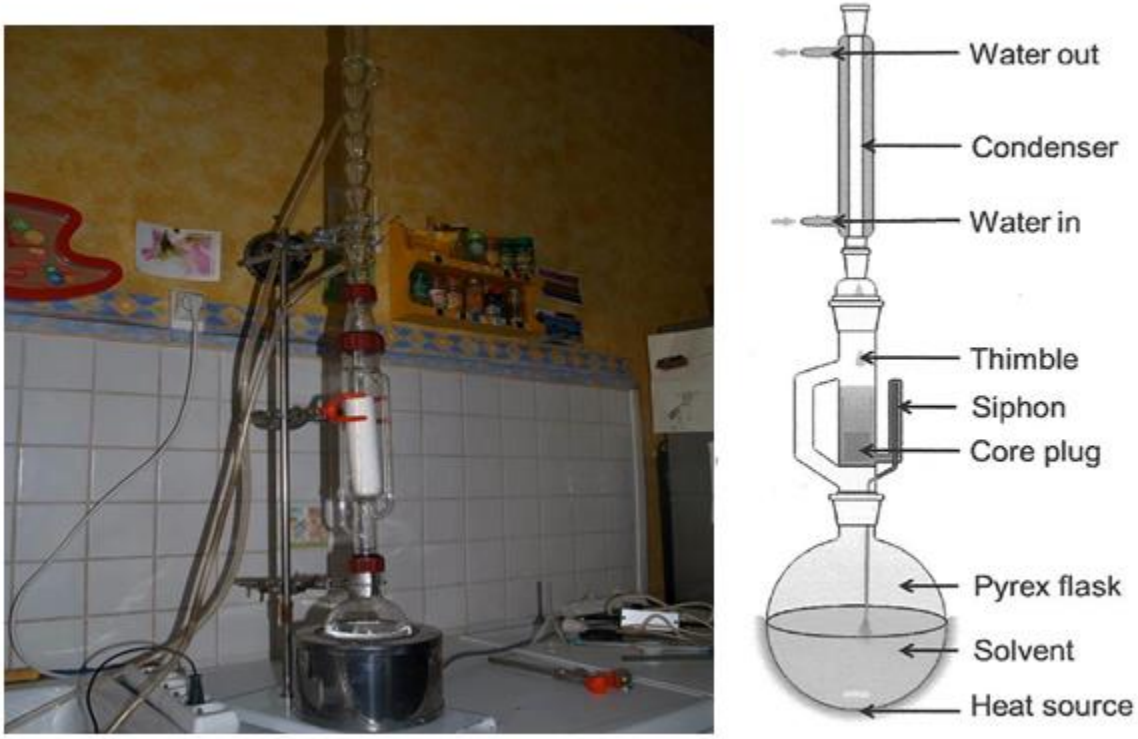

Figure 3.6: Soxhlet Extraction apparatus

3.3 Porosity measurements

Porosity is measured on plug samples after they have been cleaned and dried to remove all reservoir fluids and residual salts by injecting the sample with helium. Core analysis provides simple determination of porosity as we do not need information about the minerals composition or borehole effects. By measuring two out of three quantities, bulk volume, pore volume or grain volume, porosity can easily be determined by equations (3.1 - 3.3). A drawback is that a core plug represents a smaller rock volume than what can be reached by a logging tool. Therefore the

porosity values gathered from well testing are usually more accurate than from core analysis in heterogeneous reservoirs (Torsæter and Abtahi, 2003).

3.3.1 Dry weight and Bulk volume measurements

The dry weight of the core plug is an important parameter as it allows for porosity calculations as well as further density and saturation determinations. A scale with the precision of 0,01g was used to weigh the core plugs. For core plugs of non-geometric shapes, bulk volume is normally determined by observing the displaced volume of a fluid with known density with a plug immersed in the fluid. The fluid must be prevented from entering the pore spaces of the rock, either by coating the plug, fully saturating it with the same fluid in advance or by using mercury. In volumetric procedures the displaced volume of fluid is used directly to calculate the bulk volume. In gravimetric determination the loss in weight of the plug immersed in a fluid or the change in weight of a pycnometer with and without the plug is observed.

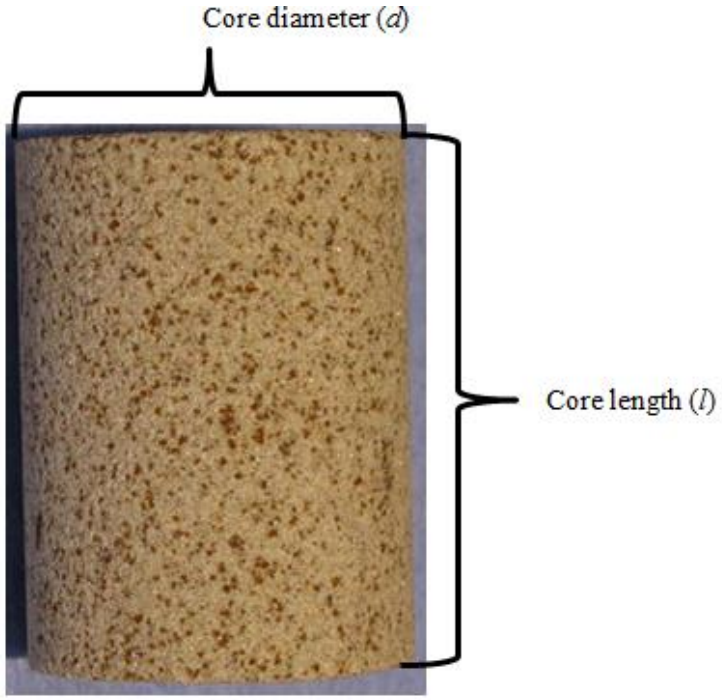

Figure 3.7: Core Bulk Volume Measurement

In this experiment the bulk volumes V_{bulk} of core plugs with uniform cylindrical shapes (all 24 samples) were determined by measuring the diameter, *d*, and length, *h*, of each core (See Figure 3.7) and applying the equation:

$$V_b = \pi(r^2)l \tag{3.1}$$

where *r* is the radius of the core plug and is equal to *d/2* and *h* is the length of the core plug.

3.3.2 Helium Porosimeter

This method relies on the expansion of helium gas, employing Boyle's law on a closed system under isothermal conditions and also measures the effective porosity of the rock. Helium is most often preferred as the measurement gas because it is a creeping little molecule that can penetrate even the smallest voids or pores. It is also an inert gas and dos not adsorb on the rock surface. Hence, this method provides slightly higher porosity measurements on any given rock sample. Figure 3.8 shows a schematic of the Helium porosimeter used in the work.

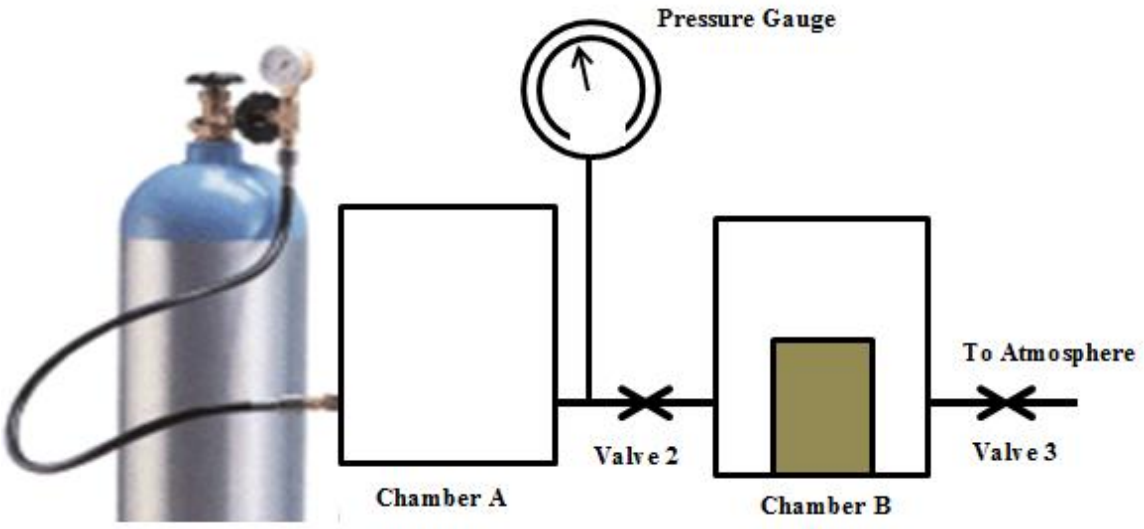

Figure 3.8: Schematic of Helium Expansion Porosimeter

With valve 2 closed, helium gas was introduced into chamber A of the apparatus through valve 1 (not shown) until a pressure p_1 was reached, then valve 1 was closed. This pressure was

arbitrarily fixed at 100 psi (which is common). The core sample was inserted into chamber B, which was at atmospheric pressure, p_{atm}, and then valve 3 was closed. Valve 2 was slowly opened to let the gas equilibrate through the entirety of both chambers. As the gas penetrated into the pores of the core sample the pressure decreased to a new stable level, p_2. The drop of pressure depends upon how much space there is in chamber B, and that depends on how much of chamber B is occupied by solid rock particles. The measured gas pressures p_1, p_{atm} and p_2 alone are not sufficient to obtain the volume of the sample core plug matrix. However, the system was calibrated by putting a range of metal cylinders of accurately known volume into chamber B and repeating the experiment. When this was done, the calibration constant, and the pressures allowed the volume of the core plug matrix V_{mat} to be obtained using the Boyle's law equation:

$$V_{mat} = \frac{P_{atm}V_1 + P_2V_2 - P_3(V_1 - V_2)}{(P_{atm} - P_2)} \tag{3.2}$$

The porosity was then calculated using the equation:

$$\varphi = \frac{V_{bulk} - V_{mat}}{V_{bulk}} \tag{3.3}$$

3.4 Permeability measurement

Permeability is a measure of the ability of a porous media to transmit fluids. It is a critical parameter in defining the flow capacity of a rock sample. Accurate measurement of permeability is critical for fluid flow modeling in porous media. According to Darcy, determination of the flow rate of water through a sand filter could be described by:

$$Q = \frac{KA}{L}(h_1 - h_2) \tag{3.4}$$

where Q (cc/s) represents the volumetric flow rate through a sand pack with cross sectional area A (cm) and length L (cm); h_1 (h_{in}) and h_2 (h_{out}) are the hydrostatic heads at the sand pack inlet

and outlet, respectively, and K (cm/s) is a constant of proportionality. Figure 3.9 shows a simplified schematic diagram of the experimental setup used by Darcy to study fluid flow I porous media. Darcy's experiments were however, confined to water flow through 100% water saturated sand packs. Further investigations showed that Darcy's law could be extended to other liquids and that the proportionality constant K could be replaced by μ/k, where k is the permeability of the rock, and μ is the viscosity of the fluid flowing through the rock. With this modification, Darcy's law can be written in a form suitable for our experiment as:

$$Q = \frac{kA}{\mu L}\Delta P \tag{3.5}$$

where Q is in cm^3/s, k is permeability in Darcy, μ is absolute viscosity in *mPa.*, A in cm^2, L is length in cm, and ΔP is pressure change along the sample in atm.

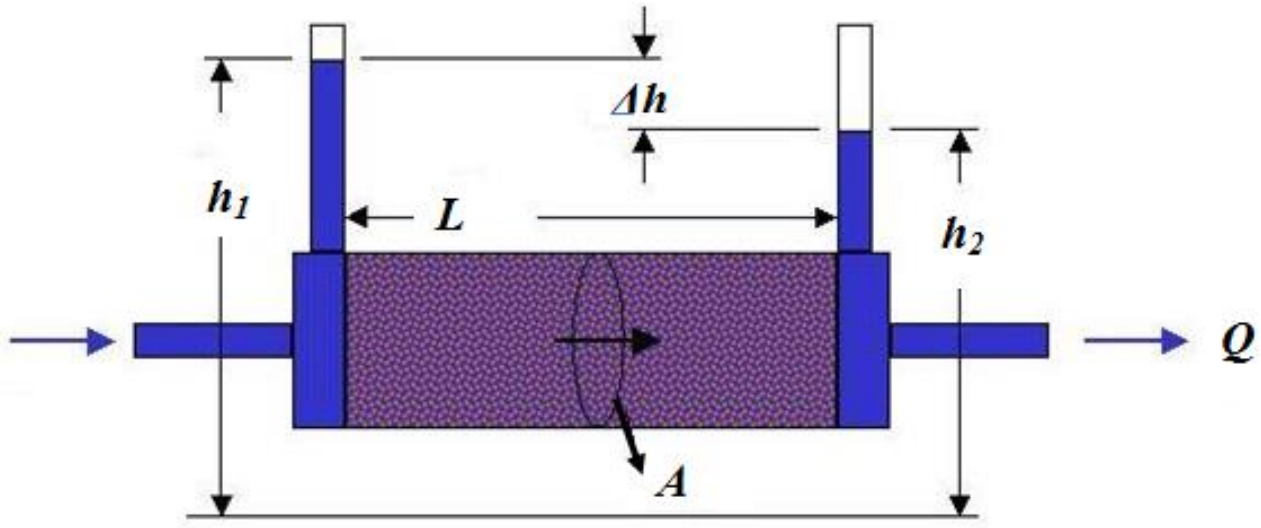

Figure 3.9: Schematic of Darcy's experimental setup for fluid flow in sandpack

Permeability is measured in the laboratory by encasing a core plug of known dimension in an air-tight sleeve (Hassler-type Core Holder) and injecting a fluid of known viscosity into the core plug while mounted in a steel chamber. The pressure drop across the sample and the flow rate are measured and permeability is calculated using Darcy's law above.

Various methods are used in the determination of permeability depending on core size, shape and consolidation, type of fluids used, available pressure and the permeability range. Air is used as the flowing fluid as it reaches rapidly steady-state, does not alter the minerals in the rock and it is easy to obtain 100 % fluid saturation.

Figure 3.6 illustrates the air permeameter setup. Air is run through the system and regulated by two valves, one on each side of the Hassler cell, where the core plug is placed. Manometers show the pressures P_1 and P_2 before and after the cell. The air flow rate, Q, can be read from the flow meter.

Each core plug was placed in the Hassler-type core holder and surrounded by a sleeve pressure of approximately 10 bar. This was to make sure that the air flow through the core was in the longitudinal direction only. The upstream and downstream valves were adjusted to maintain a constant pressure drop, $\Delta P = 0.4$ bar, and to provide laminar flow through the length, L, of the core. The permeability resulted from injection of nitrogen gas into the samples at a constant pressure until a constant flow rate of gas through the sample is attained (steady-state conditions). Four measurements were taken for each core and the air permeability, k_{air}, was calculated using equation (3.5). The liquid permeability of each core sample was determined using the Klinkenberg correction procedure.

A clean, dry core is mounted in a rubber sleeve of the appropriate size so the core and sleeve completely fill the core holder. The core and sleeve are then placed in the core holder and tightened securely into place. The flow tube selector valve is turned to a large setting and an

upstream pressure 0f 0.25 bar applied to the system by adjusting the regulator. The pressure gauge is tapped lightly during adjustment to stabilize the needle. The preferred range on the flow tube was between 20 and 140 divisions. If it remains below 20, the selector valve should be slowly turned to the medium setting. The barometric pressure was recorded (mmHg, corrected for temperature and latitude). Also recorded were pressure (bar), gas temperature (^{o}C) and flow rate tube reading (cm).

3.5 Wettability measurement

3.5.1 Experimental procedures and apparatus

3.5.1.1 Amott-Harvey method

The Amott-Harvey method utilizes imbibition and drainage processes in a two-fluid system to measure wettability. Twelve core plugs were used for initial wettability measurement. The clean and dry core plugs were first saturated with oil in a vacuum pump setup. The cores were placed in a beaker inside the vacuum chamber and the valve at the fluid holder was closed. The vacuum pump creates an under-pressure of approximately 50 bars to extract all fluids from the system. The valve connected to the pump was closed before gently opening the fluid valve. With all the valves closed the core plugs were completely soaked in oil and left to saturate for about 2 hours.

The fully saturated plugs were placed in imbibition cells surrounded by brine for 7 days to attain equilibrium (Figure 3.10 left). Brine imbibed into the core plugs and oil started to seep out, ascending to the graded cylinder at the top of the cell. The displaced volume was regularly noted to keep track of the rate of imbibition. After equilibrium was reached the total volume of oil displaced was recorded. The cores were then taken out of the cells, quickly dried and weighed.

Each core was placed in a centrifuge, surrounded by brine. The centrifuge could contain three holders at a time and each holder was carefully weighed and replenished with brine to get exactly the same weight. The centrifuge allows for a weight difference of < 0.03g between the three holders in order to be balanced and able to spin straight.

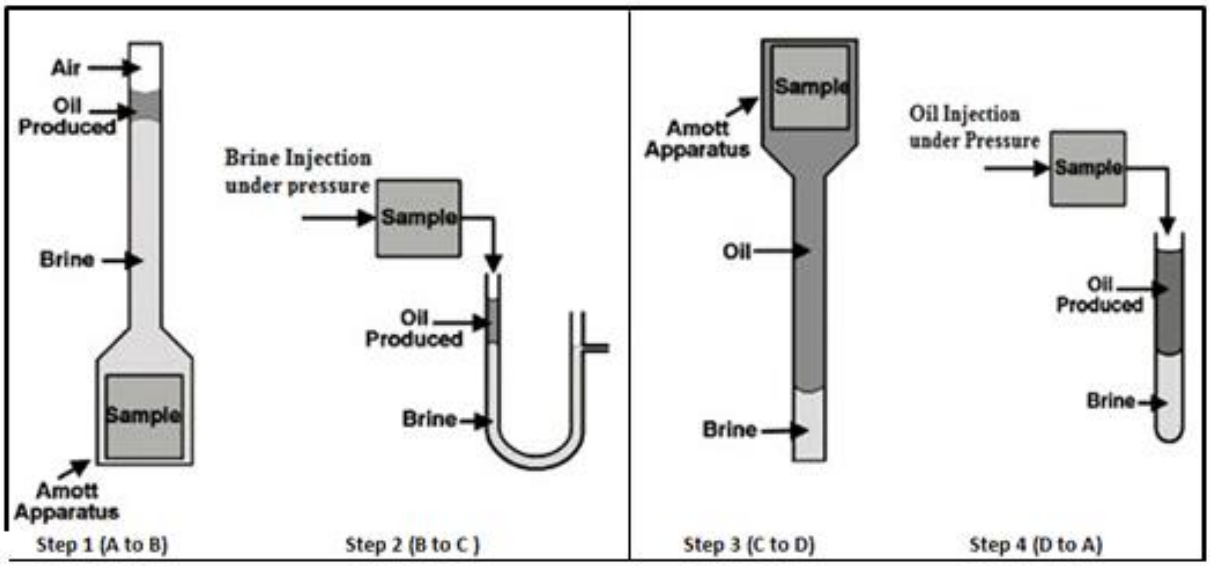

Figure 3.10: Amott Wettability Test Setup

The cores were centrifuged at 3000 rpm for approximately one hour to force the remaining oil down to residual saturation. Then the cores were taken out, quickly dried and weighed again. The difference in weight before and after the centrifuge was divided by the density difference between brine and oil to find the displaced volume of oil for each core. At this point all cores were saturated with brine at residual oil saturation. They were placed in drainage cells, as seen in Figure 3.10 right, and surrounded by oil for 7 days to allow for spontaneous drainage. Forced drainage by centrifuge was not applied as no brine was produced from the cores in the drainage cells.

The Amott-Harvey wettability index (*WI*) was calculated using equation (3.6), where V_{o1} and V_{o2} represent spontaneous and forced imbibition volumes. V_{w1} and V_{w2} represent spontaneous and forced drainage volumes, r_w stands for the ratio of oil displaced by brine and r_o stands for the ratio of brine displaced by oil. Amott-Harvey *WI* lies between -1.0 and +1.0 where *WI* = 0.3 – 1.0 complete water-wet; WI = 0.0 indicates neutrally-wet; and WI = -1.0 - -0.3 indicates completely oil-wet.

$$Amott - Harvey\ Wettability\ Index, WI = \frac{V_{01}}{V_{01}+V_{02}} - \frac{V_{w1}}{V_{w1}+V_{w2}} = r_w - r_0 \quad (3.6)$$

3.6 Coreflooding experiment

3.6.1 Materials

3.6.1.1 Core samples

In this study, five reservoir core samples with designations of A1 to E1 were used. These core samples were obtained from whole cores from different oil reservoirs as stated earlier. Also, porosity and permeability of cores were obtained using helium porosimeter and air permeameter respectively. Results obtained, and the mineralogy and rock properties of the core plugs are shown in Tables 4.1 and 4.2 respectively.

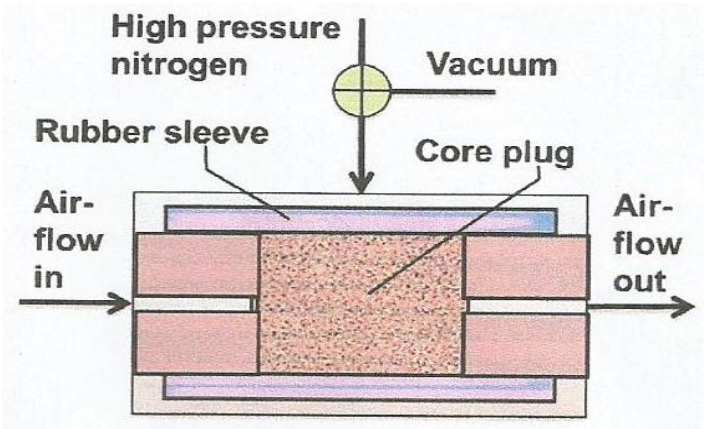

Figure 3.11: Schematic of Hassler cell

The waterflooding experimental setup is shown in Figure 3.12.

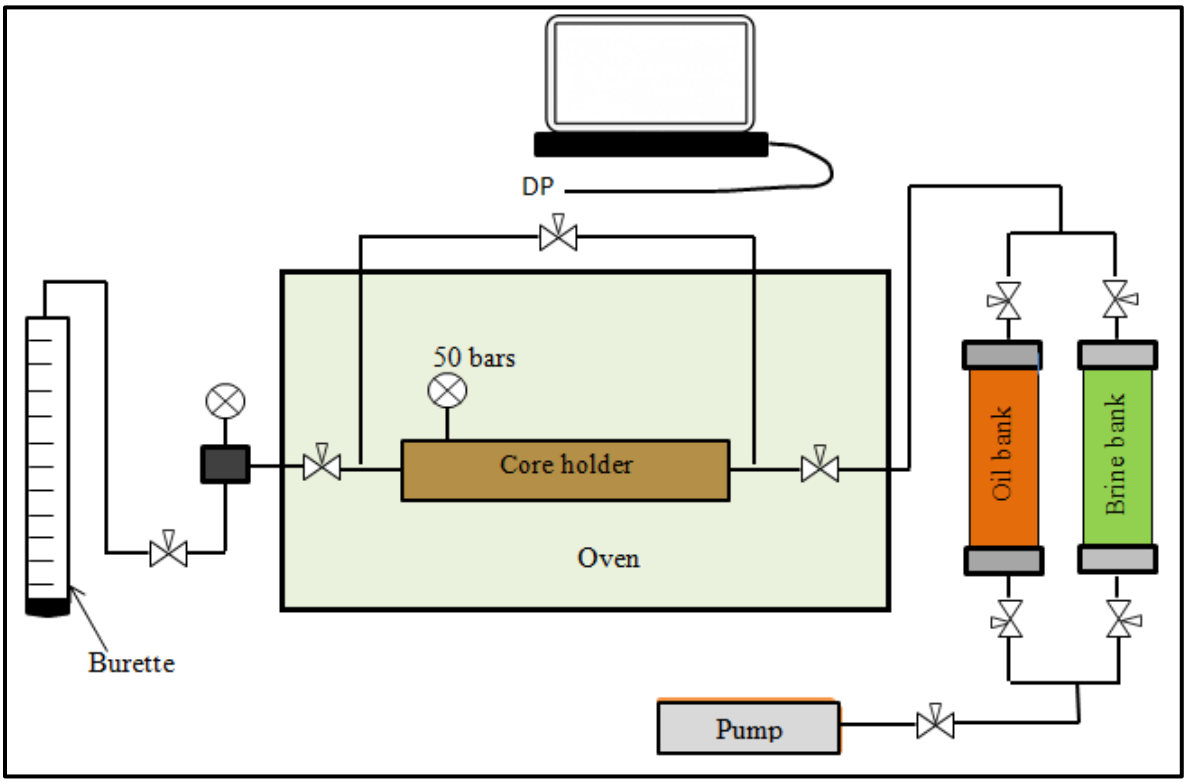

Figure 3.12: Schematic of experimental setup for core flooding

Water

The formation water used in the experiments was synthetic brine prepared in the laboratory by dissolving reagent grade salts in distilled water. Table 4.3 shows the composition of the formation water.

Crude oil

Two types crude oil were used for core saturation, the Bonny light and the Forcados crude oils. Filtered stock tank oil was used for aging the core samples. Table 4.2 indicates some properties of the oils at room temperature. Acid number was measured in the laboratory using modified ASTM D664 method.

3.6.1.2 Methodology

The Hassler cell (Figure 3.10) is a core holder fitted with a flexible rubber tube and an external pressure inlet connected to a nitrogen tank. These features give the cell excellent tightness, options for higher pressure drop (ΔP) across the cell and the possibility. Core samples were first saturated with brine for 10 days to allow for ionic equilibrium between the rock and the brine. The brine was then displaced by 5 PV of oil at 25 to 30 psi pressure drop as required to give initial water saturations close to 22%. The direction of oil flow was then reversed after 5 PV injection of oil to alleviate end effects and give uniform saturation distribution along the core. Next, the core samples were removed from core holder and aged in crude oil in sealed Pyrex jars at reservoir temperature (190 °F) for 40 days.

Before measuring rates of spontaneous imbibitions, the core, after aging, was flushed with fresh crude oil. All displacement tests were carried out under room temperature. Determination of oil recovery by spontaneous imbibition was done by calculating the change in weight of the core suspended under water. Expelled oil that remained attached to the core sample was removed with the aid of a PTFE rod prior to recording the core weight. To allow complete drainage of oil from the core samples, imbibition was allowed to take place for five days after which oil production stopped.

The samples were then waterflooded to determine the fraction of oil recovered by forced displacement. Finally the samples were restored to S_{wi} by oil flooding and then waterflooded at 5 psi injection pressure (flow rate was about 0.2 ml/s). Oil recovery vs. pore volumes of water injected was recorded.

3.7 Determination of Porosity and Permeability using x-ray Computed Tomography

Conventional routine laboratory techniques for determination of petrophysical properties of petroleum reservoir rocks such as porosity, pore distribution and permeability using core samples, in most cases, result in the destruction or modification of the core samples. In addition, they are time consuming and costly. X-ray computed micro-tomography is a non-destructive technique that is widely used to determine some petrophysical parameters of the rock sample that does not require elaborate preparation. The only preparation necessary for CT scanning is to ensure that the object fits inside the field of view and that it does not move during the scan. X-ray CT has the ability for visualizing interior features within solid objects, and for obtaining digital information on their 3-D geometries and properties.

The μ-CT set up consists of an X-ray source, the sample object through which the X-rays pass, and a detector that measures the extent to which the X-ray signal has been attenuated by the object. The imaging technique consists of directing X-rays at the sample object from multiple orientations and measuring the decrease in intensity along a series of linear paths. This decrease is characterized by Beer's Law, which describes reduction in intensity as a function of X-ray energy, path length, and the objects linear attenuation coefficient. A specialized algorithm is then used to reconstruct the distribution of X-ray attenuation in the volume being imaged.

X-ray CT data are generally sequential image files which can be visualized and analyzed using a wide variety of 2-D and 3-D-based image processing tools. The gray-level data values in X-ray CT images are generically called CT numbers. The 2-D and 3-D images of the core samples allow us to see the pore distribution, the size, and shape of pore volumes. In this work 3-D

images of the Agbada sandstone were generated using X-ray computed tomography and then a maximal ball algorithm was used to extract topologically equivalent network

A desktop micro-CT scanner ‘v|tome|x’ (Fig.3.13) located in the XMT laboratory at the Department of Materials, Imperial College London, was used. v|tome|x is a high-resolution µCT system manufactured by Phoenix|x-ray in Germany and equipped with an image acquisition and processing software, SIXTOS. The X-ray tube of this nano-focus system has a focal spot size less than 1 µm. However, in practice, we use 1.5 µm focal spot size to obtain sufficient photon flux passing through the rock samples and responsed by the detector. The 16-bit digital X-ray detector of this system is a flat panel detector, Perkin Elmer RID 512-400 based on an 8” amorphous silicon sensor with a pixel size of 400µm and a field of view of 512 × 512 pixels.

Figure 3.13: Micro-CT scanner, Phoenix vltomelx, at Imperial College, London

3.7.1 Basic Setup

The Phoenix vltomelx system, Figure 3.13, has the following components in its basic setup: the X-ray source, a manipulator sample stage that can position and rotate the sample with high precision and a detector to receive the attenuated profiles as raw information for reconstruction. Computer is used to control the X-ray source and the scanning parameters as well as to perform the reconstruction software to transform the radiographic images (attenuation profiles) to the interior volumetric view of the sample.

Figure 3.14 shows the setup of the desktop micro-CT scanner at Imperial College. The desktop scanner uses an industrial tube to generate a bundle of X-rays as a cone beam. The sample has to be imaged at least every half degree and rotated 360 degrees during the scan for a comprehensive set of radiographic profiles for the reconstruction.

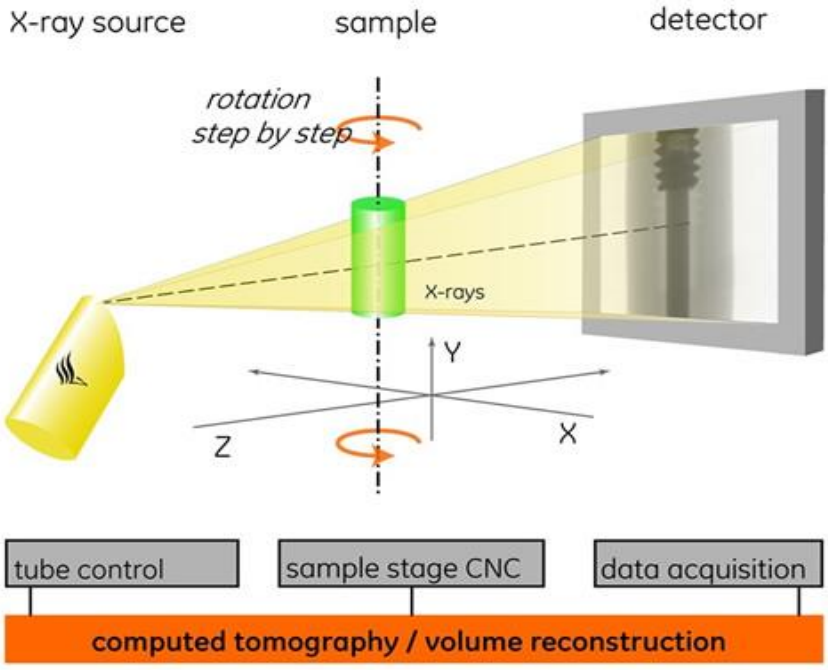

Figure 3.14: Schematic picture of basic components of a micro-CT scanner from the manual of the v|tome|x system. The system uses X-rays to penetrate sample that is rotated during the scanning and project the X-ray attenuation profiles on the detector from different viewpoints. These attenuation profiles are used for reconstructing 3-D image of the interior volume of the sample.

3.7.2 X-ray Attenuation

As the X-ray radiation from the source pass through the object being scanned, the signal is attenuated by scattering and absorption depending on the material composition, density and thickness along the beam direction. The attenuation of X-rays through a homogenous material can be calculated using Beer's law (Kak and Slaney, 2001). The simplest form of Beer's Law for a monochromatic X-ray beam through a homogeneous material is:

$$I = I_0 exp[-\mu x] \tag{3.7}$$

where I_0 and I are the initial and final X-ray intensity, μ is the material's linear attenuation coefficient (units 1/length) and x is the length of the X-ray path through the object. If the scan object is composite material, the equation becomes:

$$I = I_0 exp\left[\sum_i (-\mu_i x_i)\right] \tag{3.8}$$

where each increment i reflects a single material with attenuation coefficient μ_i over a linear extent x_i.

Taking into account that the attenuation coefficient is a strong function of X-ray energy, the complete solution would require solving equation (3.8) over the range of the effective X-ray spectrum:

$$I = \int I_o(E)\, exp\left[\sum_i (-\mu_i(E) x_i)\right] dE \tag{3.9}$$

The attenuated X-ray intensities (radiography) are received by the detector and transferred to the computer where the volume is reconstructed using 2-D projections. Figure 3.15 gives an example of an attenuation profile.

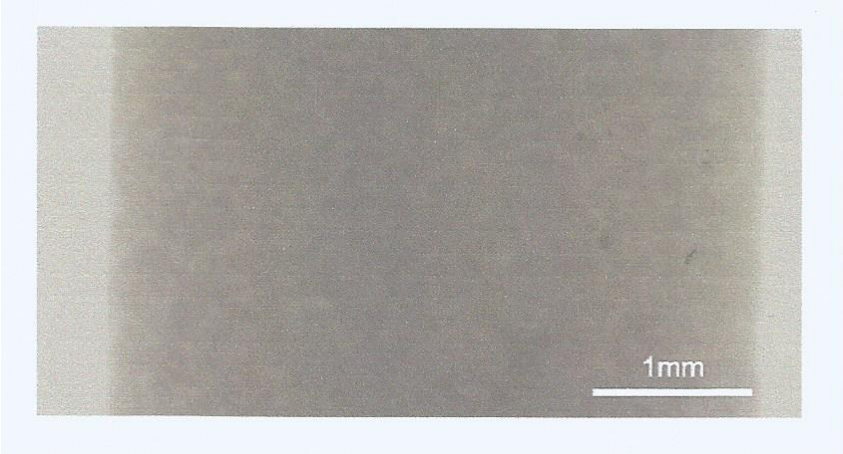

Figure 3.15: A profile of attenuated X-ray radiation through
a sandstone captured by the detector (Dong, 2007)

3.7.3 X-ray Sources

The laboratory desktop scanner uses an industrial X-ray generation tube (Figure 3.16a). The electrons emitted from a cathode by thermionic emission are accelerated by high voltage in order to collide with the target metal anode. During the impinging, X-ray photons are emitted due to two atomic processes: Bremsstrahlung and characteristic photon emission.

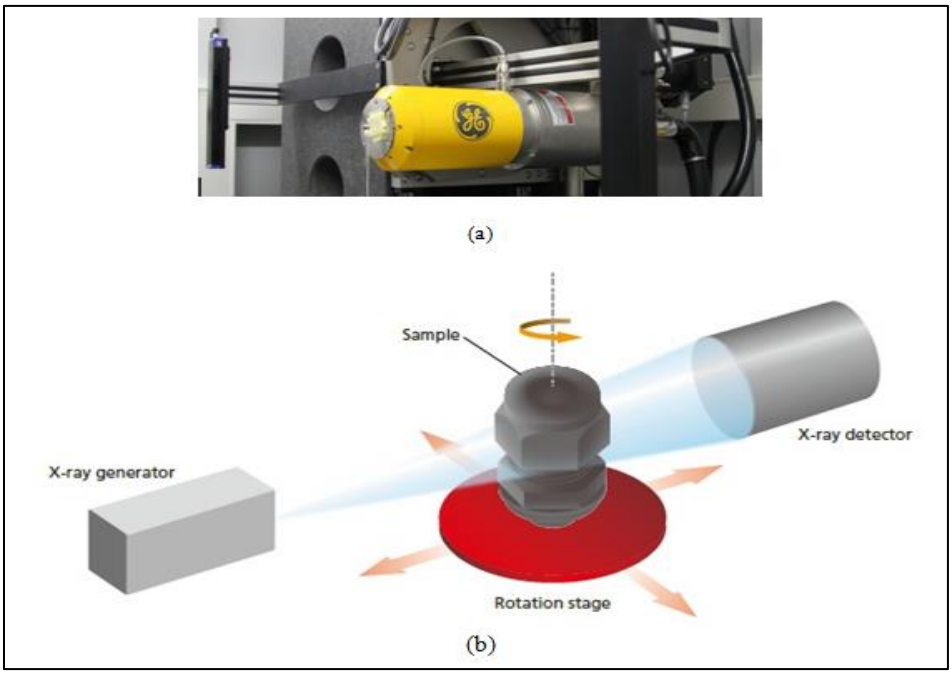

Figure 3.16: (a) The X-ray tube in the desktop scanner. (b) Rotating sample stage

Bremsstrahlung (German, "braking radiation" or "deceleration radiation") generates the continuous spectrum of X-ray photons, whose maximum energy is equivalent to the kinetic energy of the incident electrons decelerated at the anode. Characteristic photon emission generates certain spectral lines depending on the target anode element used. When an incident electron interacts with an atom, it may impart sufficient energy to an electron at lower energy shell and knock it out of the original energy status. An electron from a higher energy shell drops into the hole and emits a characteristic photon depending on the energy level difference in this process. The important variables that determine how effective an X-ray source will be for a particular task are the size of the focal spot, the spectrum of X-ray energies generated, and the X-ray intensity. The focal-spot size partially defines the potential spatial resolution of a CT system by determining the number of possible source-detector paths that can intersect a given point in the object being scanned. The more such source-detector paths there are, the more blurring of features there will be. The energy spectrum defines the penetrative ability of the X-rays, as well as their expected relative attenuation as they pass through materials of different density. Higher-energy X-rays penetrate more effectively than lower-energy ones, but are less sensitive to changes in material density and composition. The X-ray intensity directly affects the signal-to-noise ratio and thus image clarity. Higher intensities improve the underlying counting statistics, but often require a larger focal spot.

3.7.4 3D Reconstruction

The attenuation profiles are continuously measured and collected from different angles of view. Each view represents a rotational interval equal to 360 degrees (or 180 degrees with a parallel beam) divided by the total number of views.

Reconstruction is a mathematical process of converting attenuation profiles into a volume as serial two-dimensional slice images. The most widespread reconstruction technique is called filtered back-projection. For each projection, an intensity map is recorded in the XY detector plane. The projections are submitted to filtering procedures. In the filtration process, horizontal projection profiles are ramp-filtered in the Fourier domain after zero padding. In the back-projection process, an image volume is reconstructed by back-projecting filtered data along X-ray paths with appropriate weights. The weights are the beam length considering the different paths of the rays through the object.

3.7.5 Spatial Resolution

A pore space image is acquired in order to extract a topologically equivalent network with the pore space replaced by pores and throats. The imaging process should therefore identify the boundary of the solid phase and void phase and recognize the smallest crevices. Spatial resolution is very important parameter in achieving these aims as the contrast is relatively good between the void and solid for porous rocks. The image spatial resolution is the ability to distinguish high contrast phases (void and solid) that are close to each other. Practically, we require the resolution of 15~20 microns for coarse sandstone, 5~15 microns for unconsolidated sandstone and <5 microns for consolidated sandstone and most carbonates.

3.8 Sample Preparation

To obtain a high quality image from the scanner for subsequent data analysis, sample preparation is very important to achieve designed scan results. The preparation procedures must satisfy particle sampling statistics and not affect the mass linear attenuation coefficient of the sample itself. In consideration of the detector coverage during the sample rotation and the relation

between sample size and resolution, the mounted specimen must be small and well-shaped to obtain the maximum use of the detector to acquire the highest possible resolution. We drill small cylinders out of larger core samples and align them vertically onto the sample stage for best resolution acquisition.

Particle size and range are the two main issues for consideration in the preparation of the sample. The minimum particle size is required to be at least five to ten times of the voxel resolution in order to obtain enough voxels to distinguish the particle. A narrow size range is also helpful to get an unambiguous result. In this regard, a uniform particle size is preferred, especially for subsequent data analysis such as particle segmentation and mineral grain characterization.

The main purpose of the sample holder/container is to hold the sample on the stage in a fixed, steady position during scanning of the sample. The first consideration for the container is to stabilize the sample during the scan while rotating through different angles; the second consideration is the mass attenuation coefficient of the container which has to be as low as possible, yet still providing sufficient support and stability for the sample.

3.9 Experimental Procedure

The core sample was made into the specimens in size that fit into the sample holder. Figure (3.17) shows a schematic diagram of the experimental setup. After the initial preparation and calibration procedures required by the CT scan equipment were completed, the loading cell with sample was placed on the vertical rotating stage/turntable, the isolation room doors were closed and the scanning commenced. X-rays were generated at 90kV and 100 μA. During every loading

step, various sections of the core sample were scanned. The voxel size is approximately 512 µm x 512 µm × 400 µm.

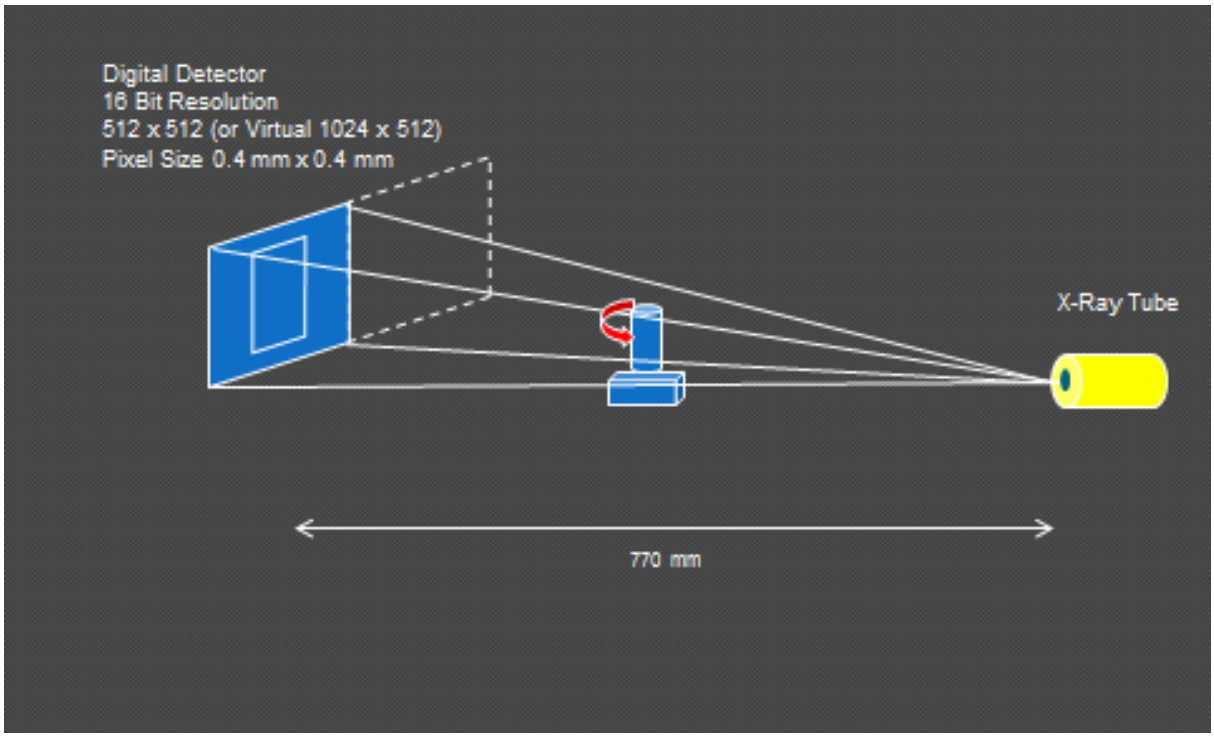

Figure 3.17: Schematic diagram of core scanning experimental setup

3.9.1 Image Acquisition

A brief summary of the parameters undertaken to obtain raw X-ray attenuation profiles using Phoenix v|tome|x system provided by the XMT lab at Imperial is given below.

3.9.1.1 Sample Positioning

Figure 3.16b shows the sample rotating stage. The specimen is positioned using the control panel of the system so that the specimen fills the field of view as fully as possible, while retaining a band of clear air to the left and right of the specimen throughout the rotation. Quick scans are

taken for every 45^{o} to make sure the edges of the specimen are more than 20-25 pixels from the edge of the detector at each view.

3.9.1.2 Sensor Calibration

First, the energy of X-ray has to be decided by tuning the voltage. A value of 90kV is sufficient to penetrate the minerals and make good contrast between void and solid. The resultant current is around 100μA. The correction images have to be acquired to remove inhomogeneity in the background images i.e. images with only air between source and detector. Two such images are required, one with the X-rays on and one with the X-rays off (also called flat and dark field in Synchrotron micro-CT). The flat field is necessary to account for the non-uniformities in the X-ray beam and the non-uniform response of the detector.

3.9.1.3 Operational Parameters

Parameters such as the number of images to average for one projection image, the metal thickness to reduce the beam hardening effects (for desktop μCT which uses polychromatic beam) etc. are defined for the scanning operation. One important factor affecting the image quality is the number of projections which should be similar to or greater than the width of the object in pixel.

3.9.1.4 Reconstruction

The software SIXTOS is used in the XMT lab at Imperial College London for reconstruction. A calibration factor (also called ‘Dejust’ or ‘Djust’) is found in this step by visual inspection to compensate for any difference between the center of the specimen and the center of the reconstruction.

3.10 Post-Processing

Mirco-CT outputs a 3D image which is a 3D array of gray scales. In order to obtain the pore space to quantitatively define the pore geometry and topology, the gray scales must be segmented into black and white representing the void and solid. Filters must be applied to the images to enhance the contrast of different materials and remove the noise.

3.10.1 Median Filter

As a cornerstone of modern image processing, the median filter is used extensively in smoothing and to remove noise. The idea of a median filter is to replace the gray scale value of a voxel by the median value of the nearest 26 surrounding cells. We apply median filter to the gray scales to despeckle the image without introducing new gray values into the scale.

In Figure 3.18, the effects of median filtering are demonstrated by applying to a sandstone image. The image resolution is 8.0 μm. (a) is a cross section of the original micro-CT image of the sample. After segmentation, the noises in the raw image become small grain voxels in the void or the holes in grains shown in (c). (b) is the effects of being smoothed by using a median filter and (d) is the binarized black-and-white image. Comparing (c) and (d), we find the median filter preserves the integrity of the grains and the pore space.

3.10.2 Image Segmentation

In order to obtain the pore space from the matrix, a segmentation process is required to binarize the gray scale into two scales, black (void) and white (solid), based on the gray scale histogram, shown in Figure (3.19). The bimodal histogram suggests that the image contains two peaks

representing the void and solid respectively. A threshold value is chosen at the valley to divide the image into two phases. We use the function of threshold provided in ImageJ.

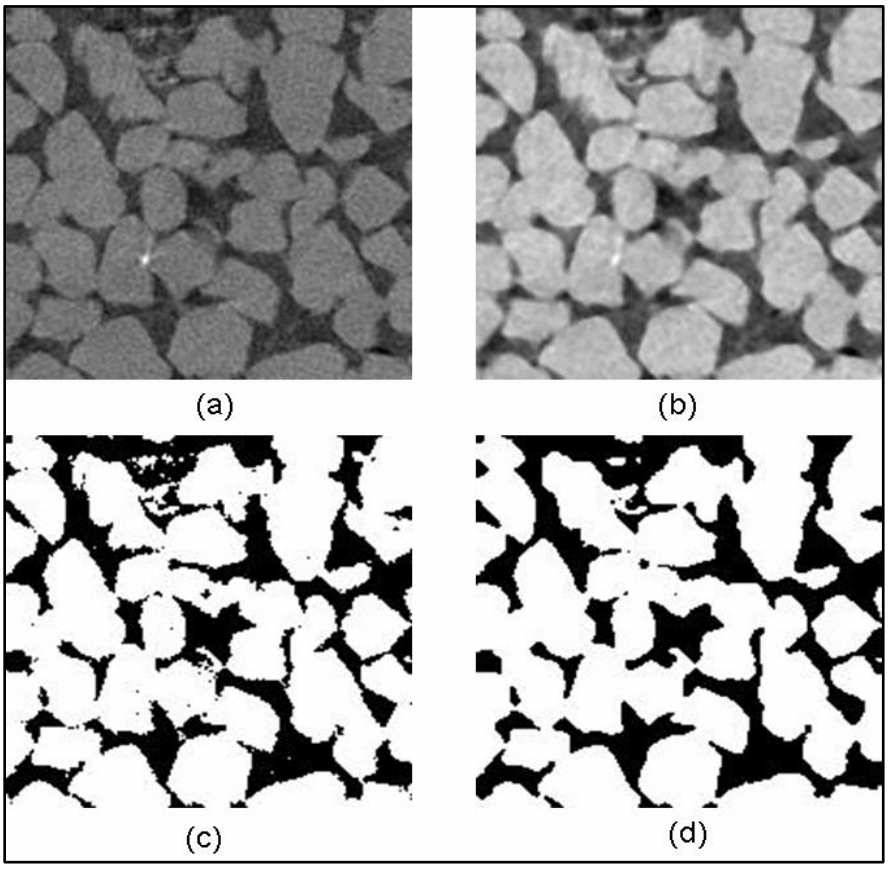

Figure 3.18: (a) A cross section of the raw image of a sandstone; (b) is the median filtered image of (a); (c) is the segmented image of (a); (d) is the segmented image of (b). The side length of the four cross section images is 0.75mm.

An automatic thresholding integrated in ImageJ is applied to select the thresholding value, which is an iterative procedure based on the isodata algorithm (Ridler and Calvard, 1978). Briefly, the isodata algorithm divides the image into objects and background by taking an initial threshold; then the averages of the pixels at or below the threshold and pixels above are computed. The averages of those two values are computed, the threshold is incremented and the process is repeated until the threshold is larger than the composite average, which is given by:

$$threshold - (average\ background + average\ objects)^2$$

If the automatic thresholding is not satisfied by visual inspection, a minor adjustment is performed to minimize the unreal grain voxels in the void and the holes in the grains.

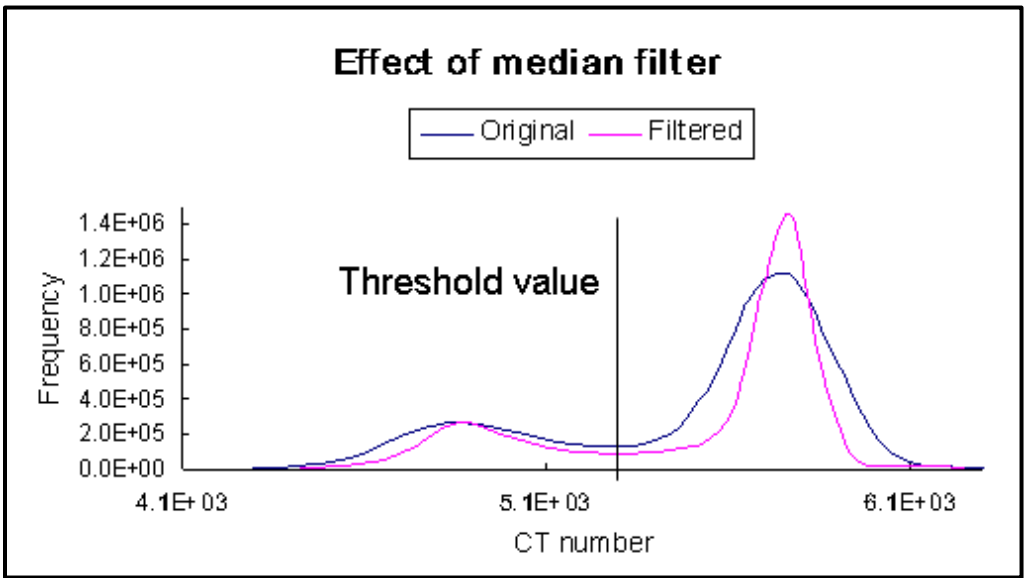

Figure 3.19: Effect of median filtering on the binarized images. The two peaks representing two phases (void and solid) are more distinguished after the filtering (Dong, 2007).

3.11 Network Extraction

The pore networks extraction from generic 3-D images using the maximal ball algorithm can be found in (Dong and Blunt, 2009).

Usually, it is difficult to measure the material's attenuation coefficient directly, and CT number is used to quantitatively describe the attenuation. With reference to a certain proportion, the CT number can be converted into grey value, which is shown as CT image. The material linear attenuation coefficient has approximate linear relationship with the density of the material, so CT image approximately reflects the changes of material density in the experiment, the CT image is 16- bit grey image, and the image size is 512 × 512 (pixels).

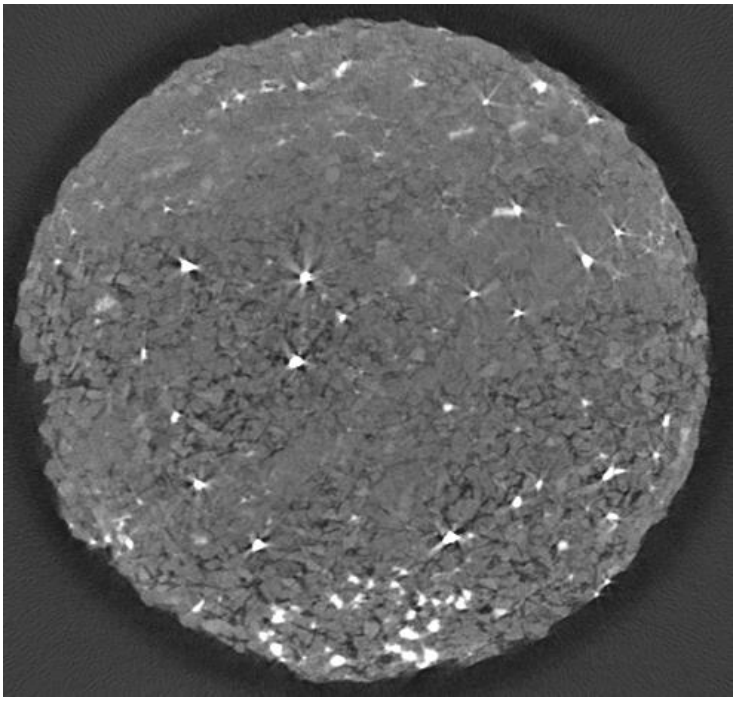

Figure 3.20: Imaged Agbada core sample. Image size by pixels (voxels) 512 x 512 x 400 mm. Resolution 8 microns. Actual image size 4.1 x 4.1 x 3.2 mm^3

3.12 Porosity Calculation

The x-ray 2-D images of the sample slices were exported to a computer and ImageJ software (http://rsbweb.nih.gov/ij/) was used to quantify the results. The scans were segmented to obtain similar sized rectangular region of interest from the middle part of the sample to eliminate possible artifacts (Babin et al., 2007).

ImageJ is a public domain Java-based image processing and analysis program. It runs, either as an online applet or as a downloadable application, on any computer with a Java 1.5 or later virtual machine. It can display, edit, analyze, process, save and print 8– bit, 16–bit and 32–bit images as well as accept multiple image formats as input, including TIFF, GIF, JPEG, BMP, DICOM, FITS and 'raw'. It also supports importation of image stacks as a single input. It is a multithreaded application, which means it takes advantage of multi-core processor architecture in

order to run multiple processes at the same time, something important in the processing and analysis of image stacks as regards time-efficiency. One important feature of ImageJ is that, apart from the basic suite of processes which covers most of the standardized processing and analysis operations, it allows for inclusion of custom scripts towards either automating existing processes or adding new ones. A very active multidisciplinary community continuously adds and updates publicly available content. In this work, ImageJ was used in further filtering and processing of the μ-CT images, as well as in determining the total porosity from the ratio of the number of foreground (air) voxels divided by the total number of voxels in the image using ImageJ.

3.13 Permeability Estimation - lattice Boltzmann Method

In this work, the lattice Boltzmann method (LBM) is used to simulate single-phase flow for the absolute permeability of the core samples. Known for its ability to handle complex geometries (boundary conditions), LBM, compared to traditional Computational fluid dynamics (CFD), models the fluid as consisting of fictitious particles performing consecutive propagation and collision processes on the discrete lattice mesh (voxel grids) rather than solving numerically for the conservation equations of mass and momentum without solving the Navier-Stokes equation directly at the continuum level (Succi, 2001).

Instead of solving the Navier-Stokes equations to calculate the absolute permeability, the discrete Boltzmann equation is solved to simulate the flow of Newtonian fluid with collision models (Chen and Doolen, 1998; Manswart et al., 2002). In other words, the LBM captures the essential

physics at the micro- or meso-scopic scale in order to satisfy the macroscopic dynamics from the averaged particles behavior (Okabe, 2004).

The Boltzmann equation is discretized by limiting the space to a lattice and the velocity space to a discrete set of velocities $\overrightarrow{e_i}$, therefore the lattice Boltzmann equation is:

$$f_i(\vec{x} + \overrightarrow{e_i}, t+1) - f_i(\vec{x}, t) = \Omega_i\big(f_i(\overrightarrow{x}, t)\big) \tag{3.10}$$

where $f_i(\vec{x}, t)$ is the particle distribution function at position $\vec{x}$ and time t along the i-th direction (i = 0,1,2…18) using three-dimensional nineteen velocity (D3Q19) model (Qian et al., 1992) which considers three velocity types. $\Omega_i\big(f_i(\vec{x}, t)\big)$ is the collision operator and $\overrightarrow{e_i}$ is the local particle velocity.

The collision operator represents the relaxation process to local equilibrium, which is often approximated by a BGK collision operator (Bhatnagar et al., 1954) and widely used due to its simplicity (Qian et al., 1992).

$$\Omega_i = \frac{1}{\tau}\big(f_i^{eqv} - f_i\big) \tag{3.11}$$

where τ is the single time relaxation parameter and f_i^{eqv} is the local equilibrium state depending on the density ρ and local velocity u. The conserved quantities are the mass and momentum defined below:

$$\rho = \sum_i f_i = \sum_i f_i^{eqv} \tag{3.12}$$

$$\rho\vec{u} = \sum_i f_i\,\overrightarrow{e_i} = \sum_i f_i^{eqv} \tag{3.13}$$

where ρ and u are the density and the local velocity respectively.

Thus, the LB model for 3-D single-phase is

$$f_i(\vec{x} + \vec{e}_1, t + 1) - f_i(\vec{x}, t) = \frac{1}{\tau}\left(f_i^{eqv} - f_i\right) \tag{3.14}$$

3.14 Measurement of saturations and capillary pressure

The percentage saturation of the tested samples was measured by recording the dry weight of the samples, loading the samples in a saturator, evacuating air from the saturator for 30 minutes using vacuum pump; filling the saturator with the saturating fluid (brine or crude oil) at a pressure of 1000 psi for 24 hours, and then recording thereafter the net weight of the samples. The saturation values are then obtained by the equation:

$$S_i = \frac{Volume\ of\ phase}{Pore\ volume} = \frac{V_i}{V_p} \tag{3.15}$$

The porous plate method was used for the laboratory measurement of capillary pressure. A set of capillary pressure data was acquired under different wettability conditions (before and after wettability alteration of the core samples by aging) for both water-wet and oil-wet conditions.

Relative permeability was calculated using the Brooks-Corey-Burdine empirical relationship (Jerauld and Salter, 1990; Valvatne and Blunt, 2004):

$$k_{rw} = S_{ew}^4,$$

$$k_{rnw} = (1 - S_{ew})^2(1 - S_{ew}^2), \tag{3.16}$$

$$S_{ew} = \frac{S_w - S_{rw}}{1 - S_{rw}}$$

where

k_{rw} and k_{rnw} are the wetting phase and non-wetting phase relative permeability, respectively; S_{ew}, Srw, and Sw are the effective saturation of the wetting phase, residual saturation of the wetting phase, and the saturation of the wetting phase, respectively.

3.15 Buckley-Leverret computation of waterflood oil recovery

3.15.1 Immiscible displacement process of oil by water

A mathematical approach to describe the flow of two-phase immiscible fluids in a linear system was developed by Buckley and Leverett (1942). By applying the law of conservation of mass they developed a fundamental theory that governs flow of two fluids in one dimension. The frontal advance theory states that in a representative elementary volume (REV) of length *dx* of a porous medium mass is conserved. This mass conservation of fluid passing through the REV is stated as:

rate of mass accumulation within the element = rate of mass transport in – rate of mass transport out

The details of the mathematical development of Buckley-Leverett frontal theory are not discussed in this study as they can be found in any petroleum engineering literature. Instead its practical application to waterflooding in the Agbada reservoir is considered.

The important assumptions made in the Buckley-Leverett theory include the following:

1. At the flood front, only oil moves ahead of the front while oil and water move behind the front.
2. The cross-sectional area to flow is constant
3. The core is a single homogenous layer (constant φ and k).

4. Flow is linear and steady-state (Darcy's law).
5. Gas saturation in front of the fluid is zero at all times.
6. Fluids are incompressible
7. Capillary pressure and gravity effects are negligible.

In this study a core plug saturated with both oil and water is considered. At the transition zone during the coreflooding both oil and water will be produced, and at each point water fraction flowrate will be a function of oil and water saturation at that point. The intersection of the tangent to the fractional-flow water saturation curve, f_w vs. S_w is used to calculate the average water saturation after breakthrough. We note however, that this technique is subject to errors, as it is difficult to ascertain the exact point at which the tangent to the fractional-flow curve intersects the curve. We assume oil displacement to be a diffusion flow process and that the conditions for vertical equilibrium do not exist. Capillary pressure and gravity effects are negligible. The equations for simultaneous flow of oil and water are:

for oil,

$$q_o = \frac{k_o k A \rho_o}{\mu_o} \frac{dp}{dx} \tag{3.17}$$

and for water

$$q_w = \frac{k_w k \rho_w A}{\mu_w} \frac{dp}{dx} \tag{3.18}$$

Total flow rate through the small volume element is given as:

$$q_t = q_o + q_w \tag{3.19}$$

Fractional water and oil flows in the reservoir (core) are given by:

$$f_w = \frac{q_w}{q_w + q_o} = \frac{q_w}{q_t} \tag{3.20}$$

and

$$f_o = 1 - f_w \tag{3.21}$$

where q denotes volumetric flow rate at reservoir conditions and the sub-scripts $\{o,w,t\}$ refer to oil, water, and total rate, respectively and f_w and f_o are fractional flow to water and oil (or water cut and oil cut), respectively.

For horizontal flow and neglecting capillary pressure gradient, equation (3.20) becomes:

$$f_w = \frac{\frac{k_{rw}}{\mu_w}}{\frac{k_{ro}}{\mu_o}+\frac{k_{rw}}{\mu_w}} = \frac{1}{1+\frac{k_{ro}\mu_w}{k_{rw}\mu_o}} \tag{3.22}$$

where k_o/k_w and by extension f_w, are functions of saturation.

The following procedures adopted in this work are valid for water injection with initial oil production and equally for the case when the oil originally in place (OIIP) has been reduced by a primary production factor: 1) Calculate and plot the water saturation profile; 2) Calculate time to water breakthrough; 3) Calculate cumulative water injected at breakthrough; 4) Water volume injected at breakthrough. In this work, a single homogeneous layer reservoir (core plug) with constant porosity and permeability respectively, is considered.

3.16 Simulation of waterflooding in Agbada sandstone reservoir

In this section a model for the simulation of waterflooding in the Agbada sandstone formation is proposed. The proposed model is based on the use of Weierstrass elliptic functions, in particular, the *P*-functions.

3.16.1 Weierstrass elliptic functions

As stated in Chapter 2, the Weierstrass elliptic functions (or Weierstrass *P*-functions) are elliptic functions which have a second-order poles at all nodes of the periodic lattice. The main function is the *P*-function, defined by the infinite sum:

$$P(z) = \frac{1}{z^2} = \sum_{m,n=-\infty}{}' \left(\frac{1}{(z-\omega)^2} - \frac{1}{\omega^2} \right) \tag{3.23}$$

where $\omega = m\omega$, nω (m, n 0, 1, 2) are the nodes of the periodic lattice Λ.

The prime in equation (3.23) indicates that the summation is taken over all non-zero periods of *P*, i.e., over all integer values of *m* and *n*, except when $m = n = 0$. The subtraction of each $1/\omega^2$ plays two roles: it gives convergence of the series, and the right limiting behavior as *z* approaches zero.

The main property of the p-function that is of interest in this work is its double periodicity. As stated earlier, function *f*(z) is generally denoted by *P*(z). Therefore,

$$\left.\begin{aligned} P(z-\omega_1) &= P(z) \\ P(z-\omega_2) &= P(z) \end{aligned}\right\} \tag{3.24}$$

where ω_1 and ω_2 are the periods of the Weierstrass *P*-function.

3.16.2 Mathematical model

One application of complex analysis is to fluid dynamics. In particular, potential flow (steady, two-dimensional, inviscid, incompressible) may be studied with the aid of analytic complex functions. Here it will be shown how the elliptic functions discussed in this paper may be used to simulate potential flow in a rectangular closed reservoir model.

Reservoir simulation boundary condition requires that the reservoir lies within a closed space across which there is no flow: fluid injection and withdrawal take place in system of wells which can be represented by point sources and sinks and regarded as doubly periodic array of injection and production wells. The mathematical models that are used for the description of fluid flow in oil reservoirs can be divided into compressible or incompressible, and miscible or immiscible flow. The models that describe most isothermal flow conditions are derived from four main physical principles. These are mass conservation, momentum conservation, thermodynamic equilibrium, and full saturation of the rock pore volume by the fluid. Application of available analytical models is restricted to small models, due to the complexity and mathematical efforts required in most of the practical applications. So the solution for intermediate and large models is the numerical simulation. Different methods are used in oil reservoir simulation. In this work the Weierstrass elliptic functions method is used for solution of the differential equations of flow in the Agbada sandstone rock medium. The mathematical formulations used in this section rely heavily on the work of Astafev and Roters, (2014), and Astafev and Kasatkin, (2016).

The flow of a fluid of slight and constant compressibility, c_t, through a closed isotropic porous medium of volume $V = Ah$ is described by Darcy's law:

$$\frac{\varphi}{\rho}\frac{\partial \rho}{\partial t} + \frac{\partial v_x}{\partial x} + \frac{\partial v_y}{\partial y} = 0 \tag{3.25}$$

$$v_x = -\frac{k}{\mu}\frac{\partial p}{\partial x}, v_y = -\frac{k}{\mu}\frac{\partial p}{\partial y} \tag{3.26}$$

where ρ is the density of the fluid, μ is the viscosity, k is the permeability, φ is the porosity, p is the reservoir pressure, v_x and v_y are the Darcy velocity components, A (denoted by Δ in the fundamental parallelogram) and h are the square and thickness (area and height) of the reservoir, respectively.

For quasi-static flow the governing equation for pressure in the reservoir $p(x, y, t)$ can be expressed by the diffusion equation:

$$\frac{\partial P}{\partial t} = C_D \left(\frac{\partial^2 P}{\partial x^2} + \frac{\partial^2 P}{\partial y^2}\right) \tag{3.27}$$

where C_D is the diffusion coefficient, given as:

$$C_D = \frac{k}{\varphi \mu c_t}$$

The average pressure in the reservoir can be expressed as the form $P(x, y, t) = \bar{P}(t)\delta p(x, y)$, or

$$\frac{\partial P}{\partial t} = \frac{d\bar{P}}{dt}$$

where $\bar{P}(t) = \frac{1}{A}\iint P(x, y, t)dxdy$ is the average reservoir pressure.

We can therefore rewrite the first term of the right hand side of equation (3.25) above as:

$$\frac{\varphi}{\rho}\frac{\partial \rho}{\partial P}\frac{d\bar{P}}{dt} = \varphi C_p \frac{d\bar{P}}{dt}$$

where $C_p = \frac{1}{\rho}\frac{\partial \rho}{\partial P}$ = constant, is the compressibility factor or coefficient.

For a well in a closed reservoir of volume $V = Ah$ producing at a rate q, the material balance can be expressed as:

$$\varphi C_p \frac{d\bar{P}}{dt} = \frac{q}{Ah} \tag{3.27}$$

A combination of the material balance equation (3.27) above, and the continuity equation (3.25) written in the form

$$\frac{\partial v_x}{\partial x} + \frac{\partial v_y}{\partial y} = \frac{q}{Ah} \tag{3.28}$$

with the Darcy equations for velocity components (equation 3.26) gives a system of equations for the unknown functions $\delta P(x, y), \bar{P}(t), v_x \; and \; v_y$, which describe quasi-static flow in the closed reservoir.

To obtain a general solution to equations (3.26) - (3.28) we impose the complex variables and their conjugates variables of $z = x + iy$ and $\bar{z} = x + iy$ on the coordinates x and y, and the complex velocity function and its conjugate $V = v_x + iv_y$ and $\bar{V} = v_x + iv_y$ on the velocity component vectors $v_x \; and \; v_y$. With these equations (3.26) - (3.28) become:

$$\left.\begin{aligned} V &= -\frac{2k}{\mu}\frac{\partial P}{\partial z} \\ \bar{V} &= \frac{2k}{\mu}\frac{\partial P}{\partial z} \end{aligned}\right\} \tag{3.29}$$

$$\frac{\partial V}{\partial z} + \frac{\partial \bar{V}}{\partial z} = \frac{q}{Ah} \tag{3.30}$$

With equations (3.29) and (3.30) we can re-write the complex velocity function $V = (z, \bar{z})$ and the pressure function $P(z, \bar{z})$ in the following forms:

$$V = \frac{q}{2Ah} z + \overline{F'(z)}, \quad \bar{V} = \frac{q}{2Ah}\bar{z} + F'(\bar{z}) \tag{3.31}$$

$$P = \frac{\mu}{2k}\left(F(z) - \overline{F(z)} - \frac{q}{2Ah} z\bar{z} + C\right) \tag{3.32}$$

where $F(z)$ is an unknown analytical function and C is an arbitrary constant.

3.16.3 Boundary conditions

It is essential that, in order to complete the mathematical model and initiate the solution of the simulation model, all initial and boundary conditions be specified. Initial boundaries include external and internal boundaries. External boundaries are the physical domains beyond which there is no flow, while the internal boundaries maybe the flow rates of the phases or the bottomhole pressure. Initial conditions are the initial reservoir pressure and the distribution of the

saturations of the phases. In this work, a no-flow (or closed boundary) is assumed as external boundary condition, that is, there is no-flow of any phase (oil or water) across the external boundary of the reservoir model. In other words, the component of velocity perpendicular to the external boundary is zero, i. e.,

$$(v_n|_\Gamma = 0) \tag{3.33}$$

Since the flow path is bounded by solid walls, the usual no-slip boundary conditions apply. Flow in the reservoir is driven only by a constant pressure gradient, no external body force. Pressure of the gridblock or well contour is equal to the flowing wellbore pressure, i. e.,

$$P|_{z=r_{w}e^{i\theta}} = P_{wf} \tag{3.34}$$

Fluid flow rate on the gridblock or well contour of radius r_w is equal to the flow rate in the reservoir, i. e,

$$h\int_0^{2\pi} v_n r_w d\theta = -q \tag{3.35}$$

The equation for the component of velocity perpendicular to the external boundary can be written as:

$$v_n ds = Im(\bar{V} dz)$$

where $z = z(s)$ is the reservoir boundary equation, n is the unit normal to Γ

To find $F(z)$ and C, we impose the boundary conditions stated above. Applying the boundary conditions in equations (3.34) and (3.35), and assuming that the ratio of the wellbore area to the area of the reservoir is small and negligible, the unknown function $F(z)$ and the constant C can be expressed as:

$$F(z)=\frac{q}{2\pi h}\left(lnz - F_o(z)\right); \qquad F_o(z) = \sum_{n=1}^{\infty} \alpha_n z^n \tag{3.36}$$

$$C = \frac{2k}{\mu} P_{wf} - \frac{q}{2\pi h} ln r_w^2 \tag{3.37}$$

Therefore, for a well flowing at a rate q and centered in a closed reservoir of drainage area Ah, boundary Γ, and origin $z = 0$,

$$\bar{V} = \frac{q}{2\pi h}\left(\frac{1}{z} + F_o(z) - \frac{\pi}{A}\bar{z}\right) \tag{3.38}$$

$$P = P_{wf} + \frac{q\mu}{4\pi kh}\left(ln\frac{z\bar{z}}{r_w^2} + F_o(z) - \overline{F_o(z)} - \frac{\pi}{A} z\bar{z}\right) \tag{3.39}$$

In the above equation, $F_o(z)$ is an unknown analytical function which can be determined by applying the no-flow boundary condition. For the reservoir boundary z = z(s),

$$ImF_o(s) = \frac{2\pi}{A}\sum(s) - \theta(s) \tag{3.40}$$

where s is the length of an arc of a point on the reservoir boundary, $\theta(s)$ is the polar angle of the point, P, and $\sum(s)$ is the square of the sector sustaining the arc. Methods of solving the above equation for different types of reservoir boundaries can be found in Gakhov (1966).

We consider flow in a closed cylindrical reservoir with the boundary Γ, and a producing well of radius r_w at the center, shown in Figure 3.20. We transform this flowfield into a parallelogram using the map given by equation 2.19 and impose the complex variables and their conjugates to simulate flow in the system.

Based on the transformation we regard the injection and production wells as periodic arrays of wells defined by their placement patterns, as on a fundamental parallelogram with a doubly periodic lattice spanned by the periods ω_1 and ω_2. Figure 3.22 shows the fundamental parallelogram with the corresponding periods for five-spot waterflooding pattern.

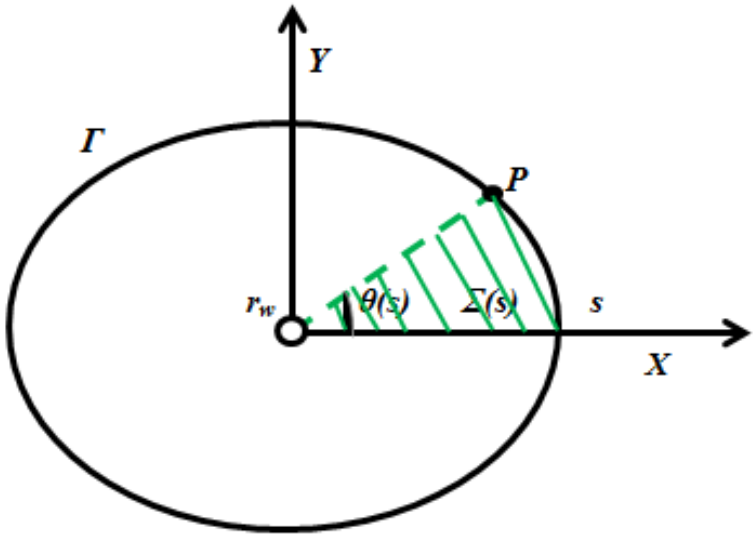

Fig. 3.21: Closed cylindrical reservoir with boundary Γ and a producing well of radius r_w

Double periodicity of the lattice is defined by a series of numerical parameters, shown in Figure 3.20, that determine the size and form of its periods. The corners $\omega = m\omega_1 + n\omega_2 / m, n \in \mathbb{Z}$ lattice are defined by the parameters ω_1, $\omega_2 = \infty = \lambda e^{i\theta}$, where θ is the angle between ω_2 and the *OX* axis.

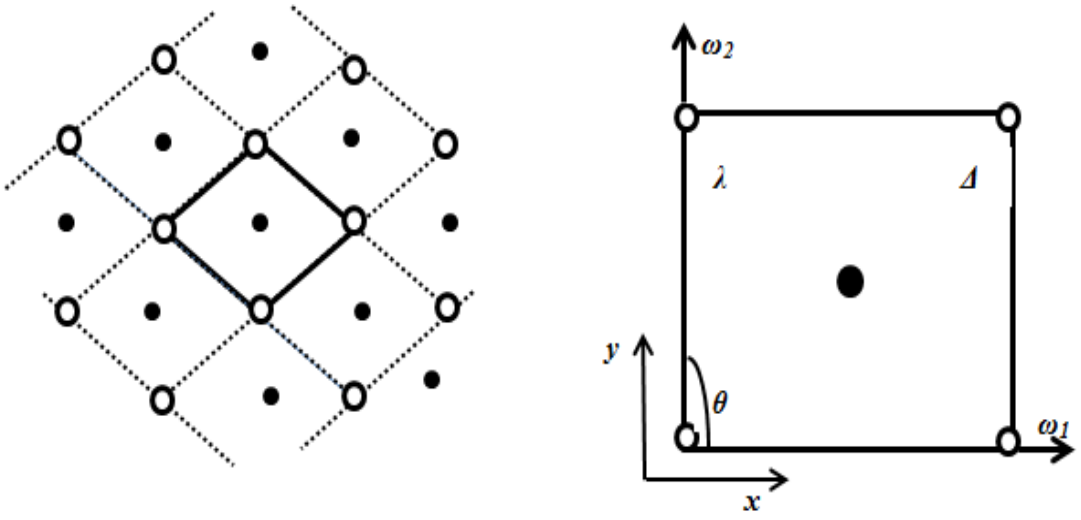

Fig 3.22: Double periodic lattice for five-spot water flooding pattern. Injection wells are shown by black circles while production wells are shown by dark shaded circles

3.16.4 Piston-like displacement

For piston-like displacement (moving boundary problem), the boundary condition at the moving oil-water boundary line for the normal V^n and tangential V^t velocity components, respectively can be expressed as:

$$\begin{cases} V_w^n = V_o^n \\ \mu_w V_w^t = \mu_o V_o^t \end{cases} \tag{3.41}$$

where μ_w and μ_o are the viscosities of water and oil, and the superscripts *w* and *o* denote the water phase and the oil phase, respectively.

We consider the position of a point $\mathbb{Z}$ on the oil-water boundary at a given time *t*, with the corresponding normal and tangential velocities shown in Figure 3.23. Here, the flood front (line L, shown in black) divides the flood region into zones occupied by water, injected through the injection well, and oil, respectively.

Next is to apply the complex variables $z = x + iy$ on the velocity function $\bar{V}(z) = V_x - iV_y$ for both oil and water at any chosen point $\mathbb{Z}$(x, y). Transforming to the coordinate system (*t*, *n*), we have:

$$\bar{V}(z) = V_t(cos\alpha - isin\alpha) + iV_n(cos\alpha - sin\alpha) = \big(V_t(z) + iV_n(z)\big)e^{-i\alpha} \tag{3.42}$$

The function $\bar{V}(z)$ will be sought for in the form:

$$\bar{V}(z) = V_x(x,y) - iV_y(x,y) = F(z) + \frac{1}{2\pi i}\oint_L \xi(\tau - z)\gamma(\tau,t)d\tau \tag{3.43a}$$

which can also be written in its variant form as:

$$\bar{V}(z,\bar{z}) = V_x(x,y) - iV_y(x,y) = -\sum_{k=1}^{n}\frac{q_k}{2\pi h}\big(\zeta(z - z_k) + \alpha(z - z_k) - c_t(\bar{z} - \bar{z}_k)\big) \tag{3.43b}$$

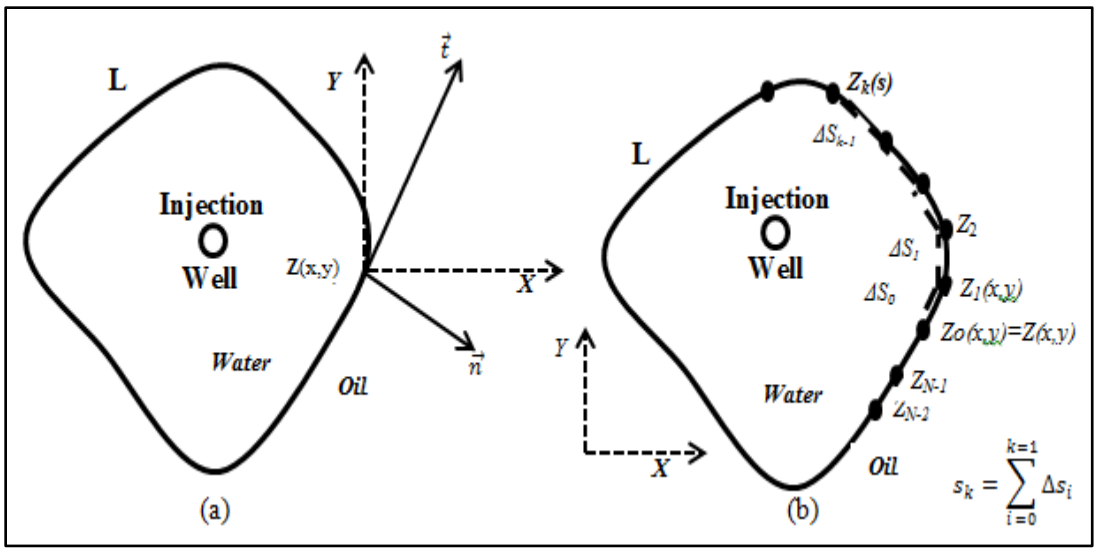

Fig. 3.23: Schematic diagrams of oil-water interface: – a) mutual position of the vectors (X, Y) and (t, n) related to the point (x, y) on the oil-water contact (OWC); b) parameterization of OWC contour.

The function $F(z)$ is a velocity function for doubly periodic scheme of waterflooding, and is given by the equation:

$$F(z) = -\sum_{u=1}^{n_1} \frac{q_{u_{prod}}}{2\pi h}\left(\zeta(z - z_u) + \alpha(z - z_u) - c_t(\overline{z - z_u})\right)$$

$$+\sum_{w=1}^{n_2} \frac{q_{w_{inj}}}{2\pi h}\left(\zeta(z - z_w) + \alpha(z - z_w) - c_t(\overline{z - z_w})\right)$$

where $\zeta(z)$ is the Weierstrass zeta function, z_k is the location of the k-th well in the cluster (z_u for production and z_w for injection wells, respectively), $\alpha = \left((c_t - \frac{2}{\omega 1})\zeta(\omega_1/2)\right)$, $c_t = \pi/A$ and q_k is the flow rate of the k-th well (q_u for production and q_w for injection wells, respectively). For injection well q_k of oil ≤ 0, while for production well $q_k > 0$ (source and sink).

The second of the right hand side of equation (3.43a) is a regular integral of Cauchy type nucleus, embodied in the Weierstrass zeta function $\zeta(\tau - z)$ for fulfillment of the condition for doubly periodicity (Koiter, 1959).

The pressure field in the reservoir with doubly periodic system of wells is defined by the following equation:

$$p = p_{wf} + \frac{q}{2\pi kh}\left[Re\left(ln\sigma(z) + \alpha\frac{z^2}{2}\right) - C_p\frac{z\bar{z}}{2} - lnr_w\right] \tag{3.44}$$

Once the pressure field is determined, the velocity field can be determined by using equations (3.43a, b). Therefore, equations (3.43a,b) are used to determine the oil and water velocity function (V_o(z) and V_w(z) on the oil-water contact line, L.

Parameterization of the contour L based on the length of the arc *s* (Figure 3.23b), and application of Sokhotsky-Plemel equation (Koiter, 1959) gives the following system of equations:

$$\begin{cases} V_w\big(z(s)\big) = F\big(z(s)\big) + \frac{1}{2\pi i}\oint_L \xi\big(\tau - z(s)\big)\gamma(\tau)d\tau + \frac{\gamma(z(s))}{2}; \\ V_o\big(z(s)\big) = F\big(z(s)\big) + \frac{1}{2\pi i}\oint_L \xi\big(\tau - z(s)\big)\gamma(\tau)d\tau - \frac{\gamma(z(s))}{2} \end{cases} \tag{3.45}$$

where z = z(s) and the integration variable τ, connected with the contour points, has the same meaning as the *z* inside the integral part of above equation (3.45).

Combination of equation (3.45) above with equation (3.41) results in the following function for $\gamma(z) = V_w(z) - V_o(z)$:

$$\gamma(z) = V_w^t(z)\left(1 - \frac{\mu_w}{\mu_o}\right)c^{-i\alpha} \tag{3.46}$$

The coinciding of the oil-water contact with the oil-water boundary line and the flood front is adequate to monitor the evolution of the oil water contact (streamlines) from the launch position. Also, further attention will be focused on the velocity field, which is which is expressed by the function$\bar{V}_w(z)$.

The ratio of the viscosities is denoted as $\mu_R = {}^{\mu_w}/_{\mu_o}$ while the corresponding normal and tangential velocities are denoted as $N(s) = V_w^n\big(z(s)\big)$ and $T(s) = V_w^t\big(z(s)\big)$. Further, we rewrite the form of the function $\bar{V}_w\big(z(s)\big)$ in equation (3.44) with new notations. Transforming *N*(s) and T(s) using equation (3.42) and changing the contour interval, and also taking into consideration equation (3.45), the following equation is obtained:

$$\frac{1+k}{2}T(s) + iN(s) = \left[F\big(z(s)\big) + \frac{1-k}{2\pi i}\int_0^S \xi\big(z(\sigma) - z(s)\big)T(\sigma)d\sigma\right]\frac{dz}{ds} \tag{3.47}$$

Here the variable σ is the parameter for the arc length s, while the integral limit *S* is calculated by the equation:

$$S = \sum_{i=0}^{N-1} \Delta s_i$$

This validates the relationship $z = z(s)$

Equation (3.47) allows us calculate the flow velocity of the injected water at a given point $z = z(s)$ on the oil-water boundary line. However, in order to find solution to the oil-water contact monitoring, it is necessary to track the flow path of the injected water in the reservoir, which is the next step.

Solution to the problem of tracking the OWC movement implies the monitoring the displacement or path of generated streamlines with time. For this, the system of equations below, which is analogues to the Cauchy problem, may be applied:

$$\left.\begin{aligned} \varphi\frac{\partial \bar{z}}{\partial t} &= \bar{V}(z) \\ z_{t=0} &= z_0 + r_w e^{i\theta} \end{aligned}\right\} \tag{3.48}$$

where φ is the porosity of the reservoir (as indicated earlier), z_o (the equivalent wellbore radius in complex variable) is the center of the injection well of radius r_w.

The reservoir simulator calculates pressures for each lattice or gridblock. In order to relate the wellblock pressure (pressure of the gridblock where well is located) to the flowing wellbore pressure, the concept of equivalent wellblock radius, z_o, is used. The most significant treatment of well models until the late 1980s was given by Peaceman (1978). This model is based on the assumption of steady state flow condition at the boundary of the drainage area of the reservoir. According to Peaceman the wellblock pressure, p_o, is related to the bottomhole flowing pressure, p_{wf}, for a vertical well by:

$$p_o - p_{wf} = \frac{q\mu}{2\pi\left(k_x + k_y\right)^{1/2}\Delta z} ln \frac{r_o}{r_w}$$

were r_w is the wellbore radius and r_o is the equivalent wellblock radius. The equivalent wellbore radius r_0 is the effective block radius at which the steady-state pressure equals the computed grid pressure, and for an isotropic system ($k_x = k_y$), it is given by (Peaceman, 1978):

$$r_o = 0.14(\Delta x^2 + \Delta y^2)^{1/2}$$

As stated earlier, $\bar{V}(z)$ loses continuity on the OWC due to piston-like displacement (viscosity difference). Because of this it is necessary to define the velocity function on the oil-water boundary. In this work, $\bar{V}(z)$ is taken as the total sum of all the values of the velocity of oil $\bar{V}_o(z)$ and velocity of water $\bar{V}_w(z)$. Considering the conditions in equation (3.41), expression for $\bar{V}(z)$ becomes:

$$\bar{V}(z) = \frac{1}{2}\left(\bar{V}_o(z) + \bar{V}_w(z)\right) = \left(\frac{(1+k)}{2}T(s) + iN(s)\right)e^{-i\alpha}$$

Rewriting equation (3.48) gives:

$$\left.\begin{array}{c} \varphi \frac{\partial \bar{z}}{\partial t} = \left[\frac{(1+k)}{2} T_w(s) + iN_w(s)\right] e^{-i\alpha} \\ z_{t=0} = z_0 + r_w e^{i\theta} \end{array}\right\} \tag{3.49a}$$

Further, a proper attention is given to equation (3.46), necessary for determination of the component function $\vec{V}(z)$. In contrast to first term, $F\big(z(s)\big)$, given analytically, the singular integral on the right side of equation (3.47) is computed approximately:

$$\int_0^S \xi\big(z(\sigma) - z(s_k)\big) T(\sigma) d\sigma = \sum_{i=k}^{N+k-1} \int_{s_i}^{s_i+1} \xi\big(z(\sigma) - z(s_k)\big) T(\sigma) d\sigma \tag{3.49b}$$

In line with definition, singular integral with nucleus the type of Cauchy, contains in itself a peculiarity expressed in the form $\frac{1}{z-z_k}$, which exhibits only two integrals, from the sum. Removing them into separate terms, we obtain singular and regular components of the singular integral, included in the right side of equation (3.46):

$$\left\{\begin{array}{c} \sum_{i-k}^{N+k-1} \int_{s_i}^{s_i+1} \xi\big(z(\sigma) - z(s_k)\big) T(\sigma) d\sigma = \int_{s_{k-1}}^{s_i+1} \xi\big(z(\sigma) - z(s_k)\big) T(\sigma) d\sigma \\ + \sum_{i=k+1}^{N+k-2} \int_{S_i}^{S_i+1} \xi\big(z(\sigma) - z(s_k)\big) T(\sigma) d\sigma \end{array}\right. \tag{3.50}$$

The first term in equation (3.50) is singular, arising from the signs of the limits of integration and definition of Weierstrass zeta function, appearing in the integral nucleus.

$$\xi\big(z(\sigma) - z(s)\big) = \frac{1}{z(\sigma) - z(s)} + \sum_{n,m=-\infty}^{\infty} \left(\frac{1}{z(\sigma) - z(s) - \omega} + \frac{1}{\omega}\right) + \frac{z(\sigma) - z(s)}{\omega^2}$$

where ω =, mω_{1+} $n\omega_2/m$, $n \in \mathbb{Z}$ is the region of doubly periodicity of the lattice, on which ξ is defined.

To establish its significance, the first term in equation (3.50) is solved on the basis of the Cauchy main problem. As a result the following equation is obtained:

$$\int_{s_{k-1}}^{s_i+1} \xi\big(z(\sigma)-z(s_k)\big)T(\sigma)d\sigma = \frac{1}{z'_k}\left[T_k ln\left(\frac{\Delta s_k}{\Delta s_{k-1}}\right)+T_{k+1}-T_{k-1}\right]+ \frac{1}{2}[\xi z_{k-1}-z_k)T_{k-1}\Delta s_{k-1}+\xi(z_{k+1}-z_k)T_{k+1}\Delta s_k]$$

The second term in equation (3.50) is regular, and is determined by squaring the sum according to the trapezoidal rule:

$$\sum_{i=k+1}^{N+k-1}\int_{s_i}^{s_i+1} \xi\big(z(\sigma)-z(s_k)\big)T(\sigma)d\sigma = \frac{1}{2}\sum_{i=k+1}^{N+k-2}[\xi(z_{k+1}-z_k)T_i+\xi(z_{i+1}-z_k)T_{i+1}]\Delta s_i$$

From the above relationship, a summation expression for determination of the singular integral (3.49) is obtained:

$$\int_0^S \xi\big(z(\sigma)-z(s_k)\big)T(\sigma)d\sigma = \frac{1}{z'_k}\left[T_k ln\left(\frac{\Delta s_k}{\Delta s_{k-1}}\right)+T_{k+1}-T_{k-1}\right]+$$

$$+\tfrac{1}{2}[\xi z_{k-1}-z_k)T_{k-1}\Delta s_{k-1}+\xi(z_{k+1}-z_k)T_{k+1}\Delta s_k]+$$

$$+\tfrac{1}{2}\textstyle\sum_{i=k+1}^{N+k-2}[\xi(z_{k+1}-z_k)T_i+\xi(z_{i+1}-z_k)T_{i+1}]\Delta s_i \qquad (3.51)$$

Next, we return to the Cauchy equation (3.48), governing the tracking of the oil-water with time. According to the expression for $\vec{V}(s)$for the determination of the velocity of the flood front, it is necessary to compute the normal and tangential velocity components. The values of *T*(*s*) and *N*(*s*) can be obtained by separating equation (3.39) it into real and imaginary parts:

$$\begin{cases} \frac{1+k}{2}T(s_k) = Re\left\{\left[F\big(z(s_k)\big) + \frac{1-k}{2\pi i}\int_0^S \xi\big(z(\sigma) - z(s_k)\big)T(\sigma)d\sigma\right]\frac{ds_k}{ds}\right\} \\ N(s_k) = Im\left\{\left[F(z(s_k) +)\frac{1-k}{2\pi i}\int_0^S \xi\big(z(\sigma) - z(s_k)\big)T(\sigma)d\sigma\right]\frac{ds_k}{ds}\right\} \end{cases} \quad (3.52)$$

Writing equation (3.52) for all the points on the oil-water contact z_k, we obtain two systems of matrix equations:

$$(T_{matrix})\vec{T} = \vec{T}_r;\ \vec{N} - (N_{matrix})\vec{T} = \vec{N}_r \quad (3.53)$$

where T_{matrix} and $N_{matrix}$are matrix coefficients for tangential velocity component, their determination of which can be carried out using equation (3.52) and the expression (3.51)

$$\int_0^S \xi\big(z(\sigma) - z(s_k)\big)T(\sigma)d\sigma = \frac{1}{2'_k}\Big[2T_k \ln\Big(\frac{\Delta s_k}{\Delta s_{k-1}}\Big) + T_{k+1} - T_{k-1} + \sum_{i=k+1}^{N+k-2}[\xi(z_{k+1} -$$

$$z_k)T_i(\Delta s_i + \Delta s_{i-1})]z'_k\Big]$$

On their own, the vectors $\vec{T}$and $\vec{N}$ indicated on the right hand sides in equation (3.53) and are defined by the equation:

$$\vec{T}_r = Re\left\{\begin{pmatrix} \phi\big(z(S_o)\big)\frac{dz_0}{ds} \\ \dots\dots \\ \phi\big(z(S_{N-1})\big)\frac{dz_{N-1}}{ds} \end{pmatrix}\right\};\quad \vec{N}_r = Im\left\{\begin{pmatrix} \phi\big(z(S_o)\big)\frac{dz_0}{ds} \\ \dots\dots \\ \phi\big(z(S_{N-1})\big)\frac{dz_{N-1}}{ds} \end{pmatrix}\right\}$$

Determining iteratively values of the vectors $\vec{T}$and $\vec{N}$ in equation (3.53), it is possible to obtain the value of $\bar{V}(s)$ from equation (3.41) for a given time, *t*. To solve the equation, known as the Cauchy problem, we apply the corresponding initial conditions and use a Runge-Kuta method, modified for the complex variable, z. For the integral variables we use a dimensionless time τ related to the given real time *t*, by the equation:

$$\tau = q_w t/2\pi\varphi h|\omega_1^2| \quad (3.54)$$

From equation (3.47), for initial condition at $t = 0$;

$$z(\theta, 0) = z_0 + r_w e^{i\theta} \tag{3.55}$$

In equation (3.54), in addition to the known parameter, ω_1 is one of the two periods of the doubly periodic lattice, while q_w is the water injection rate, from the equation for $\phi(z)$. It can be see from the equation for $\phi(z)$ the the injection rate and the production rate are equal. Therefore it is convenient to express the ratio q_u/q_w *as* q_w and indicate it outside the common bracket in the expression for dimensionless time, τ. The parameter θ in equation (3.55) indicates position of a streamline $z(\theta, t)$at time $t > 0$, starting at time $t = 0$ from point $z(\theta, 0)$ to point $z(\theta, t)$. Simply speaking, the solution $z(\theta, t)$ is the trajectory of the the streamlines, defined by the parameter θ, from the injection well to the production well. Thus, on simulation for different values of the parameter $0<\theta<\pi$, we obtain a set of water flow curves (streamlines) that spread out in the reservoir with time. Curves from the simulation of the quarter five-spot flood pattern are shown in Chapter 4

3.17 Numerical Solution

3.17.1 The well model

In its simplest form, a well is a vertical, open hole through which fluid can flow in and out of the reservoir. More advanced wells are cemented and then perforated along specific intervals along a path that may stretch kilometers along the reservoir in the horizontal direction. Production wells are for extraction of hydrocarbons, while injection wells may be used for disposal of produced water/gas, maintenance of reservoir pressure by voidage replacement, or for displacement of hydrocarbons towards production wells. Fluids injection and production rates are controlled at the surface or downhole by use of control devices.

A well model is used to accurately represent flow in a wellbore and provides equations that can be used to compute injection or production rates at a known bottom hole flowing pressure, or compute the pressure for a given well rate. When the flow equations presented above are discretized using a volumetric grid, the wellbore pressure will be significantly different from the average pressure in the perforated grid blocks. This is because the control-volume dimensions are significantly greater than the wellbore radius, which implies that large pressure gradients appear in a small region inside the perforated blocks. The flow rate in the well is proportional to the difference between the block and well pressure. Since the grid pressure and all other physical properties are assumed to be centered at the middle of the control-volume, the well is also assumed to be at the center of the grid cell (Figure 3.23).

The numerical model was applied to investigate waterflood performance in wellbores in the Agbada reservoir using Wolfram Mathematica 10 software. A simple reservoir model was specified to provide the source terms for the wells. Thus, the reservoir-wellbore simulator considerably acts as a standalone wellbore simulator.

3.17.2 Data Input

The experimental data obtained in Chapter 3 are used, in conjunction with other assumed properties, to validate the model developed above. In the model, a homogeneous and isotropic oil-bearing Agbada sandstone formation was tested through two vertical wells of average length 8,000 feet, each with one perforation at the bottom. The reservoir model is assumed to contain initially only oil and water, with zero initial gas saturation. It is homogeneous with respect to

porosity, anisotropic with respect to permeability and isothermal with respect to temperature. The physical domain consisted in a rectangular reservoir with an area of 30,000 ft^2, and a thickness of 30 ft. The porosity (calculated experimentally) was equal to 0.28, and the irreducible water saturation equal to 0.22. Permeabilities are 200, 150 and 50 in the x, y and z directions, respectively. Flow in the z-direction was assumed negligible. The maximum relative permeability to oil was 0.80 while the maximum relative permeability to water was 0.32. The initial reservoir pressure is assumed to be 3,800 psi. The wellbore radius was 0.5 ft and the rock compressibility was assumed equal to zero. For the sake of simplicity, zero mechanical skin was imposed. No-flow boundaries were assumed at the limits of the physical domain. Oil and water were modeled as incompressible fluids. These physical properties and others are summarized in Table 3.1. Both production and injection wells are vertical and completed in all the layers of the simulation model, four injectors at two sides and one producer at the center of the control element in a five-spot flood pattern (Figure 3.24).

Table 3.1: Fluid and reservoir properties used in the simulation

Property	**Value**	**Property**	**Value**
Initial reservoir pressure, psia	3,800	Capillary pressure, psi	0
Bubble point pressure, psia	3,345	Porosity	0.28
Well depth, ft	8,000	k_x, md	200
Depth to top of reservoir, ft	450	k_y, md	150
Rock compressibility, psi^{-1}	0	k_z, md	50
Water compressibility, psi^{-1}	$3.5x10^{-5}$	Reservoir thickness, ft	30
Oil compressibility, psi^{-1}	$4.7x10^{-4}$	Bottomhole pressure, psia	2,900
Reservoir Temperature, ^oF	190	Irreducible water saturation, (S_{wc})	0.22
Oil viscosity, mPa.s	2.8	Initial oil saturation, (S_{oi})	0.78
Viscosity ratio,	0.36	Initial water saturation, (S_{wi})	0.22
Water viscosity, mPa.s	1.03	Residual oil saturation, (S_{or})	0.20
Oil FVF, bbls/STB	1.18	Initial gas saturation, (S_{gi})	0
Water FVF, bbls/STB	1.0	Water injection rate, bbls/day	900

The optimization criteria used were arrival time of the leading waterfronts at the producing wells (grid blocks) and injection rate. To ensure a realistic representation of the well configurations and to have good control of the model being waterflooded, the model was thought of as being a small part cut out of a larger reservoir. This implied that all well blocks at the model boundary were being shared by other adjacent well patterns in the larger reservoir.

The pattern studied represents one element of a large number of such patterns in a water injection project for enhanced oil recovery. Thus, only a fraction of the productivity or injectivity of a boundary well block could be utilized by a well pattern.

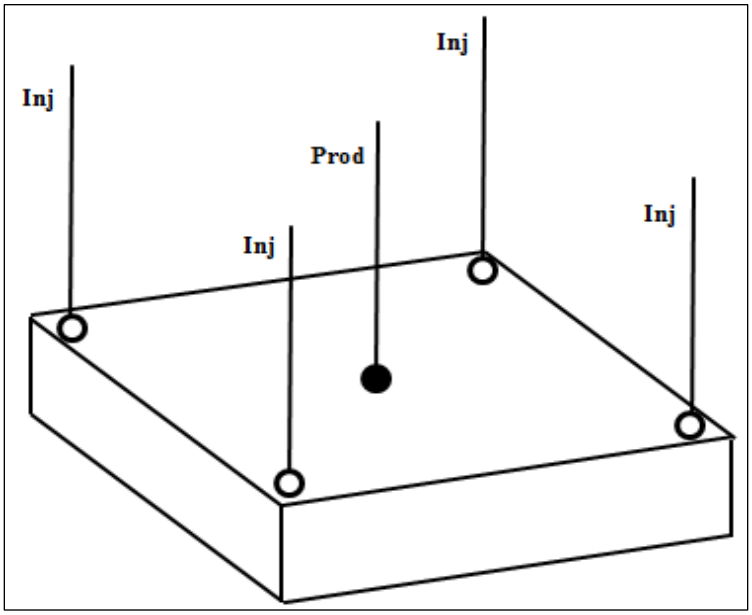

Fig. 3.24: Geometry of reservoir model and well locations on regular Cartesian grid.

3.17.3 Streamline path

Once the pressure field has been determined, the field of velocity vectors is defined in order to trace streamline paths. A streamline is defined as the instantaneous curve in space along which every point is tangent to the local velocity vector. Tracing streamlines from injectors to

producers is based on the analytical description of a streamline path within a gridblock as outlined by Pollock (1988). The underlying assumption is that the velocity field in each coordinate direction varies linearly and is independent of the velocities in the other directions. Pollock's method is attractive because it is analytical and consistent with the governing material balance equation.

3.17.4 Tracing Streamlines

Streamlines are traced from an arbitrary number of injection blocks to production blocks using equations (3.48) and (3.55). The streamline paths do not start at the center of an injection well since the velocity field cannot be approximated as piecewise linear within a lattice containing a point source. Rather, streamlines are launched from each lattice or gridblock face containing an injector. The number of streamlines to launch from an injection face can either be a constant for all faces, or can vary from face to face. Streamlines are launched in proportion to the flux out of a face, such that more streamlines are launched from high rate injectors, while fewer streamlines are launched from low rate injectors. Thus more streamlines are traced through high velocity regions and fewer streamlines are traced through low velocity regions.

The flux across each injection block face is uniform, consistent with the underlying velocity field. Since the flux is uniform, streamlines are distributed on each face in a uniform manner. One method for a uniform launching pattern of an arbitrary number of streamlines is to distribute the streamlines uniformly in the horizontal coordinate direction and randomly in the vertical coordinate direction. This launching pattern allows for the intersection of a maximum number of lattices or gridblocks for a fixed number of streamlines. Not every gridblock in the domain will

contain a streamline for a fixed total number of streamlines launched. A missed gridblock is assigned a streamline which is then traced backwards in the velocity field towards an injector.

3.18 Time stepping and simulation scheme

The fundamental idea of the Weierstrass elliptic function method is that streamline paths are allowed to change with time in accordance with the changing pressure/mobility field. The pressure field therefore needs to be updated and saturations transported forward in time.

The numerical simulation scheme involves the following time step:

1. Input data and state initial well conditions

2. Calculate the pressure field by solving equation (3.44).

3. Determine the total velocity field at gridblocks, using Darcy's law.

4. Trace streamlines using equation (3.48). While tracing a streamline, use equation (3.55) with current time step, map the 1-D analytical solution along each streamline for a pre-specified time step and map the solution back to the lattice.

5. Trace all streamlines, check for missed grid-blocks, and determine the average saturation and total mobility of each grid- block.

6. Calculate the real time, *t*, at which the new saturation distribution exists using equation (3.47).

7. Return to Step 2.

8. Repeat until convergence is reached, then terminate

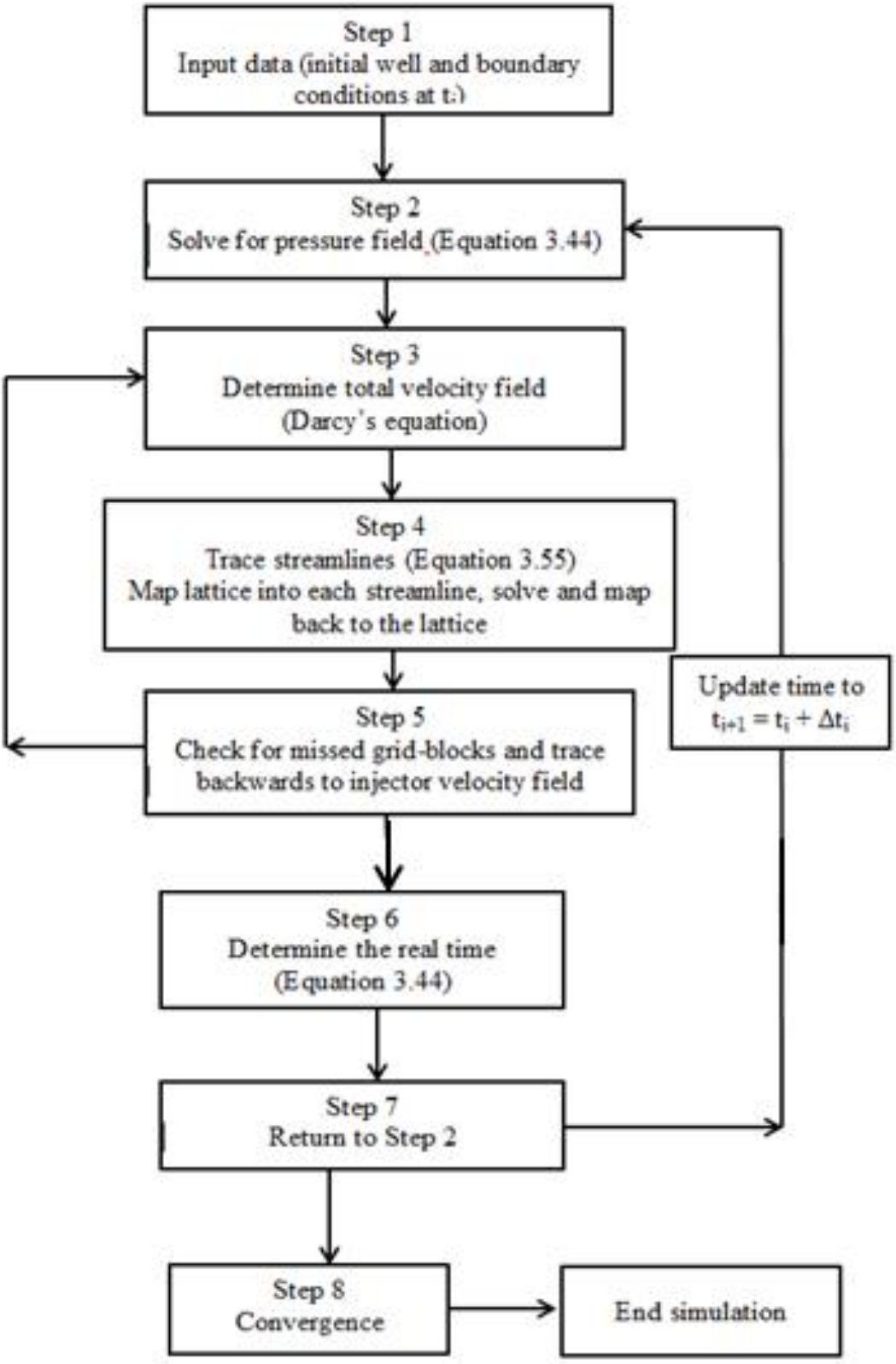

Fig. 3.25: Simulation scheme for Weierstrass elliptic functions

Chapter 4

Results and Analysis

In this chapter all the relevant calculated values and the final results from the experimental procedures are presented. Obtained data is given in the appendices while the numerical results are reported here.

4.1. Mineralogy, Porosity and Permeability

The mineralogy and petrophysical properties of the Agbada sandstone core samples used in this study are shown in Tables 4.1 and 4.2 respectively. In Figure 4.1 the initial porosity (red color) and permeability (blue color) for all 12 core plugs are presented graphically. Porosity data, core dimensions and weights are given in Appendix A1.

Table 4.1: Mineralogy of the Agbada sandstone cores (wt.%)

Mineral	**Quartz**	**Albite**	**Calcite**	**Dolomite**	**Kaolinite**	**Muscovite**
% Comp	78	16	2.8	0.6	2	0.6

Table 4.2 Porosity and permeability of the core plugs measured in the laboratory

Core ID	**A_1**	**A_2**	**B_1**	**B_2**	**C_1**	**C_2**	**D_1**	**D_2**	**E_1**	**E_2**	**F_1**	**F_2**
Porosity	28.9	27.2	28.6	28.1	28.2	27.8	27.3	26.8	28.1	27.5	28.0	27.7
Permeability	1791	1602	1780	1722	1654	1698	1589	1622	1776	1675	1745	1734

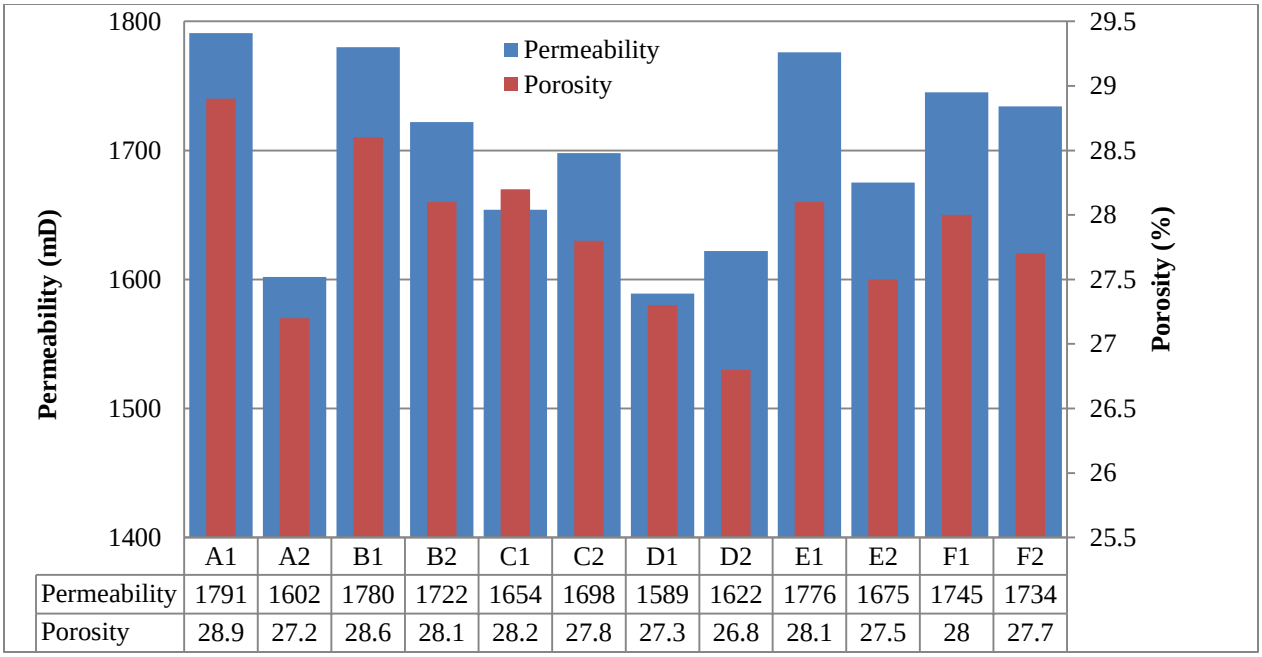

	A1	A2	B1	B2	C1	C2	D1	D2	E1	E2	F1	F2
Permeability	1791	1602	1780	1722	1654	1698	1589	1622	1776	1675	1745	1734
Porosity	28.9	27.2	28.6	28.1	28.2	27.8	27.3	26.8	28.1	27.5	28	27.7

Figure 4.1: Graphic presentation of the experimental porosity and permeability of the core plugs

Properties of the core samples are shown in Table 4.3, while Tables 4.4 and 4.5 show properties of the formation water and crude oils respectively

Table 4.3: Measured properties of the Agbada core plugs

Core ID	Diameter(cm)	Length(cm)	Porosity (%)	Absolute Permeability (mD)
A_1	3.82	7.87	28.9	1791
A_2	3.83	7.86	27.2	1602
B_1	3.81	7.65	28.6	1780
B_2	3.82	7.75	28.1	1722
C_1	3.81	8.12	28.2	1654
C_2	3.82	7.78	27.8	1698
D_1	3.83	7.62	27.3	1589
D_2	3.81	7.81	26.8	1622
E_1	3.83	7.68	28.1	1776
E_2	3.83	7.66	27.5	1675
F_1	3.83	7.67	28.0	1745
F_2	3.82	7.82	27.7	1734

4.1.1 Core representative samples

A statistical analysis was carried out on the core plug samples. The precision of the analysis was less than 0.5. Based on the analysis, five representative core samples were chosen for the core flooding experiments.

Table 4.4: Water composition used in the flooding experiments

Iron	**Na^+**	**Ca^{2+}**	**Mg^{2+}**	**K^+**	**Cu^{2+}**	**Ba^{2+}**	**SO_4^{2-}**	**Cl^-**
Conc. (g/l)	77.8	24.1	3.1	2.8	0.002	0.179	0.13	151

Table 4.5: Properties of crude oils

Oil Sample	**Density (g/cm^3)**	**Viscosity (cP)**	**Acid Number (mgKOH/gOil**	**Base Number (mgKOH/gOil**
Bonny Light	0.8479	2.8	0.221	0.08
Forcados Blend	0.8811	3.4	0.237	0.17

4.2 Calculation of porosity and absolute permeability from x-ray CT images

According to the above method, voxel porosities of CT images of the core samples are calculated using the imagej software. The results shown in Table 4.6 indicates that there is good agreement between laboratory porosity measurement using core plugs (Tables 4.2 and 4.3) and the values evaluated from CT scanning. While laboratory measurements using helium porosity gives effective porosity (connected pore spaces), the voxel counting algorithm results in a higher porosity, since all of the voxels defined as pore space in the core system are accounted for. Analysis of the results, both experimental and X-ray CT images show that on the average the core samples were homogenous in porosity.

The results of the simulations of the transport properties of the extracted network were performed using the two-phase pore-scale simulator developed at Imperial College London

(Valvatne and Blunt, 2004). The saturation was calculated using the prevailing maximum in capillary pressure to compute the radius of curvature of the fluid interfaces. Absolute permeability *k* of the network is derived from Darcy's law,

$$k = \frac{\mu_p q_{tsp} L}{A(\phi_{in} - \phi_{out})} \quad (4.1)$$

where the network is fully saturated with a single phase *p* of viscosity μp, flowing at a rate of q_{tsp} through the pore network of length L with a potential difference ($\boldsymbol{\phi}_{in} - \boldsymbol{\phi}_{out}$), across a cross-sectional area A of the model. The calculations yielded three simulated absolute permeability results in the *x (kx)*, y (*ky*), and *z (kz)* directions per core plug (one for each pair of axial inlets-outlets). They are presented in Table 4.6

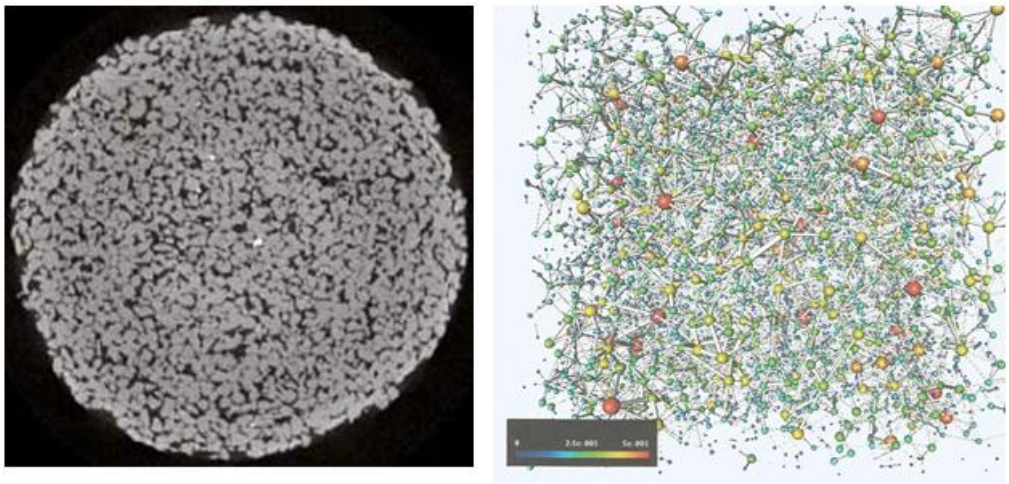

Figure 4.2: 2D section of the micro-CT image of Agbada rock sample and the extracted network. The image resolution is 8 microns

Table 4.6: Calculated transport properties for the Agbada core samples studied

Parameter/Sample	A_1	B_1	C_2	D_2	E_1	*Average*
Diameter (cm)	3.82	3.81	3.82	3.81	3.83	3.82
Length (cm)	7.87	7.65	7.78	7.81	7.86	7.86
Resolution (μ)	8.0	8.0	8.0	8.0	8.0	8.0
Porosity (%)	34.9	34.6	33.8	32.9	33.2	33.2
Permeabilty: k_x (mD)	193	210	219	176	208	201.2
k_y (mD)	169	125	181	120	154	149.8
k_z (mD)	48	52	60	40	52	50.4

4.3 Relative permeability and saturation curves

Tables 4.7 and 4.8 show the results of the relative permeability of the core samples before and after wettability alteration by aging. From these tables and Figures 4.3 and 4.4 it can be see that the relative permeabilities of the wetting phase for brine system are lower than the relative permeabilities of the wetting phase for an oil system, while it is the opposite for the non-wetting phase relative permeabilities. This shows that altering the wettability of the core samples from water-wet to oil-wet increases the relative permeability of the wetting phase, indicating the effect of wettability alteration on oil recovery from the reservoir. As the water saturation increases, the water to oil relative permeability ratio increases.

Table 4.7 Experimental relative permeability values before wettability alteration

S_w	0.20	0.25	0.30	0.35	0.40	0.45	0.50	0.55	0.60	0.65	0.70	0.75	0.80
k_{rw}	0.00	0.002	0.008	0.021	0.034	0.052	0.075	0.100	0.130	0.168	0.208	0.250	0.301
k_{ro}	0.798	0.622	0.468	0.371	0.284	0.217	0.162	0.120	0.080	0.052	0.027	0.019	0.00

The trend in relative permeability relationship to wettability observed in Tables 4.7 and 4.8 is also illustrated in Figures 4.3 and 4.4. It is observed that for all values of water saturation above the initial water saturation, the relative permeability to water decreases with increasing water-wetness. At water saturation of 60%, the relative permeability of the rock to water is 11% while that to oil is 12.8% for the strongly water-wet Agbada formation. Beyond the cross-over values, the relative permeability to water at the same saturation increases while that to oil decreases towards zero. The cross-over saturations of the samples are more than 0.5. This is considered as an indication of water wetness of the Agbada formation.

Table 4.8: Experimental relative permeability values after wettability alteration

S_w	0.22	0.29	0.36	0.38	0.44	0.48	0.54	0.62	0.69	0.73	0.78	0.86	0.89
k_{rw}	0.00	0.003	0.012	0.028	0.041	0.059	0.084	0.110	0.143	0.175	0.226	0.258	0.321
k_{ro}	0.807	0.628	0.479	0.384	0.296	0.228	0.173	0.128	0.091	0.063	0.036	0.028	0.00

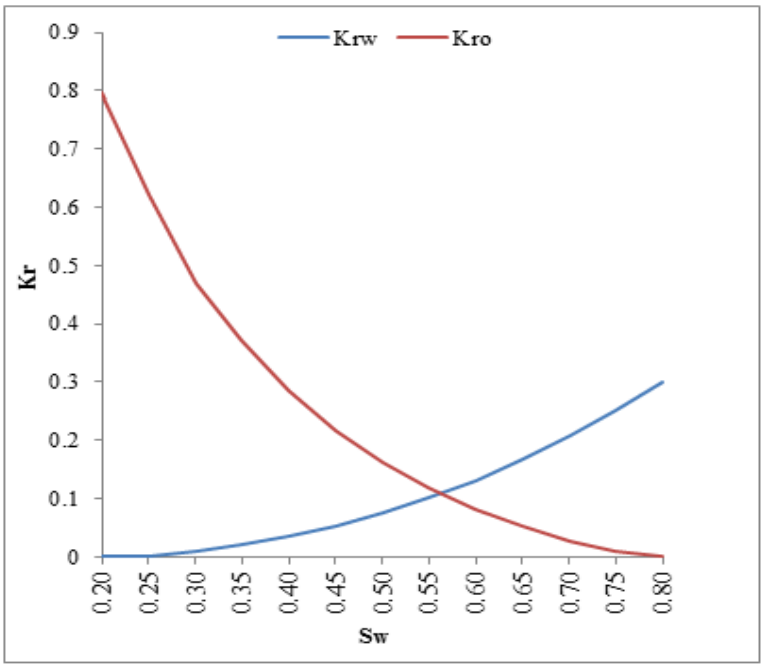

Figure 4.3: Plot of initial relative permeability

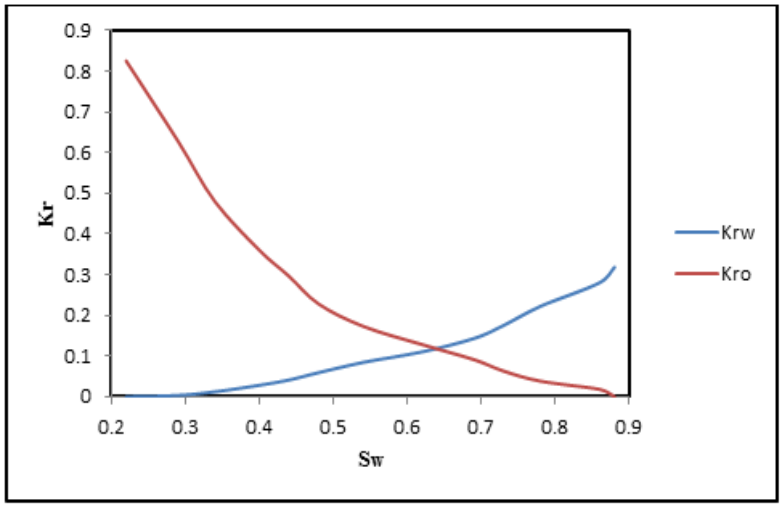

Figure 4.4: Plot of relative permeability after wettability alteration

4.4 Wettability measurement

Results from initial wettability measurement are presented in Table 4.9, while a plot of spontaneous imbibition rates for the first five hours is shown in Figure 4.5

Table 4.9: Summary of laboratory wettability measurements using Amott method

Core ID	Spontaneous displ. of oil, cc	Forced displ. of oil, cc	Spontaneous displ. of oil, cc	Forced displ. of oil, cc	I_w	I_o	$I_{w\text{-}o} = I_w - I_o$
A_1	1.70	0.50	0.40	4.25	0.7692	0.0093	0.7599
B_1	8.70	3.38	1.28	9.20	0.7202	0.1221	0.5981
C_1	4.30	0.10	0.15	11.30	0.9973	0.0131	0.9642
D_1	1.60	0.10	0.05	5.70	0.9412	0.0087	0.9325
E_2	3.40	0.15	0.10	8.30	0.9577	0.0119	0.9458

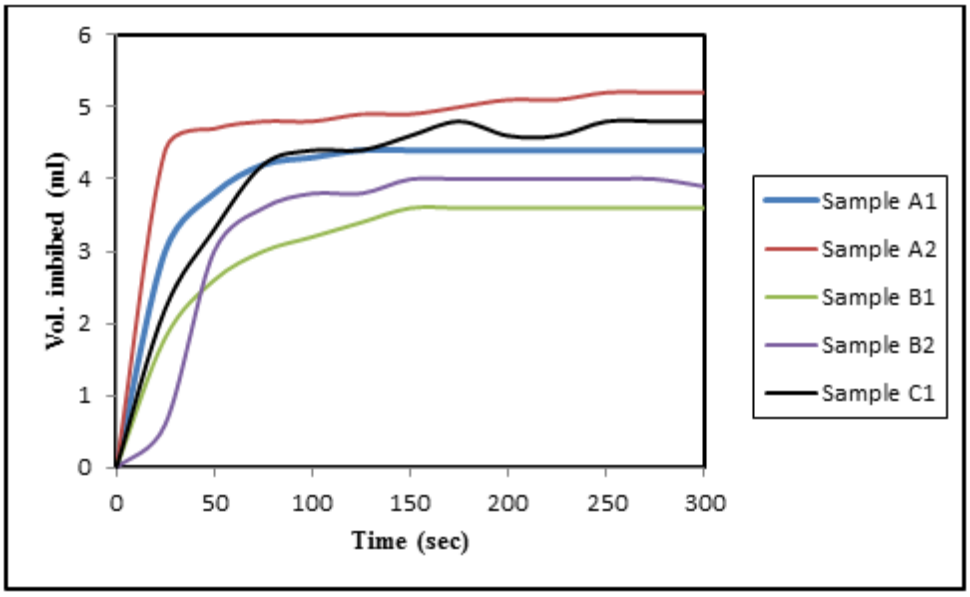

Figure 4.5: Spontaneous imbibition rates for initial wettability determination

4.5 Effect of Amott-Harvey index on oil recovery

At the start of waterflooding, as S_{wi} increases, the number of initially oil-filled elements will decrease rapidly. After water breakthrough, there is a gradual increase in water relative

permeability resulting from a single water cluster originating from the reservoir, established by a connected path of water-filled elements across the system giving a more gradual increase in k_{rw}.

There is less effect of S_{wi} on the oil relative permeability. The last elements to be filled during waterflooding in oil-wet conditions are the largest, resulting in large oil relative permeability hysteresis. Before the crossover point, the oil relative permeability for a given S_{wi} will thus lie above those starting from a lower S_{wi}. The effects of S_{wi} on both oil and water relative permeability combine to give lower fractional water flow, and subsequently higher recovery, as S_{wi} increases. There is, however, an optimal S_{wi} above which recovery again starts to decrease, as shown in Figure 4.6. It is therefore evident from Figure 4.6 that oil recovery from the Agbada reservoir increases as the rock becomes less water-wet and that in terms of the initial water saturation, S_{wi}, there is a limit range that gives optimal oil recovery. Oil initially in place (OIIP) was calculated using the volumetric method for oil reserves estimation.

Table 4.10: Summary of Amott-Harvey wettability effect on waterflood oil recovery

Amott-Harvey index	Oil recovery, % OIIP		Amott-Harvey index	Oil recovery, % OIIP
-0.96	0.52		0.10	0.80
-0.92	0.55		0.20	0.79
-0.90	0.56		0.30	0.74
-0.80	0.60		0.40	0.68
-0.60	0.61		0.60	0.66
-0.52	0.68		0.70	0.63
-0.40	0.66		0.74	0.62
-0.30	0.68		0.80	0.60
-0.20	0.69		0.90	0.55
0.00	0.77		1.00	0.54

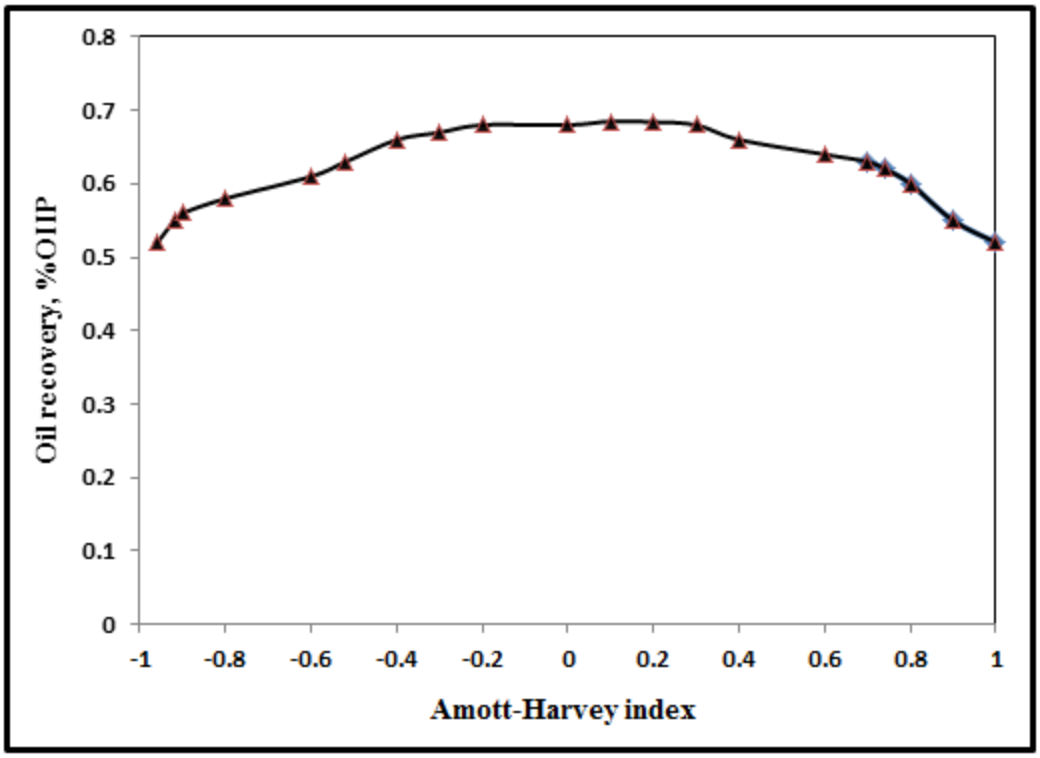

Figure 4.6: Experimental oil recovery as a function of Amott-Harvey wettability index, I_{w-o} (after 5 PV)

Figure 4.7 shows the relative permeabilities, fractional flows and recovery curves as a function of wettability, with an S_{wi} of 0.22. Water relative permeability and residual oil saturation increase with I_{w-o}. The trend in residual saturation has been discussed by McDougall and Sorbie (1995) and Blunt (1997). After primary drainage, oil occupies the centers of large pores and throats while their corners and smaller elements are still filled with water. In strongly water-wet media, as the Agbada reservoir, water will flow readily through the wetting layers in the corners of the pore space. At the inlet of the core the water is poorly connected through the pore space. As the pore volume of water injected increases the water saturation increases due to a connected path of water-filled pores and throats in the larger elements, leading to an increasing water relative permeability with saturation in an oil-wet medium.

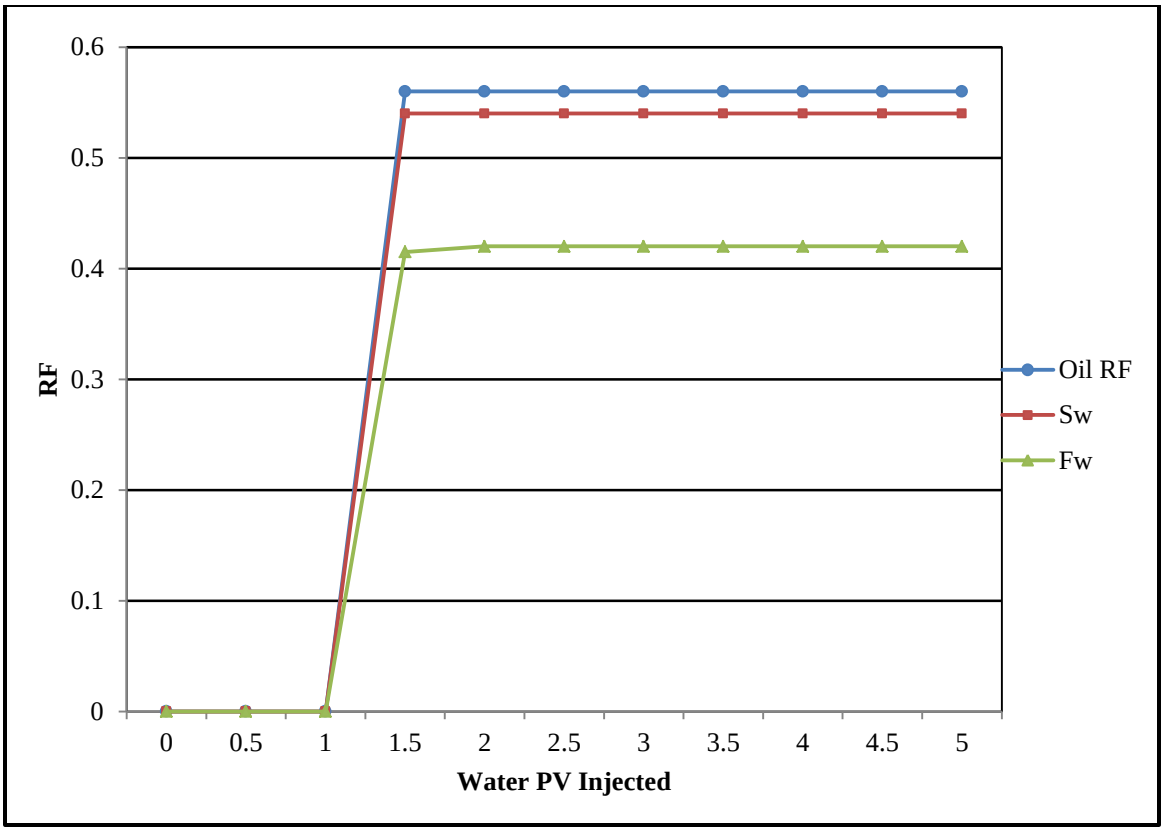

Figure 4.7: Effect of wettability on waterflood oil recovery (after 5 PV)

4.6 Buckley-Leverret Calculations

Before water breakthrough the saturation profile is easily obtained and the volume of oil recovered is assumed to be equal to the volume of water injected. It is necessary to evaluate the oil recovery after breakthrough. The values in Table 4.11 are calculated from experimental data obtained in this work.

Table 4.11: Water saturation and ratio of oil/water relative permeabilities

S_w	0.20	0.25	0.30	0.35	0.40	0.45	0.50	0.55	0.60	0.65	0.70	0.75	0.80
k_{ro}	0.798	0.900	0.83	0.740	0.660	0.440	0.270	0.170	0.104	0.058	0.033	0.019	0.000
k_{rw}	0.0	0.004	0.008	0.016	0.034	0.052	0.072	0.100	0.130	0.168	0.208	0.250	0.301
k_{ro}/k_{rw}	∞	225.0	103.75	46.25	19.41	8.46	3.75	1.70	0.80	0.35	0.16	0.076	0.000

The values in Table (4.11) are used to plot the water ratio relationship. According to Craft and Hawkins (1991), the mathematical relationship between, S_w and relative permeability is given by:

$$\frac{k_{ro}}{k_{rw}} = ae^{bS_w} \tag{4.2}$$

where

k_{ro} = relative permeability to oil

k_{rw} = relative permeability to water

S_w = water saturation at the production well

The values of a and b are calculated from the semi-log plot of k_{ro}/k_{rw} vs S_w using excel. This gives a = 12439; b =16.1 respectively.

Next, equation (3.20.) is used to calculate the producing water cut, f_w, while equation (3.22) is used to calculate $(\partial f_w/\partial S_w)_{sw}$, and then, the fractional water flow is plotted as a function of water saturation. Next, equation (3.20.) is used to calculate the producing water cut, f_w, while equation (3.22) is used to calculate $(\partial f_w/\partial S_w)_{sw}$, and then, the fractional water flow is plotted as a function of water saturation.

In the waterflooding experiment, fluid viscosities are:

Water = 1.03 *mPa.s*

Bonny Light oil = 2.8 *mPa.s*, and

Forcados Blend oil = 3.4 *mPa.s*

Formation volume factors are $B_o = 1.18\, rb/stb$ for oil and $B_w = 1.0\, rb/stb$ for water

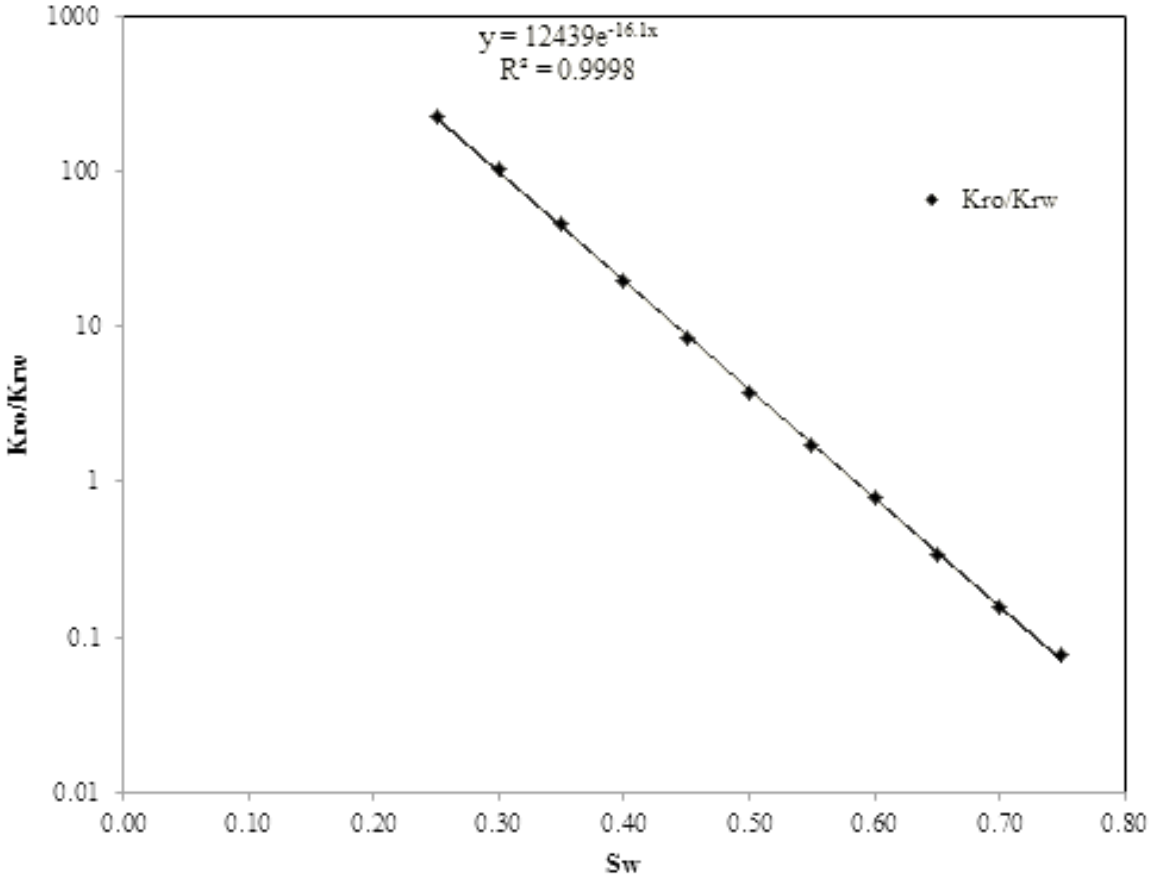

Figure 4.8: Semi-log plot of water saturation vs. relative permeability ratio

Table 4.12: Plotting data for Bonny Light oil (μ_w/μ_o = 0.368 = constant)

S_w	f_w	$(\partial f_w/\partial s_w)_{sw}$
0.25	0.062	0.862
0.30	0.106	1.363
0.35	0.173	1.977
0.40	0.271	2.558
0.45	0.398	2.860
0.50	0.540	2.715
0.55	0.675	2.212
0.59	0.779	1.644
0.60	0.787	1.586
0.65	0.868	1.027
0.70	0.921	0.635
0.75	0.954	0.393

Figure 4.9 shows the fractional water flow as a function of saturation. From the figure it can be observed that the minimum water saturation behind the flood front is 59%. A plot of the fractional flow curve for the Forcados Blend oil is also shown in Figure 4.10. Table (4.13) shows the calculated fractional values.

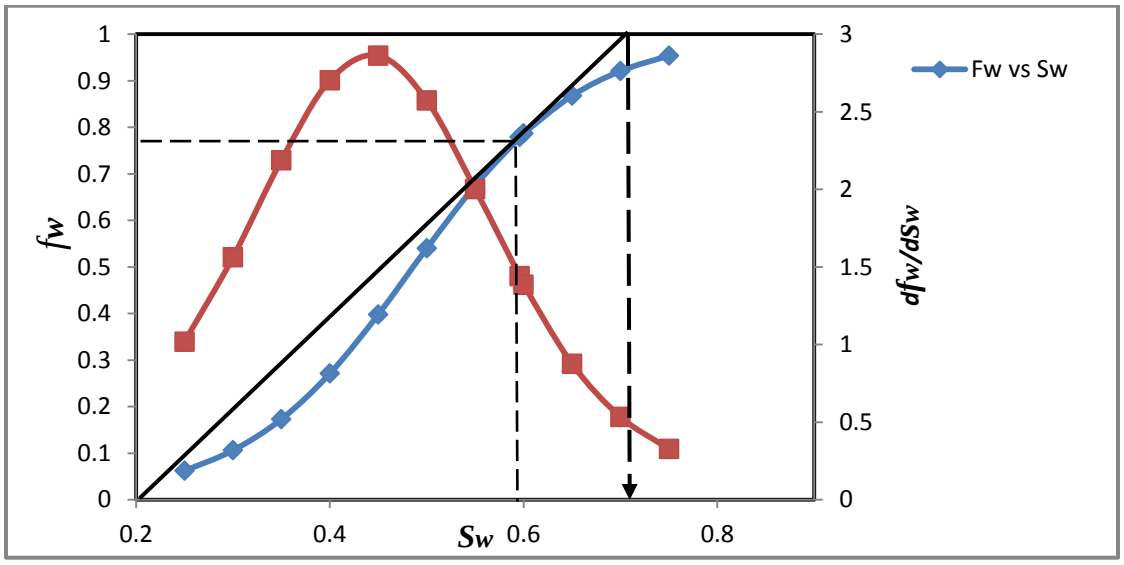

Figure 4.9: Fractional flow curve for Bonny Light crude oil

Table 4.13: Plotting data for Forcados Blend oil (μ_w/μ_o = 0.303 = constant)

S_w	f_w	$(\partial f_w/\partial s_w)_{sw}$
0.25	0.098	0.963
0.3	0.163	1.498
0.35	0.257	2.101
0.4	0.381	2.592
0.45	0.522	2.745
0.5	0.661	2.468
0.54	0.750	1.921
0.55	0.790	1.781
0.6	0.859	1.229
0.65	0.917	0.841
0.7	0.951	0.512
0.75	0.971	0.314

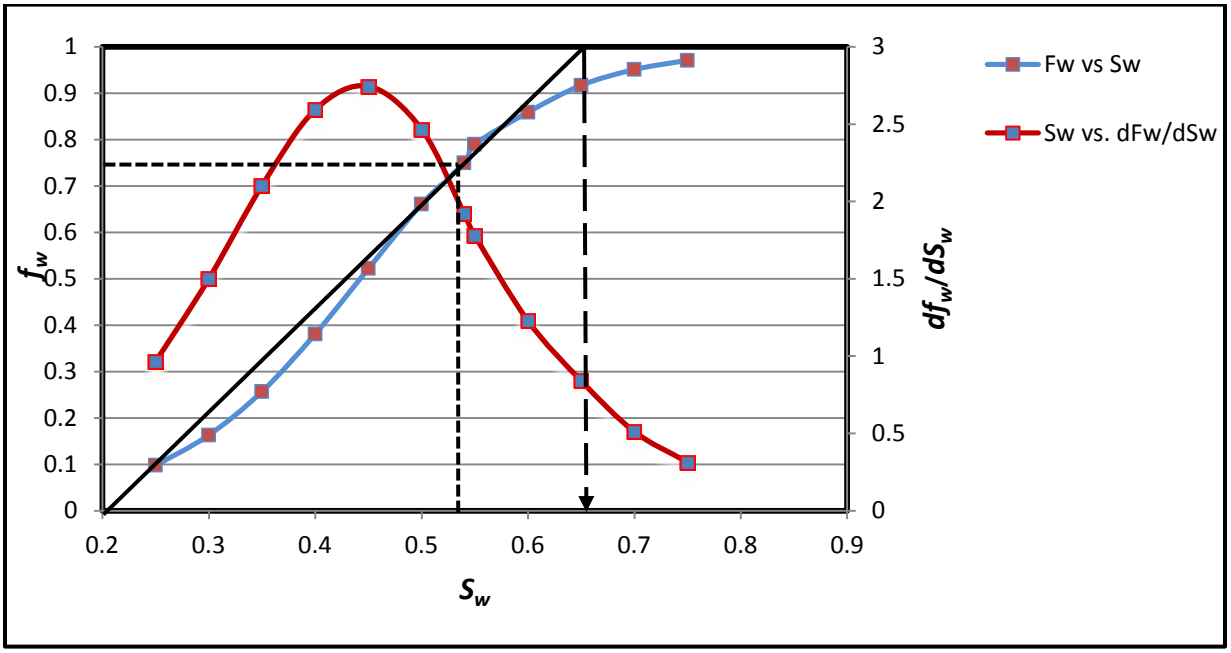

Figure 4.10: Fractional flow curve for Forcados Blend oil

From the fractional flow curve, several important information about a waterflood performance can be derived. By drawing a straight line tangent to the fractional flow curve, starting at $f_w = 0$ and $S_w = S_{wi}$, the followings are observed:

1. At the tangent point, the corresponding S_w is the water saturation at the flood front.
2. The corresponding f_w is the fraction of water flowing at the flood front.
3. The water saturation value where the tangent line intersects ($f_w = 1.0$) is the average water saturation in the reservoir at breakthrough. This is for a single-layer system.
4. Displacement efficiency (E_D) at breakthrough is calculated by:

$$E_D = \frac{(PV)[(S_{oi}/B_{oi}) - \bar{S}_o(\bar{S}_o/B_o)]}{(PV)S_{oi}/B_{oi}} = \frac{[(S_{oi}/B_{oi}) - \bar{S}_o(\bar{S}_o/B_o)]}{(S_{oi}/B_{oi})} \quad (4.3)$$

Figure 4.10 indicates that the flood front leading edge has a water saturation of 54%, i.e., water saturation behind the flood front has a minimum value of 54% ($S_{w\,min}$ = 0.54). This value is lower than the value for Bonny Light oil, and can be explained by the difference in viscosities of the two oils. In the calculations that follow concentration is placed on the Bonny Light oil.

Water saturations ranging from 60% to 80% (80% = 1 - S_{or}) is assumed, and calculation of the oil bank saturation profile made using the equation:

$$(x)S_w = \left(\frac{5.615 I_w t}{\emptyset A}\right)\left(\frac{df_w}{dS_w}\right)_{S_w} \tag{4.4}$$

Using water injection rate I_w of 900 bbls/day, average porosity of 0.28 (Table 4.1), and assuming a flood area of 30,000 square feet, equation (4.3) becomes

$$(x)S_w = \left(\frac{(5.615)(900)t}{(0.28)(30{,}000)}\right)\left(\frac{df_w}{dS_w}\right)_{S_w} = (0.602t)\left(\frac{df_w}{dS_w}\right)_{S_w} \tag{4.5}$$

We calculate the distance from the injection well to the producing well at water saturation, S_w, from 60% to 80%.

Table 4.14: Distances from injector well to producer well at S_w 60% to 75%

$\partial f_w/\partial S_w$	$t = 60$	$t = 120$	$t = 240$	S_w
1.640	96	190	370	0..6
1.282	58	136	285	0.65
0.898	44	86	174	0.70
0.602	26	58	112	0.80

Plotting the values in Table 4.14 above helps to visualize the waterflood front at 60, 120, and 240 days, respectively (Figure 4.11).

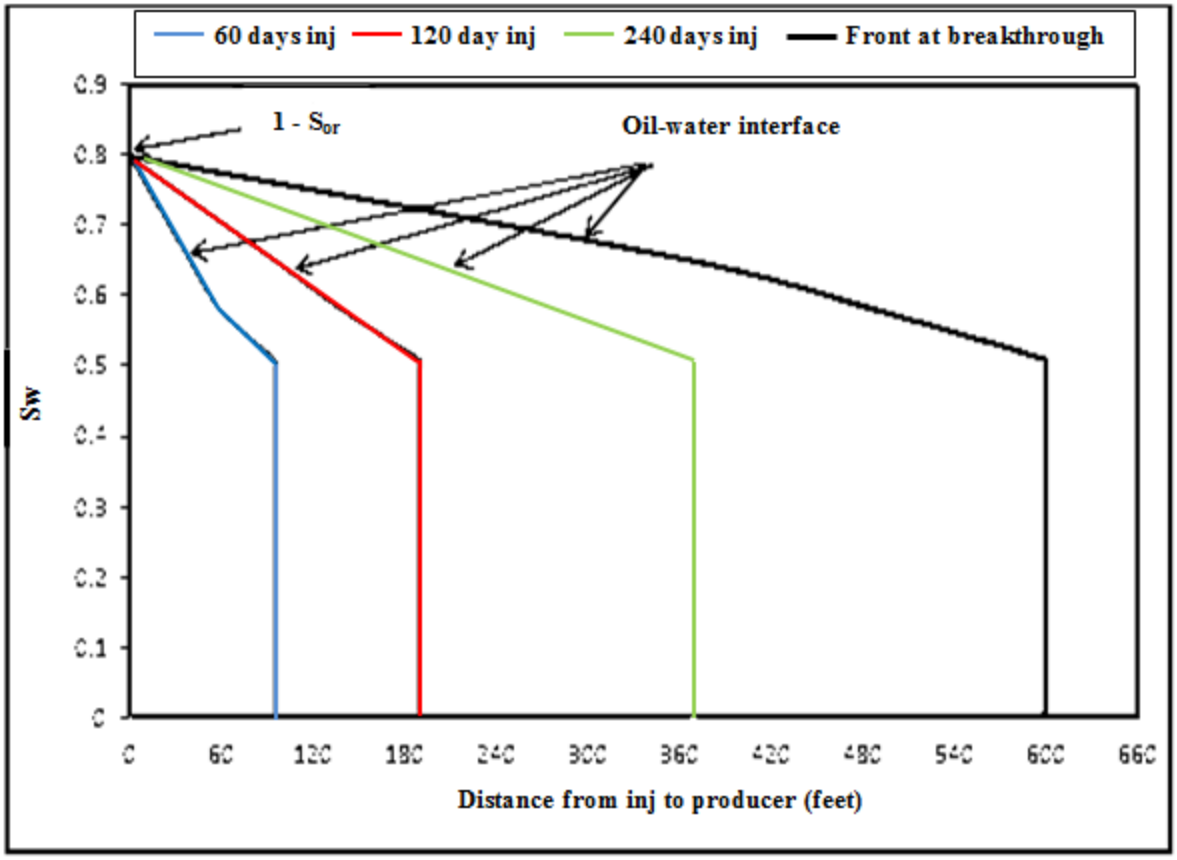

Figure 4.11: Water saturation S_w versus water injection time

Next, the time to water breakthrough is calculated. The pore volume, *PV*, is given by the equation:

$$\left.\begin{aligned} PV &= \frac{\emptyset AL}{5.615} \\ OIIP &= \frac{7758xPVx\varphi x(1-S_W)}{B_o} \end{aligned}\right\} \quad (4.6)$$

where the figure 7758 is conversion factor for PV in acre-feet to barrels, φ, S_w and B_o are porosity, water saturation and oil formation value factor, respectively,

Assuming $(x)S_w = L$ = 600 feet, area A = 25 acres and reservoir thickness, h = 30 feet, the time to water breakthrough, t_{bt} is estimated using equation (4.4). L is the distance from the injector well

to the producer well. Combining equations (4.4) and (4.6), the following equation is obtained for t_{bt}:

$$t_{bt} = \left(\frac{PV}{I_w}\right)\left(\frac{1}{\frac{df_w}{dS_w}}\right) \tag{4.7}$$

Inserting the given data,

$$OIIP = N_i = \frac{PV(1 - S_w)}{B_o} = \frac{1{,}629{,}136(1 - 0.25)}{1.18} = 1{,}035{,}468\ barrels$$

$$t_{bt} = \left[\frac{(1{,}035{,}468)}{900}\right]\left(\frac{1}{1.644}\right) = 699.8\ days$$

At breakthrough at the producing well estimated cumulative water injected, I_{wbt} is given by the equation:

$$I_{wbt} = I_w t_{bt} \tag{4.8}$$

$$I_{wbt} = (900)(699.8) = 629{,}820\ barrells$$

Estimated total pore volume of water injected at breakthrough Q_{wbt}

$$Q_{wbt} = \frac{1}{\left(\frac{df_w}{dS_w}\right)_{S_w}} \tag{4.9}$$

$$Q_{wbt} = \frac{1}{1.644} = 0.608\ PV$$

The water-oil ratio at the surface (WORs) at breakthrough is calculated using the following equation:

$$WOR_s = \frac{B_o f_w}{B_w(1 - f_w)} \tag{4.10}$$

$$WOR_s = \frac{(1.18)(0.779)}{(1.0)(1 - 0.779)} = \frac{0.9192}{0.221} = 4.16$$

After breakthrough both oil and water will be produced. The fractional flow in the reservoir is obtained by equation (4.4) while the producing water-cut at the surface is estimated by the following equation:

$$f_{ws} = \frac{{}^{q_w}/_{B_w}}{{}^{q_w}/_{B_w} + {}^{q_o}/_{B_o}} \tag{4.11}$$

Combination of equations (4.4) and (4.11) yields the following expression for the surface water-cut:

$$f_{ws} = \frac{1}{1+\frac{B_w}{B_w}\left(\frac{1}{f_w}-1\right)} \tag{4.12}$$

4.6.1 Overall recovery efficiency

The overall recovery efficiency or factor, RF, is given by the following general expression:

$$RF = E_D E_V = E_D E_A E_L \tag{4.13}$$

where

N_i = Oil initially in place (OIIP) at start of waterflood

E_D = displacement efficiency

E_V = volumetric sweep efficiency = $E_A x E_L = \left(\frac{A_d}{A_R}\right) xhx\varphi xS$

E_A = areal sweep efficiency

E_L = vertical sweep efficiency

A_d = area of displacement, A_R = area of reservoir

h = reservoir thickness

φ = porosity

S = Saturation

Using all these definitions, the cumulative oil production, N_p can be expressed as:

$$N_p = N_i E_D E_A E_L \tag{4.14}$$

4.6.2 Calculation of displacement efficiency, E_D

Mathematically, displacement efficiency is expressed as:

E_D = (volume of oil at start of flood – remaining oil volume)/(volume of oil at start of flood)

$$E_D = \left[PV\left(\frac{S_{oi}}{B_{oi}}\right) - (PV)\bar{S}_o\left(\frac{\bar{S}_o}{B_o}\right)\right] / \left[(PV)\left(\frac{S_{oi}}{B_{oi}}\right)\right] \tag{4.15}$$

where

S_{oi} = initial oil saturation at start of flood

B_{oi} = oil formation volume factor at start of flood

S_o = average oil saturation in the flood area at a particular time during the flood

4.6.3 Mobility ratio

An important parameter in the determination of the effectiveness of a waterflood is the end point mobility ratio, defined as the mobility of the displacing fluid (water) to the mobility of the displaced fluid (oil),

$$M = \frac{k_{rw}/\mu_w}{k_{ro}/\mu_o} \tag{4.16}$$

For the two cases (Bonny Light and Forcados crudes) under consideration, the mobility ratios are:

$$M_{1(Bonny\ Light)} = \frac{0.216/1.03}{0.800/2.8} = 0.7 < 1$$

$$M_{2(Forcados\ Blend)} = \frac{0.165/0.235}{0.8/3.4} = 0.7 < 1$$

In both cases the mobility ratio, M, is less than 1. A more significant parameter for characterizing the stability of Buckley-Leverett displacement is the shock front mobility ratio, M_s, which is defined as:

$$M_s = \frac{k_{ro}(S_{wf})/\mu_o + k_{rw}(S_{wf})/\mu_w}{k_{ro}/\mu_o} \quad (4.17)$$

Backed by experiment and theoretical reasoning Hagoort has shown that Buckley-Leverett displacement will be considered stable if $M_s < 1$. In the two cases considered the oil/water viscosity ratios, i.e., M and M_s are less than unity, which indicates stable and favourable type displacement of oil by waterflooding in the Agbada sandstone formation. The velocity and the efficiency of the waterflood depend significantly on the mobility ratio of the displacing fluid (water) to the displaced fluid (oil); the lower this ratio, the lower the front velocity and the more efficient the displacement process. Table 4.15 shows the calculated shock front mobility ratios.

Table 4.15: Shock front mobility ratios

Case	μ_o/μ_w	S_{wf}	$K_{rw}(S_{wf})$	$K_{ro}(S_{wf})$	M_s
Bonny Light	2.72	0.59	0.131	0.078	0.54
Forcardos Blend	3.30	0.54	0.096	0.118	0.55

The plotting of the fractional flow curves involved various steps of calculations, as shown above The irreducible water saturation had the most effect on the fractional flow curve, because relative permeability is a function of water saturation. By observing the curves the following analysis can be made:

1. Fractional flow is a function of relative permeability of both oil and water

2. The starting point of the fractional flow curve will shift, based on the initial water saturation.
3. If the irreducible water saturation is increased in steps of say, 10% for a given set of input parameters, the breakthrough water saturation value will advance by a constant value. The breakthrough fractional flow value will remain the same.
4. For a given set of oil/water relative permeability, if the relative permeability of water increases, the water saturation will increase and the relative permeability of oil will decrease.
5. If the oil viscosity is high, then the fractional flow of water will increase. Alternately, if the water viscosity is high, the fractional flow of water will decrease.

The residual oil saturation will have a similar effect on the fractional flow curve:

1. Increasing the residual oil saturation by maintaining lower water saturation, will result to the fractional flow curve becoming steeper.
2. If the residual oil saturation is increased in steps of say, 10% for a given set of input parameters, the breakthrough water saturation will decrease in constant steps, and the breakthrough fractional flow of water will remain constant.

4.7 Results of numerical calculations

In this work a model based on Weierstrass elliptic functions has been proposed for use in the simulation of immiscible displacement during waterflooding in homogeneous porous formation. Though the model presented in this work shows promising results when implemented on the Wolfram Mathematic software, there are still several issues that must be addressed before the

method can be applied to practical simulations, One of the issues is the code listing for the simulation which requires some fine-tuning. However, the model is used in this work to track the evolution of the flood front with time and Saffman-Taylor instability problem, dimensionless time for water breakthrough into the production well and the areal sweep. The results of the simulations and shown in the figures that follow.

4.7.1 Streamline flow

First, the nature of fluid flow in the reservoir system is simulated. The displacement of oil by water in a waterflood is characterized by low Reynold's number, that is, both fluids flow in streamlines. The streamline flow velocity distribution is modeled by the Weierstrass zete-function expressed the variant of equation (3.43). Using this expression the nature of the fluid flow (streamlines) from injection to production wells for a five-spot pattern (Figure 3.23) is modeled and the result shown in Figure 4.12.

4.7.2 Instability condition and viscous fingering

Next, a linear stability analysis is performed on the Saffman-Taylor problem in order to determine when discontinuity starts to occur on the oil-water interface or to get an instability condition on the interface. This starts with selecting a streamline flow solution of the problem that corresponds to the initial state of the stability analysis. In this stage, the first component of the interface is given by equation (3.47).

The ratio of the viscosities of the fluids μ_R has a significant impact on the stability of the flood front evolution and hence on ultimate oil recovery by waterflooding. Decrease in μ_R leads to decrease in the volume of oil recovered due to growing instability of oil displacement by water.

The front evolution is unstable when $1 < \mu_R < 2$. That is, when the displacing fluid is less viscous than the displaced one, the interface between then evolves in an unstable manner. When $\mu_R < 1$, the Saffman-Taylor instability, also known as 'viscous fingering' occurs.

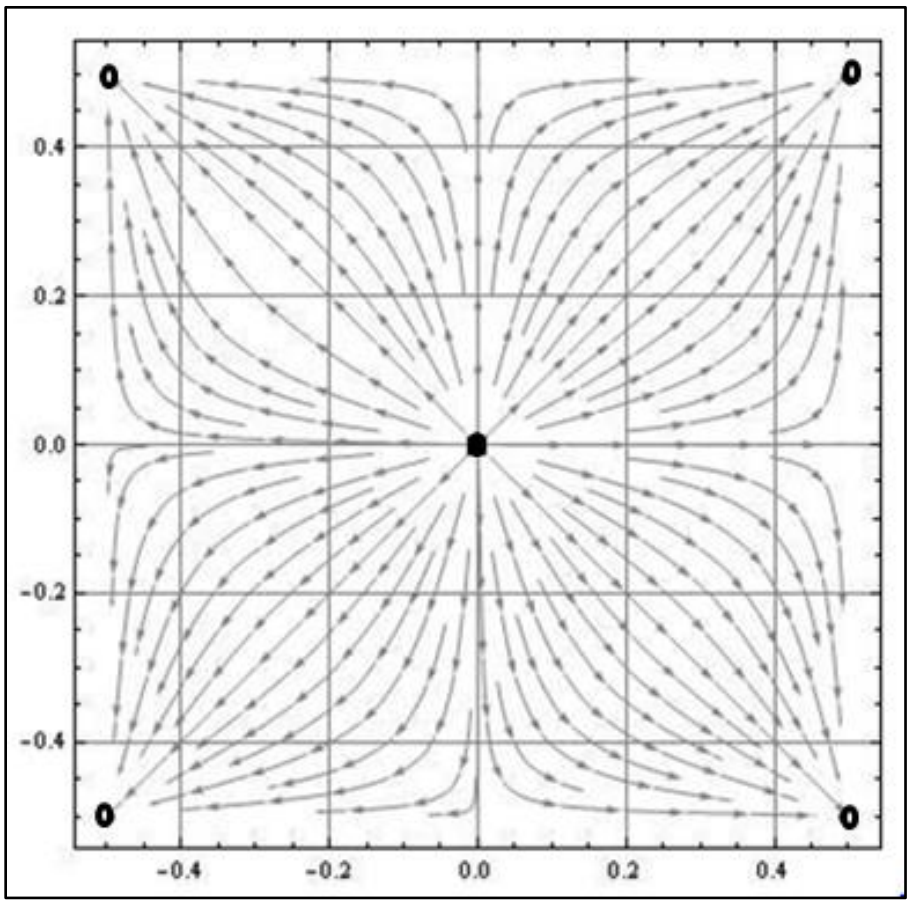

Fig. 4.12: Flow characteristics (streamlines) for five-spot flood pattern

4.7.2.1 Saffmam-Taylor instability

The result of simulation of the Saffman-Taylor instability, using the Weierstrass elliptic function method is shown. In this simulation the velocity field was determined in conjunction with the generalized Cauchy integrals for the resolution of a class of problems that can be reduced to the form of linear differential equations for the tangential and normal components of the velocity vectors, and for the movement of the oil-water interface, or oil-water contact (OWC).

The results that are presented refer to a viscous ratio $\mu_R = 0.4$. The average permeability used is 150 md. A constant injection rate of 0.2 ml/s in the normal direction of the left face of the reservoir core sample and recovery at the right face with the same direction and intensity was applied. A time scale equivalent to a time of order 10^6 was considered. Figure 4.13 shows the results obtained in the simulation for a five-spot waterflood pattern. This figure exhibits the front instabilities evolution and corresponds to the injection problem with viscosity ratio $\mu_R = 0.4$. The result shown in this figure correspond to the solution from the beginning up to the non-dimensional time $\tau = 0.21$.

4.7.2.2 Stationary fingers

At $t > 0$ an interface starts moving and generates a few modes which grow and compete together. The competition ends with a single finger occupying a part of the flow channel and moving steadily along it. The number of modes initially excited depends on the velocity of the interface. The number of modes increases more or less as the square root of the velocity, as predicted by the linear stability analysis.

Figure 4.13 also shows a time exposure with reference to a finger. The small particles that seed the fluid show two types of trajectories: some of them, originating far ahead, deviate as they approach the finger, and are further convected along its sides. Other particles converge towards the interface, swirl on a small scale as they come close to it, and are further convected backwards. Such motion shows the existence of a pair of small eddies at the tip. Few of the particles cross the interface and trap the film of oil left behind the finger.

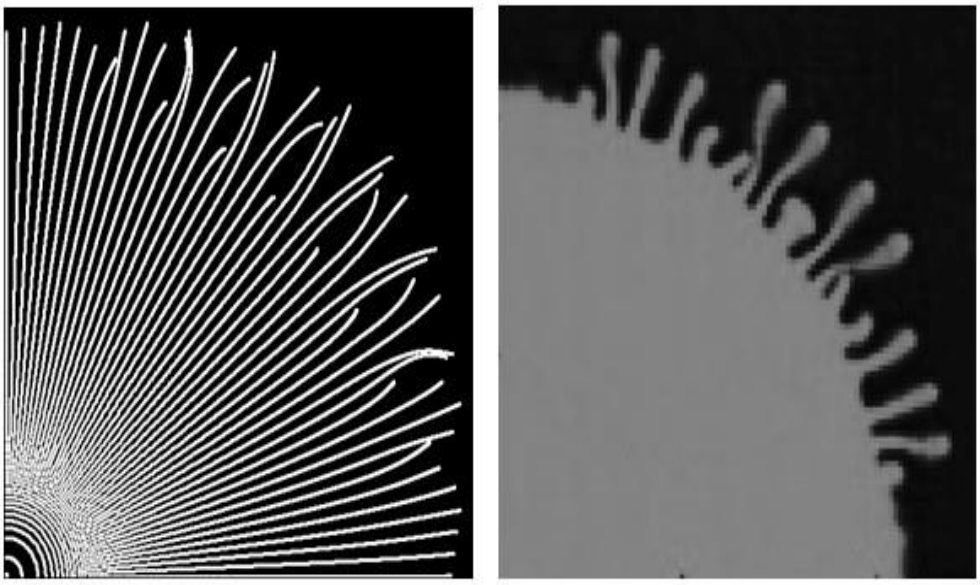

Fig. 4.13: Formation of viscous fingers (Saffman-Taylor instability) in a five-spot flood pattern. The diagram on the right is from Dapira et al. (1988) for comparison

4.7.3 Areal sweep

The areal sweep efficiency can be calculated from the equation:

$$E_A = \frac{A_{w,o}}{A_r} \tag{4.18}$$

where $A_{w,o}$ is the area covered by the injected and A_r is the area of the reservoir, determined from the grid geometry. Because of instability of the flood time resulting from viscous finging, which in turn leads to bypass of some areas in the reservoir, it is difficult to calculate the areal sweep efficiencyThe area of the reservoir swept by water in a five-spot pattern is simulated, with a viscosity ratio $\mu_R = 0.4$ and dimensionless time $\tau = 0.21$. Figure 4.13 shows the results obtained for $\mu_R = 0.4$ $\tau = 0.21$ (Figure 4.13a) and for $\mu_R = 0.4$ $\tau = 0.21$ (Figure 4.13b), respectively.

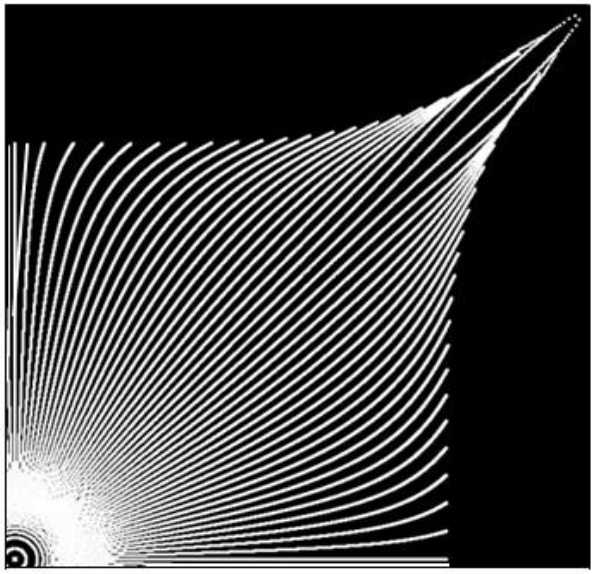

Fig. 4.14: Area of the reservoir swept by the injected water in five-spot pattern:
a) for $\mu = 0.4$ and $\tau = 0.21$ and, b) for $\mu = 0.25$ and $\tau = 0.125$, respectively

Figure 4.15 shows the path of the streamlines and the position of the OWC before breakthrough (a) and after breakthrough (b) of injected water into the production well for five-spot flood pattern

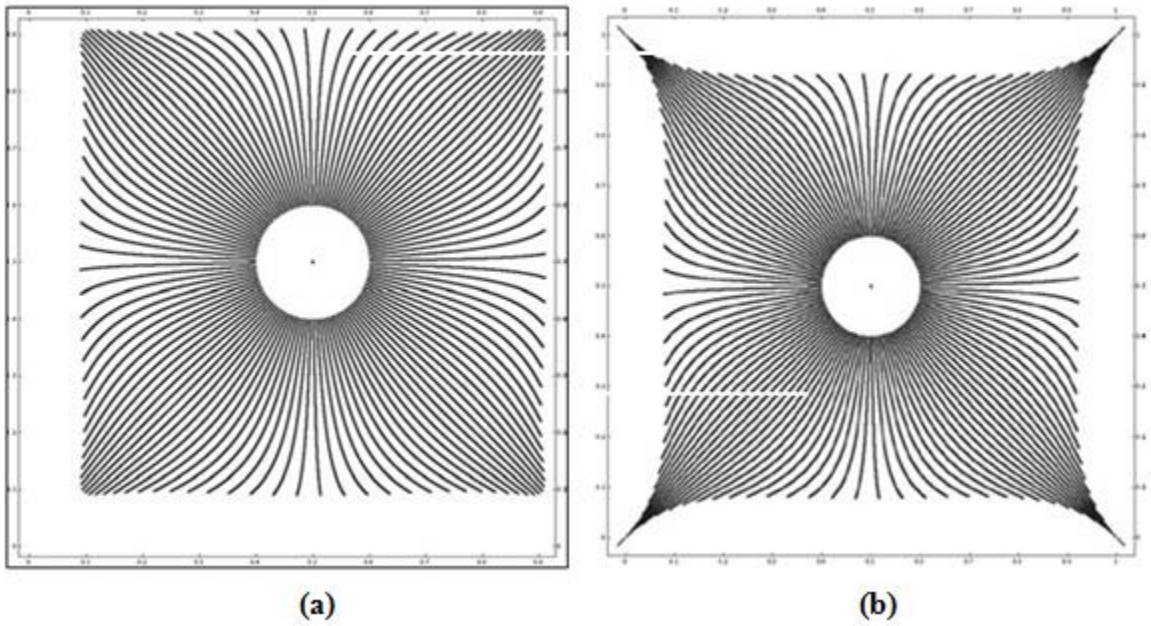

Fig. 4.15: OWC position before (a) and after (b) water breakthrough into the production well

Chapter 5

Conclusion and Recommendation

5.1 Conclusion

In this work, a description of the Niger Delta petroleum system is given and the materials and experimental procedures used in this research are described. A part of this research had earlier been published as “Fidelis O. Wopara, Sunny E. Iyuke, Abhijit Dandekar, Pore-Network Modeling and Prediction of Flow and Transport Properties in Porous Media. 37th International Symposium APPLICATION OF COMPUTERS AND OPERATIONS RESEARCH IN THE MINERAL INDUSTRY 23rd – 27th May 2015, Westmark Fairbanks Hotel & Conference Center, Fairbanks AK, USA pp. 952 – 961. The contributions of the author were experimental design, execution of all experimental procedures and writing of the article. Thus, this work covers the materials, equipment and the experimental procedures used during core preparation, core cleaning, porosity, permeability, wettability determination, core flooding, and rock image scanning.

A literature review of studies on pore network level of wettability effect on improved hydrocarbon recovery from petroleum reservoirs was carried out in this work. Also reviewed are works on micro-CT imaging of porous rocks and simulation of petroleum reservoirs. The reviews were extended to the determination of the petrophysical properties of Agbada sandstone

reservoir, relationship between these properties and the rock wettability, waterflooding and oil recovery.

The petrophysical properties of the reservoir (porosity, absolute permeability, initial saturations and relative permeabilities) were obtained by a series of laboratory experiments, results of which are in close agreement with pore network values generated in this work. The wettability state of the reservoir was established by conventional laboratory core waterflooding procedure. Coreflooding experiments of core plug samples of the Agbada sandstone reservoir rock show trends of strong water-wetness. The effects of initial water saturation on oil recovery are also studied. After primary drainage the reservoir becomes oil-wet and as the initial water saturation increases oil recovery initially increases and then decreases. These results indicate that the Agbada petroleum system exhibits similar trends in petrophysical properties and in waterflood oil recovery, as seen in other well studied water-wet sandstone reservoir rocks.

Oil recovery from the reservoir was computed using the Buckley-Leverret fractional flow method. For a given set of oil/water relative permeability, if the relative permeability of water increases, the water saturation increases and the relative permeability of oil decreases. If the oil viscosity is high, then the fractional flow of water will increase, leading to early water breakthrough, viscous fingering and trapping of the oil phase. This results in low recovery efficiency. On the other hand, if the water viscosity is high, the fractional flow of water will decrease, resulting to late water breakthrough and improved recovery efficiency. This trend, which is characteristic of strong water-wet sandstone reservoirs, is seen in the Agbada reservoir. Oil recovery increases with increasing wettability index and decreasing water-wetness and

reaches a peak at slightly-neutral water-wetness - slightly oil-wetness, but starts declining as the system becomes more oil-wet. Thus optimal oil recovery from a strongly water-wet Agbada reservoir is obtained at slightly water-wet condition.

The use of Weierstrass elliptic functions for the simulation of waterflooding performance was proposed. The proposed model was tested on Wolfram Mathematic software for five-spot flood pattern. Streamline fluid flow and viscous fingering, dimensionless water breakthrough time, and pressure distribution within the drainage area and the reservoir can be simulated using the model.

5.2 Recommendation

In this work the Agbada reservoir rock was considered homogeneous and the sequential solution methods for computation and simulation of oil recovery are similar in several ways to the methods reported in the literature. The sensitivity of the model and numerical treatment adopted were not carried out because it lies out of the scope of this work. However, to realistically predict the behavior of a reservoir under any depletion process, it is most important to have adequate knowledge of the constitutive relationship between the variables that govern fluid flow in the system. In reality natural porous media are heterogeneous and multi-phase flow on the equilibrium between viscous, capillary and gravity forces. This equilibrium changes with physical location and time. Therefore this work recommends that:

1. More rock samples from various reservoirs within the Niger delta petroleum system should be studied for more characterization in terms of the petrophysical properties.

2. Computation and simulation of the waterflood recovery should be carried out, with the reservoir treated as a heterogeneous system.
3. Refining of the Weierstrass elliotic functions model to treat other waterflooding performance variables, such as mobility ratio, fractional flow of the phases, volume of oil recovered, volume of water injected at breakthrough.
4. Validation of results obtained from this model using other simulations such as the fully implicit solution method formulation.
5. A further study that incorporates the sensitivity of more Agbada sandstone reservoir rocks and fluid properties like oil, water and gas saturations, mobility ratio, and vertical permeability anisotropy on the performance of different well configurations should be carried out.

Nomenclature

$I_{w\text{-}o}$	Amott-Harvey Wettability Index to Water/Oil
P_c	capillary pressure
S_w	water saturation
S_{wi}	initial water saturation
S_{or}	residual oil saturation
RF	recovery factor
Φ	pressure potential
φ	porosity
ρ	density
mD	milli Darcy
cP	centi Poise
p_i	initial pressure
p_{wf}	bottomhole flowing pressure
k_{rw}	water relative permeability
k_{ro}	oil relative permeability
∂P	delta pressure, differential pressure
μ	viscosity
σ	interfacial tension
λ	phase mobility
M	mobility ratio
M_s	shock front mobility ratio
WI	well index
OIIP	oil initially in place
r_w	wellbore radius
r_o	equivalent wellblock radius
WOR	water-oil ratio
Bo	formation volume factor
∇	(del) differential operator

References

Abou-Kassem, J. H., (1996). Practical considerations in developing numerical simulators for thermal recovery. Journal of Petroleum science & Engineering. V. 15, pp. 281-290.

Abreu, E., (2014). Numerical modeling of three phase immiscible flow in heterogeneous porous media with gravitational effects, Mathematics and Computers in Simulation, 97, 234-259.

Adler, P. M., Jacquin, C. G., Quiblier, J. A., (1990). Flow in simulated porous media. Int J Multiphase Flow; 16:691–712.

Adler, P. M., Jacquin, C. G., Thovert, J. F., (1992). The formation factor of reconstructed porous media. Water Resources Res, 28:1571– 6.

Agbalaka, C., Dandekar, A., Patil, S., Khataniar, S., Hemsath, J., (2009). Coreflooding Studies to Evaluate the Impact of Salinity and Wettability on Oil Recovery Efficiency. Transport in Porous Media, vol. 76, no. 1, pp. 77- 94.

Al-Dhahli, A., Geiger, S., vanDijke, M. I. J., (2011). Three-phase pore-network modelling for mixed-wet carbonate reservoirs, paper SPE 147991 presented at SPE Reservoir Characterisation and Simulation Conference and Exhibition, Soc. of Pet. Eng., Abu Dhabi, 9–11 Oct.

Al-Futaisi, A., Patzek, T. W. (2003). Impact of wettability alteration on two-phase flow characteristics of sandstones: a quasi-static description. Water Res. Res. 39, 1042–1054.

Allen III, M., B., Behie, B., Trangenstein, G. A., (1988). Multiphase flow in porous media. Springer-Verlag, London, 308p.

Allen, M. B., Furtado, F. (1997). Computational Methods for Porous Media Flows, in Fluid Transport in Porous Media, edited by J. P. du Plessis, Computational Mechanics Publ., Southampton.

Al-Raoush, R. I. (2009). Impact of Wettability on Pore-Scale Characteristics of Residual Nonaqueous Phase Liquids, *Environ. Sci. Technol.*, *43* (13), pp 4796–4801.

Amaefule, J. O., Altunbay, M., Tiab, D., Kersey, D., Keelan, D., (1993). Enhanced Reservoir Description: Using Core and Log Data to Identify Hydraulic (Flow) Units and Predict Permeability in Uncored Intervals/Wells. Paper SPE 26436.

Amott, E., (1959). Observations Relating to the Wettability of Porous Rock; Trans., AIME, v.216, pp. 156-62.

Anderson, R. N., Boulanger, A., He, W., Winston, J., Xu, L., Mello, U., Wiggins, W., (2004). Petroleum reservoir simulation and characterization system and method. US. Patent No. 6826483 B1, 13p, USA.

Anderson, W. G. (1987a). Wettability literature survey—part 4: the effects of wettability on capillary pressure. J. Petrol. Tech. 39, 1283–1300.

Anderson, W. G. (1987b). Wettability literature survey—part 5: the effects of wettability on relative permeability. J. Petrol. Technol. 39, 1453–1468.

Armstrong, R. T., Evseev, N., Koroteev, D., Berg, S., (2015). Modeling the velocity field during Haines jumps in porous media. Advances in Water Resources, 77; pp 57–68

Arns, C.H., Knackstedt, M.A., Pinczewski, W.V., Martys, N. (2004). Virtual permeametry on microtomographic images. J. Petrol. Sci. Eng. 45, 41–46.

Arns, J., Arns, C.H., Sheppard, A.D., Sok, R.M., Knackstedt, M.A., Pinczewski, W.V. (2003). Relative permeability from tomographic images; effect of correlated heterogeneity. J. Petrol. Sci. Eng. 39, 247–259.

Astafev, V. I,. Kasatkin, A. E. (2016). Modeling and numerical calculation of waterflooding using Weierstrass elliptic functions. International Journal of Mechanics, Vol 10

Astafev, V. I,. Roters, P. V. (2014). Simulation of oil recovery using Weierstrass elliptic functions. International Journal of Mechanics, Vol 8, pp 353 - 364

Aziz, K.; Settari, A., (1979). Petroleum reservoir simulation. Applied Science Publishers, London, 476p.

Babin, P., DellaValle, G., Dendievel, R., Lourdin, D., Salvo, L., (2007). X-ray tomography study of the cellular structure of extruded starches and its relations with expansion phenomenon and foam mechanical properties. Carbohydrate Pol 68:329-40.

Bear, J. (1953). Modeling flow and contaminant transport in fractured rocks. In: Bear J, Tsang C, deMarsily G. editions. Flow and contaminant transport in fractured rocks. San Diego, CA: Academic Press; 1993.

Behrooz Raeesi, B., Piri, M. (2009). Journal of Hydrology, Volume: 376, Issue: 3-4, Pages: 337-352

Berg, S., Ott, H., Klapp, S. A, Schwing, A., Neiteler, R., Brussee, N., Makurat, A., Leu, L., Enzmann, F., Jens-Oliver Schwarz, J.O., Michael Kersten, M., (2013). Real-time 3D imaging of Haines jumps in porous media flow. Proc Natl Acad Sci U S A. 5; 110(10): 3755–3759

Berkowitz, B., Balberg, I. (1993). Percolation theory and its application to groundwater hydrology. Water Resources Res, 29(34):775-94.

Bhatnagar, P. L., Gross, E. P., Krook, M., (1954). A model for collision processes in gases. I: small amplitude processes in charged and neutral one-component system. Phys. Rev. 94:511–525

Biswal B, Manwart C, Hilfer R, Bakke S, Øren PE., (1999). Quantitative analysis of experimental and synthetic microstructures for sedimentary rock. Physica A; 273:452–75.

Blunt, M. J. (1997). Effects of heterogeneity and wetting on relative permeability using pore level modeling. SPE J, 2:70-87.

Blunt, M. J. (1998). Physically-based network modeling of multiphase flow in intermeiate-wet porous media. J Petroleum Sci Eng., 20:117-25.

Blunt, M. J. (2001). Flow in porous media – pore-network models and multiphase flow. Curr Opinion Colloid Interf Sci., 6:197-207.

Blunt, M. J., Jackson, M. D., Piri, M; Valvatne, P. H., (2002). Detailed physics, predictive capabilities and macroscopic consequences for pore-network models of multiphase flow. Advances in Water Resources, 25(8-12):1069–1089.

Blunt, M. J., King, P. (1991). Relative permeabilities from two- and three-dimensional pore-scale network modeling. Transport Porous Med., 6:407-33.

Blunt, M. J., King, P., (1990). Macroscopic parameters from simulations of pore scale flow. Phys Rev A 42(8):4780–7.

Blunt, M. J., King, P., (1991). Relative permeabilities from two- and three- dimensional pore-scale network modelling. Transport Porous Med 6:407–33.

Bonner, B. P., Roberts, J. J., Schneberk, D. J. (1994). Determining water content and distribution in reservoir graywacke from the northeast Geysers with X-ray computed tomography. Geotherm. Resour. Coun. Trans., Vol.18, pp.305-310.

Brooks, R. H., Corey, A. T., (1964). Hydraulic Properties of Porous Media, Hydrology Papers No. 3, Colorado State University.

Bryant, S. L, Mellor, D. W., Cade, C. A. (1993). Physically representative network models of transport in porous media. AIChE J; 39(3):387–96.

Bryant, S. L., Blunt, M. J., (1992). Prediction of relative permeability in simple porous media. Phys Rev A; 46:2004–11.

Bryant, S. L., King, P. R., Mellor, D. W., (1993). Network model evaluation of permeability and spatial correlation in a real random sphere packing. Transport Porous Med; 11: 53–70.

Bryant, S. L., Raikes, S. (1995). Prediction of elastic wave velocities in sandstones using structural models. Geophysics; 60(2):437-46

Buckley, J. S., Bousseau, C., Liu, Y., (1996). Wetting Alteration by Brine and Crude Oil: From Contact Angles to Cores. SPE Journal, 1:341-350.

Buckley, J. S., Liu, Y., (1998). Some mechanisms of crude oil/brine/solid interactions. J. Petroleum Sci. and Eng. 20:155- 160.

Buckley, J. S., Liu, Y., Monsterleet, I. (1998). Mechanisms of wetting alteration by crude oils. SPE J, 3:54-61.

Buckley, S.E. Leverett, M. C. (1942). Mechanism of Fluid Displacement in Sands. Trans., AIME 146, 187–196.

Caubit, C., Bertin, H., Hamon, G., (2004). Three-phase flow in porous media: wettability effect on residual saturations during gravity drainage and tertiary waterflood. In: SPE 90099, proceedings of the SPE annual technical conference and exhibition, Houston, Texas, USA.

Chang, Y. C., Mohanty, K. K. (1997). Scale-up of two-phase flow in heterogeneous porous media, Journal of Petroleum Science and Engineering, 18, pp. 21-34.

Chatzis, I., Morrow, N., (1984). Correlation of Capillary Number Relationships for Sandstone, Society of Petroleum Engineers Journal, vol. 24, no. 5, pp. 555-562.

Chen, F., Xu, A., Zhang, G., Wang, Y., (2014). Two dimensional MRT LB model for compressible and incompressible flows. Front. Phys., 9(2): 246–254.

Chen, M. R., Hinkley, R. E., Killough, J. E. (1996). Computed tomography imaging of air sparging in porous media. Water Resour. Res., Vol.32, pp.3013-3024.

Chen, S., Doolen, G. D., (1998). Lattice Boltzmann Method for Fluid Flows, Annual Review of Fluid Mechanics, vol. 30, no. 1, pp. 329-364.

Christie, M. A. (2001). Flow in porous media - scale up of multiphase flow, Current Opinion in Colloid & Interface Science, 6, pp. 236-241.

Clemens, T., Tsikouris, K., Buchgraber, M., Louis M. Castanier, M. L., Anthony Kovscek, A., (2013). Pore-Scale Evaluation of Polymers Displacing Viscous Oil-Computational-Fluid-Dynamics Simulation of Micromodel Experiments, SPE-154169-PA, 16(02).

Coehlo, D., Thovert, J. F., Adler, P. M., (1997). Geometrical and transport properties of random packings of spheres and aspherical particles. Phys Rev E;55:1959–78.

Coles, M. E., Spanne, P., Muegge, E. L., Jones, K. W. (1994). Computed micro-tomograpy of reservoir core samples. Proceedings of the International SCA Meeting. Stavanger.

Coutinho, B. G., (2002) Numerical Solution for Problems of Petroleum Reservoirs Using Generalized Coordinates, Master Dissertation, Federal University of Campina Grande, Brazil. (In Portuguese)

Craft, B.C., Hawkins, M. Revised by Terry, R. E. (1991). Applied Petroleum Reservoir Engineering, Prentice Hall, pp.1-6.

Cunha, A. R., (1996). A Methodology to Three Dimensional Numerical Simulation of Petroleum Reservoirs Using Black-Oil Model and Mass Fraction Formulation, Master Dissertation, Federal University of Santa Catarina, Brazil. (In Portuguese)

Cunha, A. R., Maliska, C. R., Silva, A. F. C., Livramento, M. A., (1994). Two-Dimensional Two-Phase Petroleum Reservoir Simulation Using Boundary-Fitted Grids, Journal of the Brazilian Society of Mechanical Sciences, Vol. XVI, no. 4, pp. 423-429.

Czesnat, A. O., Maliska, C. R., Silva, A. F. C., Lucianetti, R. M., (1998). Grid Effects on petroleum reservoir simulation using boundary- fitted generalized coordinates, VII ENCIT, Rio de Janeiro, Brazil. (In Portuguese)

Dandekar, A., (2013). Petroleum Reservoir Rock and Fluid Properties, Second Edition, Gulf Publishing Company.

Dandekar, A., Patil, S., Shataniar, S. (2008). Characterization and Alteration of Wettability States of Alaskan Reservoirs to Improve Oil Recovery Efficiency (including the within-scope expansion based on Cyclic Water Injection – a pulsed waterflood for Enhanced Oil Recovery). Final report submitted to United States Department of Energy National Energy Technology Laboratory.

Dehkordi, M.M., and Manzari M.T., (2013). A multi-resolution multiscale finite volume method for simulation of fluid flows in heterogeneous porous media, Journal of Computational Physics, 248, 339-362

DiCarlo, D. A., Sahni, A., Blunt, M. J. (2000). The effect of wettability on three-phase relative permeability. Transport Porous Med., 39:347-66.

Dicks, E. M. (1993). Higher Order Godunov Black-oil Simulations for Compressible Flow in Porous Media, PhD Thesis submitted to University of Reading, Reading, UK

DiDonato, G.; Tavassoli, Z.; Blunt, M. J., (2006). Analytical and numerical analysis of oil recovery by gravity drainage. Journal of Petroleum Scinece & Engineering. V. 54, pp. 55-69.

Dillard, L. A., Blunt, M. J. (2000). Development of a pore network simulation model to study nonaqueous phase liquid dissolution. Water Resources Res, 36(2):439-54.

Dixit, A. B., Buckley, J. S., McDougall, S. R., Sorbie, K. S. (2000). Empirical measures of wettability in porous media and the relationship between them derived from pore-scale modeling. Trans. Porous Media 40, 27–54.

Dixit, A. B., McDougall, S. R., and Sorbie, K.S., (1997). Pore-level investigation of relative permeability hysteresis in water-wet systems," SPE 37233, Proceedings of the 1997 SPE International Symposium on Oilfield Chemistry, Houston.

Dixit, A. B., McDougall, S. R., Sorbie, K. S, Buckley, J. S. (1999). Pore-scale modeling of wettability effects and their influence on oil recovery. SPE Reservoir Evaluation Eng., 2:25-36.

Dong, H., Blunt, M., (2009). Pore-network extraction from micro-computerized- tomography images,‖ Physical Review E, 036307, vol. 80, no. 3.

Doust, H., Omatsola, E. (1990): Niger Delta, in , Edwards, J. D., and Santogrossi, P.A., eds., Divergent/passive Margin Basins, AAPG Memoir 48: Tulsa, American Association of Petroleum Geologists, 239-248.

Dunsmuir, J. H., Ferguson, S. R, Damico, K. L., Stokes, J. P. (1991). X-ray microtomography: a new tool for the characterization of porous media. In: Paper SPE 22860, Proceedings of the SPE Annual Meeting, Dallas, TX .

Escobar, F. H.; Ibagn, O. E.; Montealegre-M., M., (2007). Average reservoir pressure determination for homogeneous and naturally fractured formations from multi-rate testing with the TDS technique. Journal of Petroleum Science & Engineering. V. 59, pp. 204-212.

Falode, O., Manuel, E., (2014). Wettability Effects on Capillary Pressure, Relative Permeability, and Irreducible Saturation Using Porous Plate, Journal of Petroleum Engineering, Vol. 2014, Article ID 465418, 12 pages

Fatemi, S. M., Sohrabi, M., (2013). Recovery Mechanisms and Relative Permeability for Gas/Oil Systems at Near-Miscible Conditions: Effects of Immobile Water Saturation, Wettability, Hysteresis, and Permeability. Energy Fuels, 27 (5), pp 2376–2389

Fatt, I., (1956). The network model of porous media I. Capillary pressure characteristics. Trans AIME, 207:144-59.

Fatt, I., (1956). The network model of porous media II. Dynamic properties of a single size tube network. Trans AIME, 207:160-3.

Fatt, I., (1956). The network model of porous media III. Dynamic properties of networks with tube radius distribution. Trans AIME, 207:164-81.

Fenwick, D. H., Blunt, M. J., (1998). Three-dimensional modeling of three- phase imbibition and drainage. Adv Water Resources, 21(2):121–43.

Fischer, U., Celia, M. A., (1999). Prediction of relative and absolute permeabilities for gas and water from soil water retention curves using a pore-scale network model. Water Resour Res; 35(4): 10891100.

Fletcher, C. A. J., (2003). Computational techniques for fluid dynamics. V. 2, Springer, Berlin, Germany, 2.ed.

Geffen, T. M., Parrish, D. R., Dean, G. W., Morse, R, A., (1952). Efficiency of gas displacement from porous media by liquid flooding,‖ Trans. AIME, vol. 195, pp. 29-38.

Gharbi, R. B. C., (2004). Use of reservoir simulation for optimizing recovery performance. Journal of Petroleum Science & Engineering. V. 42, pp. 183-194.

Ghoodjani, E., Bolouri, S. H., (2014). A Laboratory Study of Gas-oil Relative Permeability during CO_2 Injection, Energy Sources, Part A: Recovery, Utilization, and Environmental Effects, 36(17): pp 1857-1864

Giting, V. E., (2004). Computational up-scaled modeling of heterogeneous porous media flow utilizing finite element method. PhD. Thesis, Texas A & M University, USA. 148p.

Grader, A. S., Clark, A. B S., Al-Dayyani, T., Nur. A., (2009). Computations of porosity and permeability of sparic carbonate using multi-scale ct images. Paper for presentation at the International Symposium of the Society of Core Analysts held in Noordwijk aan Zee, The Netherlands.

Grader, A. S., Nur, A., Baldwin, C., Diaz, E., (2010). Multi-Scale Imaging Process for Computations of Porosity and Permeability from Carbonate Rocks. Adapted from oral presentation at AAPG Convention, New Orleans, Louisiana.

Granet, S., Fabrie, P.; Lemonnier, P.; Quintard, M., (2001). A two-phase simulation of a fractured reservoir using a new fissure element method. Journal of Petroleum Science & Engineering. V. 32, pp. 35-52.

Grant, P., Anderson, W., (1988). Core Cleaning for Restoration of Native Wettability: SPE 14875.

Gunstensen, A., Rothman, D. (1991). Lattice Boltzmann Model of Immiscible Fluids, Phys. Rev. A, 43, pp 4320.

Hazlett, R. D. (1995). Simulation of capillary-dominated displacements in micro-tomographic images of reservoir rocks. Transport Porous Med., 20:21-35.

Heiba, A. A., Davis, H. T., Scriven, L. E. (1983). Effect of Wettability on Two-Phase Relative Permeability and Capillary Pressures, SPE paper 12172. Proceedings of the SPE Annual Technical Conference and Exhibition, San Francisco.

Heiba, A. A., Sahimi, M., Scriven, L. E., Davis, H. J., (1992). Percolation theory of two-phase relative permeability. SPE Reservoir Eng.; 7:123132.

Hirasaki, G. J., O'Dell, P. M., (1970). Representation of Reservoir Geometry for Numerical Simulation, Society Petroleum Engineers Journal, V. 10, n. 4, pp. 393-404.SPEJ.

Honarpur, M., Koederitz, L., H. Harvey, A. H., (1986). Relative Permeability of Petroleum Reservoirs, CRC Press.
http//www.wou.edu/las/physci/taylor/es486.../li_etal_2014_resistivity.pdf

http://www.searchanddiscovery.com/pdfz/documents/2010/40581grader/ndx_grader.pdf.html

Hughes, R. G., Blunt, M. J., (1999). Pore-scale modeling of multiphase flow in fractures and matrixfracture transfer. SPE 56411. Proceedings of the SPE Annual Conference and Exhibition, Houston.

Hui, M. H., Blunt, M. J. (2000). Effects of wettability on three-phase flow in porous media. J Phys Chem B, 104:3833-45.

Hui, M., Durlofsky, L. J., (2005). Accurate coarse modeling of well-driven, high-mobility-ratio displacements in heterogeneous reservoirs. Journal of Petroleum Science & Engineering. V. 49, pp. 37-56.

Jackson, M. D., Valvatne, P. H., Blunt, M. J. (2003). Prediction of wettability variation and its impact on flow using pore- to reservoir-scale simulations. J. Petrol. Sci. Eng. 39, 231–246.

Jadhunandan, P. P. (1990). Effects of brine composition, crude oil and ageing conditions on wettability and oil recovery. PhD Thesis, New Mexico Inst. of Mining and Technology, New Mexico.

Jadhunandan, P. P., Morrow, N. R. (1995). Effect of wettability on waterflood recovery for crude-oil brine rock systems. SPE Reservoir Eng. 10, 40–46.

Jerauld, G. R., (1997). Prudhoe Bay Gas/Oil Relative Permeability,‖ SPE Reservoir Engineering, vol. 12, no. 1, pp. 66-73.

Jerauld, G. R., Rathmell, J .J. (1994). Wettability and Relative Permeability of Prudhoe Bay: A Case Study in Mixed-Wet Reservoirs, paper SPE 28576 presented at the SPE Annual Technical Conference and Exhibition, New Orleans, Louisiana.

Jerauld, G. R., Salter, S. J. (1990). The effect of pore-structure on hysteresis in relative permeability and capillary pressure: pore-level modeling. Transport Porous Med., 5:103-30.

Jia, C., Shing, K., Yortsos, Y. C., (1999). Advective mass transfer from stationary sources in porous media. Water Resour Res. 35 11:32393251.

Jia, C., Shing, K., Yortsos, Y. C., (1999). Visualization and simulation of NAPL solubilization in pore networks. J Contam Hydrol. 35(4): 363387.

Jia, X., Williams, R. A., (2001). A packing algorithm for particles of arbitrary shapes. Powder Technology, 120, 3, p 175-186.

Kak, A. C., Slaney, M., (2001). Principles of Computerized Tomographic Imaging, Society of Industrial and Applied Mathematics, http://www.slaney.org/pct/pct-toc.html

Karabakal, U., Bagci, S. (2004). Determination of Wettability and Its Effect on Waterflood Performance in Limestone Medium, *Energy Fuels*, *18* (2), pp 438–449

Kasiri., Bashiri, A., (2011). Wettability and Its Effects on Oil Recovery in Fractured and Conventional Reservoirs, Petroleum Science and Technology, 29(13): 1324-1333

Katz, A., Friedman, G. M., (1965). The preparation of stained acetate peels for the study of carbonate rocks: 1965.

Kleppe, J., Delaplace, P., Lenormand, R., Hamon, G., Chaput, E., (1997). Representation of Capillary Pressure Hysteresis in Reservoir Simulation,‖ in Proceedings of SPE Annual Technical Conference and Exhibition, SPE Paper 38899, San Antonio, Texas, USA.

Koiter W.T. (1959). Some general theorems on doubly-periodic and quasi-periodic functions, Proc. Konikl. Nederl. Akademie Wetenschappen, Amsterdam, Vol. 62, no. 2, pp. 120–128.

Koplik, J., (1982). Creeping flow in two-dimensional networks. Journal of Fluid Mechanics. 119 : p. 219-247.

Koplik, J., Lasseter, T. J. (1985). Two-phase flow in random network models of porous media. SPE Journal, 25: p 89 - 100.

Kovscek, A. R., Wong, H., Radke, C. J. (1993). A pore-level scenario for the development of mixed wettability in oil reservoirs. AIChE J. 39, 1072–1085.

Kulke, H. (1995). Nigeria, in, Kulke, H., ed., Regional Petroleum Geology of the World. Part II: Africa, America, Australia and Antarctica: Berlin, Gebrüder Borntraeger, 143-172.

Land, C., (1971). Comparison of Calculated with Experimental Imbibition Relative Permeability, Society of Petroleum Engineers Journal, vol. 11, no. 4, pp. 419-425.

Latham, P. E., Richmond, B. J., Nelson, P. G., Nirenberg, S. N. (2000). Intrinsic dynamics in neuronal networks. I. Theory. J. Neurophysiol. 83: 808–827.

Lenormand, R., Zarcone, C., Sarr, A. (1983). Mechanisms of the displacement of one fluid by another in a network of capillary ducts. J Fluid Mech., 135:337-53.

Li, K., Shapiro, M., Horne, R. N., Ma, S., Hajari A., Mudhhi, M., (2014). In situ estimation of relative permeability from resistivity measurements

Lin, C., Cohen, M. H. (1982). Quantitative methods of microgeometric modeling. J Appl Phys, 53:4152.

Liu, H., Zhang, Y., Valocchi, A. J., (2015). Lattice Boltzmann simulation of immiscible fluid displacement in porous media: Homogeneous versus heterogeneous pore network, PHYSICS OF FLUIDS 27, 052103.

Lowery, M. I., Miller, C. T. (1995). Pore-scale modeling of nonwetting-phase residual in porous media. Water Resources Res, 31:455-73.

Lu, M.; Connell, L. D., (2007). A model for the flow of gas mixtures in adsorption dominated dual porosity reservoirs incorporating multi- component matrix diffusion. Part I. Theoretical development. Journal of Petroleum Scinece & Engineering. V. 59, pp. 17-26.

Lu, Q, Peszynska M. & Wheeler F., (2001). A Parallel Multi-Block Black-Oil Model in Multi-Model Implementation, Paper SPE 66359, 2001 SPE Reservoir Simulation Symposium.

Ma, S. M., Belowi, A., Pairoys, F., Zoukani, A., (2013). Quality Assurance of Carbonate Rock Special Core Analysis - Lesson Learnt from a Multi-Year Research Project. IPTC: International Petroleum Technology Conference. Engineering and Thermal Sciences and Latin American Congress of Heat and Mass Transfer(ENCIT - LATCYM), Florianpolis, SC. v.3. pp. 1477-1482.

Ma, T D., Youngren, G. K., (1994). Performance of Immiscible Water- Alternating-Gas (IWAG) Injection at Kuparuk River Unit, North Slope, Alaska, in Proceedings of SPE Annual Technical Conference and Exhibition, SPE Paper 28602, New Orleans, Louisiana, U.S.A.

Madalena, M. D., Payatakes, A. C. (1986). Network models for two-phase flow in porous media Part 1. Immiscible microdisplacement of non-wetting fluids. Journal of Fluid Mechanics, 164 : pp 305-336

Mago, A. L., (2006). Adequate description of heavy oil viscosities and a method to assess optimal steam cyclic periods for thermal reservoir simulation. Master Thesis, Texas A & M University, USA. 79p.

Maliska, C. R., (2004). Computational Heat Transfer and Fluid Mechanics, LTC, Rio de Janeiro, Brazil. (In Portuguese)

Maliska, C. R., Silva, A. F. C., Juc, P. C., Cunha, A. R., Livramento, M. A., (1993). Desenvolvimento de um Simulador 3D Black-oil em Coordenadas Curvil´ıneas Generalizadas - PARTE I, Relatrio CENPES/PETROBR ´AS, SINMEC/EMC/UFSC, Relatrio RT-93-1, Florianpolis, SC, Brasil.

Marcondes, F., (1996). Numerical Simulation Using Implicit-Adaptative Mehotds and Voronoi Meshs in Problems of Petroleum Reservoirs. PhD. Thesis, Departament of Mechanical Engineering, Federal University of Santa Catarina, Brazil. (In Portuguese)

Marcondes, F., Maliska, C. R. & Zambaldi, M. C., (1996). Soluo de Problemas de Reservatrios de Petrleo: Comparao entre as Metodologias TI, IMPES e AIM, VI Brazilian Congress of

Martins, M.A., Valle, R.M., Oliveira, L.S., (2000). Fundamental of Finite Volume Discretization of the Conservation Equations using Structured and Unstructured Meshes, 21st. Iberian Latin-American Congress on Computational Methods in Engineering, Rio de Janeiro.

Matus, E. R., (2006). A top-injection bottom-production cyclic steam stimulation method for enhanced heavy oil recovery. Master Thesis, Texas A & M University, USA. 81p.

McDougall, S. R., Sorbie, K. S. (1995). The impact of wettability on waterflooding - pore-scale simulation. SPE Reservoir Eng. 10, 208–213.

McDougall, S. R., Sorbie, K. S. (1997). The application of network modelling techniques to multiphase flow in porous media. Petrol. Geosci. 3, 161–169.

Miguel de la Cruz, L., Monsivais, D., (2014). Parallel numerical simulation of two-phase flow model in porous media using distributed and shared memory architectures, Geofísica Internacional , 53(1), 59-75.

Morrow, N. R. (1975). The effect of surface roughness on contact angle with special reference to petroleum recovery. J Can Pet Technol., 14:42-53.

Morrow, N. R., (1990). Wettability and its Effect on Oil Recovery, J. Petroleum Technol., 42:1476-1484.

Morrow, N. R., Cram, P. J., McCaffrey, F. G. (1973). Displacement Studies in Dolomite with Wettability Control by Octanoic Acid, SPEJ); Trans., AIME, 255, 221–232.

O'Carroll, D. M., Mumford, K. G., Abriola, L. M., Gerhard, J. I., (2010). Influence of wettability variations on dynamic effects in capillary pressure, Water Resour. Res., 46(8), W08505, doi:10.1029/2009WR008712.

Oak, M. J., Baker, L., Thomas, D., (1990). Three-Phase Relative Permeability of Berea Sandstone, Journal of Petroleum Technology, vol. 42, no. 8, pp. 1054-1061.

Ohtani, T., Nakashima, Y., and Muraoka, H. (in press). Three-dimensional miarolitic cavity distribution in the Kakkonda granite from borehole WD-1a using X-ray computerized tomography. Eng. Geol.

Ohtani, T., Nakashima, Y., Muraoka, H., (1997). Three- dimensional imaging of textures in the Kakkonda granite using X-ray CT. Jnl. Geotherm. Res. Soc. Japan, Vol.19 (4), pp.209-216 (in Japanese with English abstract).

Øren, P. E, Bakke S, Arntzen O. J., (1998). Extending predictive capabilities to network models. SPE J; 3:324-336.

Øren, P. E., Bakke, S. (2003). Reconstruction of Berea sandstone and pore--scale modeling of wettability effects. J. Petrol. Sci. Eng. 39, 177–199.

Øren, P., Bakke, S., (2002).Process Based Reconstruction of Sandstones and Prediction of Transport Properties, Transport in Porous Media, vol. 46, pp. 311-343.

Parsaei, R., Chatzis, I. (2011). Experimental Investigation of Production Characteristics of the Gravity-Assisted Inert Gas Injection (GAIGI) Process for Recovery of Waterflood Residual Oil: Effects of Wettability Heterogeneity, *Energy Fuels*, *25* (5), pp 2089–2099

Parvazdavani, M., Masihi, M., Ghazanfari, M. H., (2013). Gas–oil relative permeability at near miscible conditions: An experimental and modeling approach, Scientia Iranica, 20(3): Pp 626–636

Peaceman, D. W., (1978). Interpretation of well-block pressures in numerical reservoir simulation. SPEJ 253, No. 2, 183–194.

Pickell, J. J., Swanson, B. F., Hickman, W. B., (1996). Application of Air- Mercury and Oil-Air Capillary Pressure Data In the Study of Pore Structure and Fluid Distribution,‖ Society of Petroleum Engineers Journal, vol. 6, no. 1, pp. 55-61.

Piller, M., Casagrande, D., Schena, G., Santini, M., (2014). Pore-scale simulation of laminar flow through porous media. Journal of Physics: Conference Series 501, 012010

Pilotti, M., (2000). Reconstruction of clastic porous media. Transport Porous Med;41(3):359–64.

Piri, M., Blunt, M. J., (2005). Three-dimensional mixed-wet random pore-scale network modeling of two- and three-phase flow in porous media. II. Results, Physical Review E, vol. 71, no. 2, p. 026302.

Pollock, D. W. (1988). Semi-analytical Computation of Path Lines for Finite-Di erence Models, Ground Water, 26, No. 6, 743{750.

Prais, F., Campagnolo, E. A., (1991) Multiphase Flow Modeling in Reservoir Simulation. Proceedings of the XI Brazilian Congress of Mechanical Engineering (COBEM), So Paulo, SP.

Pusey, W.C., (1973). How to evaluate potential gas and source rocks: World oil, Vol 176, No 5, pp 71-75

Radike, G. A., Hadjiconstantinou, N. G., (2009). Variance-reduced particle simulation of the lattice-Boltzmann transport equation in the relaxation-time approximation. Physical Rev E79, 056711.

Raeesi, B., Piri, M., (2009). The effects of wettability and trapping on relationships between interfacial area, capillary pressure and saturation in porous media: A pore-scale network modeling approach. Journal of Hydrology, 376(3-4): pp 337-352

Rathmell, J. J., Braun, P. H., Perkins, T. K. (1973). Reservoir Waterflood Residual Oil Saturation from Laboratory Tests, JPT 25, 175–185.

Rezaveisi, M., Ayatollahi, S., Rostami, B., (2012). Experimental Investigation of Matrix Wettability Effects on Water Imbibition in Fractured Artificial Porous Media, Journal of Petroleum Science and Engineering

Rostami, B., Kharrat, R., C.Ghotbi, C., Alipour, T. V., (2008). Wettabilty Effect on Oil Recovery and Residual Saturation During Forced Gravity Drainage and Secondary Waterflood, A paper presented at the 10th International Symposium of Wettability and SCA held in Abu Dhabi, UAE.

Sahimi, M., (1995). Flow and transport in porous media and fractured rock: from classical methods to modern approaches. Weinheim:VHC.

Salathiel, R. A. (1973). Oil recovery by surface film drainage in mixed-wettability rocks. J. Petrol. Tech. 25, 1216–1224.

Shi, Y., Ying Wan Yap, Y. W., Sader, J. E., (2014). Lattice Boltzmann method for linear oscillatory no-continuum flows. Phys. Rev. E 89, 033305, 3.

Silin, D., Patzek, T., (2006). Pore space morphology analysis using maximal inscribed spheres, Physica A: Statistical and Theoretical Physics, vol. 371, no. 2, pp. 336-360.

Sorbie, K. S., Ryazanov, A. V., vanDijke, M. I. J., (2011). The structure of residual oil saturation as a function of wettability alteration using pore-scale network modelling, paper SCA2011-37 presented at International Symposium of the Society of Core Analysts, Austin, Texas.

Streng, M., (1996). Load Balancing for Computational Fluid Dynamics Calculations, in High Performance Computing Fluid Dynamics, ed. P.

Suekane, T., Nobuso, T., Hirai, S., Kiyota, M., (2008). Geological storage of carbon dioxide by residual gas and solubility trapping, International Journal of Greenhouse Gas Control, vol. 2, no. 1, pp. 58-64.

Suicmez, V. S., Piri, M., Blunt, M. J. (2008). Effects of wettability and pore-level displacement on hydrocarbon trapping. Advances in Water Resources, Vol. 31, Issue 3, pp 503-512.

Suzanne, K., Hamon, G., Billiotte, J., Trocme, V., (2003). Experimental Relationships Between Residual Gas Saturation and Initial Gas Saturation in Heterogeneous Sandstone

Reservoirs,‖ in Proceedings of SPE Annual Technical Conference and Exhibition, SPE Paper 84038, Denver, Colorado, U.S.A.

Tiab, D., Donaldson, E. C., (2004). Petrophysics: Theory and Practice of Measuring Reservoir Rock and Fluid Transport Properties. (2nd ed). USA: Elsevier, Inc., (Chapter 7) p.425.

Tivey, M. K., Singh, S. (1997). Nondestructive imaging of fragile sea-floor vent deposit samples. Geology, Vol.25, pp.931-934.

Todd, M. R., O'Dell, P. M., Hirasaki, G. J., (1972). Methods for Increas- ing Accuracy in Numerical Reservoir Simulators, Society of Petroleum Engineers Journal, V. 12, n. 6, pp. 515-530.

Torsæter, O., Abtahi, M., (2003). Experimental Reservoir Engineering, Laboratory Workbook. Dept. of Petroleum Eng. and Applied Geophysics, Norwegian University of Science and Technology , (Chapter 11).

Tsakiroglou, C. D., Payatakes, A. C., (2000). Characterization of the pore structure of reservoir rocks with the aid of serial sectioning analysis, mercury porosimetry and network simulation. Adv Water Resour, 23 7 :773789.

Tuller, M., Or, D., Dudley, I. M. (1999). Adsorption and capillary condensation in porous media: liquid retention and interfacial configurations in angular pores. Water Resources Res, 35(7):1949-64.

Tuttle, L. W. M., Charpentier, R. R., Brownfield, E., (1999). The Niger Delta Petroleum System: Niger Delta Province, Nigeria Cameroon, and Equatorial Guinea, Africa. U.S. Geological Survey Open-File Report 99-50-H, Denver, Colorado, 70 pp.

Unsal, E., Dane, J. H., Schwartz, P., Dozier, G. V., (2006). Displacement Properties of Immiscible Fluids in Porous Media, Journal Simulation, 82(8): pp 499-510

Vahid, S., Maša, P., Christoph, H., Arns, S., Bryant, L. S. (2010). Pore scale modeling of two-phase flow. XVIII International Conference on Water Resources, CMWR, Barcelona.

Valvatne, P .H., Blunt, M.J., (2004). Predictive pore-scale modeling of two-phase flow in mixed wet media, Water Resources Research, W07406, vol. 40, no. 7, p. 21.

Valvatne, P. H., (2004). Predictive pore-scale modelling of multiphase flow. PhD thesis, Imperial College London.

Van Der Vorst, H. A., (1992). BI-CGSTAB: A Fast and Smoothly Converging Variant of Bi-CG for the Solution of Nonsymmetric Linear Systems. SIAM Journal on Scientific & Statistical Computing, V. 13, n.2, pp. 631-644.

van Dijke M. I. J., McDougall, S., Sorbie, K. S., (2000). A process-based approach for three-phase capillary pressure and relative permeability relationships in mixed-wet systems, SPE 59310. Proceedings of the SPE DOE Symposium on Improved Oil Recovery, Tulsa

van Dijke M. I. J., Sorbie, K. S., McDougall, S., (2001). Saturation-dependencies of three-phase relative permeabilities in mixed- wet and fractionally-wet system. Adv Water Resour; 24:365384.

Vizika, O., Lombard, J.-M., 1996. Wettability and spreading: two key parameters in oil recovery with three-phase gravity drain- age. SPE Reservoir Eval. Eng., 54–60.

Wason, C. B.; King, G. A.; Shuck, E. L.; Breitenbach, E. A.; McFarlane, R. C., (1990). System for monitoring the changes in fluid content of a petroleum reservoir. US Patent No. 4969130,

Wesseling, K., Thiele, M. R., Batycky, R.P., Blunt, M. J., (1997). A Streamline-Based 3D Field-Scale Compositional Reservoir Simulator, SPE Journal, SPE 38889.

Whiteman, A. J., (1982). Nigeria, its petroleum, geology, resources and potential. v. I and II, Edinburgh, Graham and Trotman.

Zang, K., Wu, Y.S., Ding, C., Pruess, K., Elmroth, E., (2001). Parallel Computing Techniques for Large-Scale Reservoir Simulation of Multi-Component and Multiphase Fluid Flow, Paper SPE 66343, SPE Reservoir Simulation Symposium.

Zendehboudi, S., Rezaei, N., Chatzis, I. (2011). Effect of Wettability in Free-Fall and Controlled Gravity Drainage in Fractionally Wet Porous Media with Fractures, *Energy Fuels*, Article ASAP.

Zhao, X., Blunt, M. J., Yao, J. (2011). Pore-scale modeling: Effects of wettability on waterflood oil recovery, Journal of Petroleum Science and Engineering 71 169–178.

Zhou, X., Morrow, N.R., Ma, S., (2011). Interrelationship of Wettability, Initial Water Saturation, Aging Time and Oil Recovery by Spontaneous Imbibition and Waterflooding. SPE Journal, 5:199-207.

Appendices

Appendix A1: Porosity data, core dimensions and weights

Core ID	Diameter (cm)	Length (cm)	Bulk Volume (cm^3)	Dry Weight (g)	V_1 (cm^3)	V_2 (cm^3)	Grain Volume (cm^3)	Pore Volume (cm^3)	Porosity (%)
A_1	3.82	7.87	90.23	192.40	102.18	38.02	64.16	26.07	28.9
A_2	3.83	7.86	90.59	192.44	103.66	37.71	65.95	24.64	27.2
B_1	3.81	7.65	87.25	186.22	100.17	37.87	62.30	24.95	28.6
B_2	3.82	7.75	88.86	191.18	101.17	37.28	63.89	24.97	28.1
C_1	3.81	8.12	92.61	194.02	104.97	38.48	66.49	26.12	28.2
C_2	3.82	7.78	89.20	191.21	102.51	38.11	64.40	24.80	27.8
D_1	3.83	7.62	87.82	188.46	101.51	37.66	63.85	23.97	27.3
D_2	3.81	7.81	89.08	191.19	102.49	37.28	65.21	23.87	26.8
E_1	3.83	7.68	88.52	189.00	100.69	36.98	63.71	24.81	28.1
E_2	3.83	7.66	88.28	189.02	101.10	37.10	64.00	24.28	27.5
F_1	3.83	7.67	88.40	189.10	101.40	37.75	63.65	24.75	28.0
F_2	3.82	7.82	89.66	191.90	102.82	38.00	64.82	24.84	27.7

Appendix A2: Experimental relative permeability values

S_w	0.20	0.25	0.30	0.35	0.40	0.45	0.50	0.55	0.60	0.65	0.70	0.75	0.80
k_{rw}	0.00	0.002	0.008	0.021	0.034	0.052	0.075	0.100	0.130	0.168	0.208	0.250	0.301
k_{ro}	0.798	0.622	0.468	0.371	0.284	0.217	0.162	0.120	0.080	0.052	0.027	0.019	0.00

Appendix A3: Recovery efficiency versus water pore volume injected

Water pore vol. injected	0.0	0.5	1.0	1.5	2.0	2.5	3.0	3.5	4.0	4.5	5.0	5.5
Oil recovery factor	0.0	0.0	0.0	0.56	0.56	0.56	0.56	0.56	0.56	0.56	0.56	0.56
S_w	0.0	0.0	0.0	0.54	0.54	0.54	0.54	0.54	0.54	0.54	0.54	0.54
f_w	0.0	0.0	0.0	0.42	0.42	0.42	0.42	0.42	0.42	0.42	0.42	0.42

Appendix A4: Injection rate vs oil recovery

Water PV Injected	40 bb/hr	60 bbl/hr	20 bbl/hr
0	0	0	0
0.5	0.16	0.16	0.14
1	0.36	0.3	0.28
1.5	0.56	0.5	0.4
2	0.58	0.54	0.42
2.5	0.58	0.54	0.42
3	0.58	0.54	0.42
3.5	0.58	0.54	0.42
4	0.58	0.54	0.42
4.5	0.58	0.54	0.42
5	0.56	0.54	0.42

AppendixA5: Experimental and simulated injection rate vs oil recovery

Water PV Injected	Experiment	Simulation	20 bbl/hr
0	0	0	0
0.5	0.16	0.16	0.14
1	0.36	0.4	0.28
1.5	0.54	0.5	0.4
2	0.58	0.56	0.42
2.5	0.58	0.58	0.42
3	0.56	0.58	0.42
3.5	0.56	0.57	0.42
4	0.56	0.56	0.42
4.5	0.54	0.55	0.42
5	0.54	0.54	0.42

Appendix B: Micro-CT image processing using ImageJ

The original image output from micro-CT scanners are commonly in two formats, a series of 2D cross-sections or a unitary 3D array as a volumetric dataset. To view and process the data into a usable format as input of the pore-scale simulators developed in Imperial College London, a software ImageJ is used. ImageJ is a public domain, Java-based image processing program developed at the National Institutes of Health. ImageJ has an open architecture that provides extensibility via Java plugins and recordable macros.

B.1 Data format of micro-CT images

Phoenix v|tome|x system outputs the projection shadow images, the configuration files and the micro-CT datasets, among which the most important data to the end users are two files. One is *.vgi file that is an ascii text with description of the micro-CT data. The most useful information contained in *.vgi files are the dimensions of the 3D image and the resolution of the image. The other is *.vol file consists of 32 bit real type data that is the 3D array of gray scale reflecting the volumetric information of the inspected specimen. Although it is 32 bit data type, the gray scale is only 16 bit due to the resolution of detector.

B.2 Importing and saving data

The typical output 3D image is about 1~1.2 GB from Phoenix v|tome|x system depending on the image size and data type. To enable ImageJ to view the whole image, the maximum memory usage of ImageJ is suggested to be set to 1500 MB through the menu: Edit->Options->Memory. Restart the program after the configuration to valid the modification.

To import the *.vol data, go to File->Import->Raw, input the dimensions and choose the proper datatype 32 bit real.

To import a series of 2D cross-sections, go to File->Import->Image Sequence.

To save the processed images, go to File->Save as->Raw data.

During the import, there is an option of 'Little-Endian Byte Order'. In computing, endianness is the byte (and sometimes bit) ordering in memory used to represent some kind of data, which is system dependent. To keep the data format consistency, please go to Edit->Options->Input/Output and tick 'Export Raw in Intel Byte Order" on.

B.3 Processing images

1. Cropping

To obtain the desired sub-section of the whole image, the plug-in of 'TransformJ' is used to crop the data in 3D with user defined dimensions.

2. Rescaling

Since the useful gray scale is only in 16 bit, it is necessary to subsample the gray scale to save the memory usage and hard disk storage by transforming the 32 bit real data to 16 bit. Go to Image->Type and choose 16 bit.

3. Filtering

To apply a median filter to the image, go to Process->Filters->Median, choose a radius that is the neighborhood range to judge the median value. Please note that, this median filter of ImageJ is a

2D filter. To apply a 3D median filter, it is suggested to use another freeware VolView (http://www.kitware.com/products/volview.html). More professional filters can be found in the software packages VGS Studio Max and Amira in the XMT lab in Imperial College London.

4. Segmentation

To transform the gray scale into black and white image (pore space and solid phase), go to Image->Adjust->Threshold. A threshold value is selected automatically by Image based on an isodata algorithm (Ridler and Calvard, 1978). Visual inspection is required to make sure the segmentation is roughly correct before applying the value to the global image. The resultant image is black (0) and white (255).

5. Normalization

Since the desired input data for porenet.exe (the program to extract a network from any generic 3D images) consists only 0s (pore space) and 1s (solid phase), we set the maximum value of the global image to 1 by visiting Process->Math->Max. Go to Image ->Adjust->B&C->Auto to obtain the best view condition whenever the contrast and brightness are uncomfortable.

Appendix B.4: 2D micro-CT image of Agbada rock and the extracted network (8µm resolution).

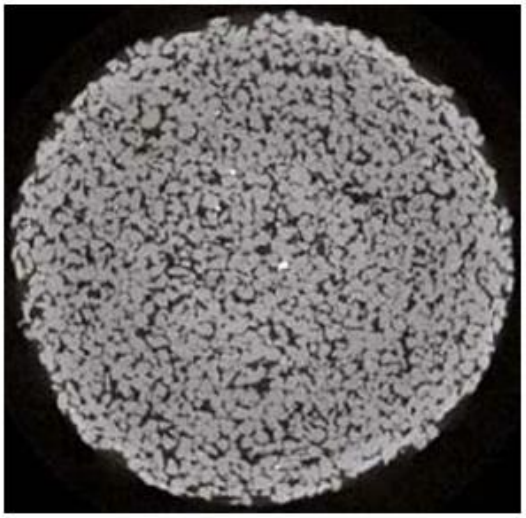

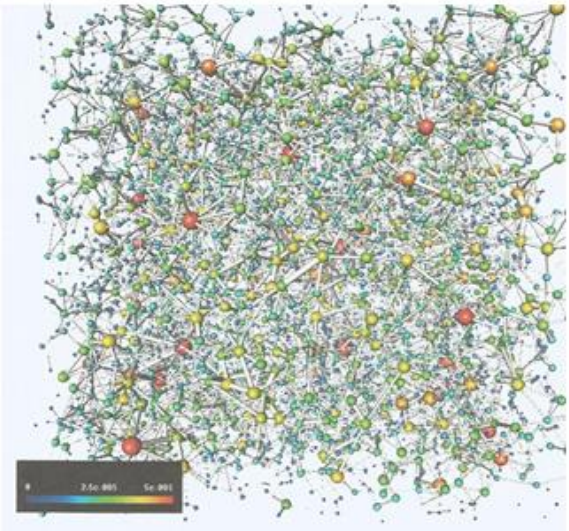

Appendix C: Eclipse Simulator

```
================================================================
====
--THIS IS THE DATA FILE USED AS SYTHETIC MODEL FOR THESIS STUDY
ON --- WATERFLOODING USING BUCKET-LEVERETT
-- ENCHANCE OIL RECOVERY.
-- TWO-DIMENSIONAL BLACK OIL.
-- SIMULATION, on: 28-Jul-2015 at: 10:37:31.
-- A REGULAR GRID WITH Five SPOT PATTERN RESERVOIR (INJECTORS
AND -- PRODUCERS) ARE
-- EXAMINED.IMPES SOLUTION METHOD IS USED FOR THIS SIMULATION
AND ---- THE PRODUCTION IS CONTROLLED BY FLOW RATE AND MIN. BHP.
-- STUDENT NAME: ONUOHA FIDELIS WOPARA
-- SUPERVISOR NAME: PROFESSOR SUNNY IYUKE
================================================================
====
```

Appendix C.1: Programme

```
RUNSPEC
TITLE
Waterflooding using buckley-leverett equation
START
 1 'JUL' 2015 /
FIELD
OIL
WATER
MONITOR
RSSPEC
NOINSPEC
MSGFILE
 1 /
DISPDIMS
 1 2 1 /

DIMENS
 41 41 10 /
EQLDIMS
 1 100 100 1 20 /
REGDIMS
 1 1 0 0 /
TABDIMS
 1 1 20 20 1 20 20 1 /
WELLDIMS
 6 11 3 6 /
GRID
GRIDFILE
```

```
 0 1 /
PVCDO
-- Dead Oil PVT Properties
      3800    1.15 2.895798e-005     2.8      1* /
PVTW
-- Water PVT Properties
        3800         1 0.000241316495      1.03    1*/
RSCONSTT
-- Constant Rs per PVT Region
        0.05      3349 /
DENSITY
-- Fluid Densities at Surface Conditions
   52.93267    62.42797   45.01057    /
ECHO
ROCK
-- Rock Properties
  3800 2.895798e-005                          /
SWOF
-- Water/Oil Saturation Functions
           0.2           0       0.789           0
          0.25       0.002       0.622           0
           0.3       0.008       0.468           0
          0.35       0.021       0.371           0
           0.4       0.034       0.284           0
          0.45       0.053       0.217           0
           0.5       0.075       0.162           0
          0.55         0.1        0.12           0
           0.6        0.13        0.08           0
          0.65       0.168       0.052           0
           0.7       0.208       0.027           0
          0.75        0.25        0.01           0
           0.8       0.301           0           0
/
Equilibration Data Specification
8000  3800   600   1*   7150   1*   1*   1*   1*   1*   1*
/
RPTSOL
-- Initialisation Print Output
/
OUTSOL
-- Restart File Output Control
'BASIC=2' 'NORST=0' /
RTEMPA
-- Initial Reservoir Temperature
190 /
END
V
```

Appendix C.2: Dimensionless water cut vs distance from injector to producer wells